2008

Annual Report
Jahresbericht

Remote Sensing
Technology Institute

Department
Atmospheric Processors

DLR

Contents

1. Foreword

Time flies and another year has passed with the 8th edition of the annual report for the year 2008 now being available. It summarizes results from scientific research and development work accomplished by the department *Atmospheric Processors* (AP) at DLR's Remote Sensing Technology Institute (IMF). The previous report for 2007 was the first one published in an English version. This change, addressing a wider audience, was rather welcomed by the readership. We hope that with the current report we continue in that manner and provide our partners again with interesting details of our activities.

In the areas of our major 'data providers', i.e. SCIAMACHY on ENVISAT and GOME-2 on MetOp, the achievements of last year could be consolidated. Algorithm and product development for SCIAMACHY followed the paths outlined by the SQWG. The goals specified in the plans could be reached thus extending SCIAMACHY's product suite and improving its quality even further. Preparatory work on the mission extension until 2013 at the level of instrument settings has begun. This is the basis for reprogramming SCIAMACHY accounting for the orbit modification, presently scheduled for end October 2010. GOME-2 continues to deliver a wealth of measurement data. The high quality of the products generated under DLR responsibility in the O3M-SAF had led EUMETSAT to declare O_3, NO_2 and SO_2 as operational. Investigating retrieval of further geophysical parameters from GOME-2 spectra is ongoing work and has already been successfully proven on species as e.g. BrO which has been granted *demonstrational* status.

In 2008 we added a new research area to our portfolio. In the Helmholtz alliance *Planetary Evolution and Life* we contribute our know-how in atmospheric radiative transfer, i.e. our theoretical backbone. This shall help to better understand planetary atmospheres. Since the selected approaches can not only be applied to the Earth and bodies in the Solar System but also to exoplanets, it is an opportunity for participating in 'very remote' sensing.

Early November 2008 our department spent a couple of days at the town of Nördlingen to elaborate on short- and mid-term strategies as well as future developments. Nördlingen is located in the Nördlinger Ries, a well known 15 Million years old impact crater. This venue was a very inspiring mixture of work and leisure. We hope that the ideas born 'in conclave' lead to exciting results in 2009 and the following years.

The editorial team wishes to thank all authors and co-authors for their contributions.

Prof. Dr. Thomas Trautmann   Dr. Manfred Gottwald

IMF-AP (Nördlingen, 11/2008)

2. Highlights of the Year 2008 – Operational O3M-SAF Products at DLR

D. Loyola, P. Valks, W. Zimmer, N. Hao, S. Emmadi (TUM), M. Rix (TUM), S. Kiemle (DFD-IT), D. Delaure (DFD-BI), K.-H. Seitz (DFD-BI), T. Ruppert (DFD-MM)

The Satellite Application Facility on Ozone and Atmospheric Chemistry Monitoring (O3M-SAF) is a key component of EUMETSAT's Polar System (EPS) ground segment. The EPS mission comprises three MetOp satellites that will supply operational products during the next 14 years. In March 2007 EUMETSAT initiated the regular delivery of GOME-2 level 1 products via EUMETCast and two weeks later DLR was able to start the test-dissemination of GOME-2 total ozone and NO_2 products via EUMETCast (Near-Realtime – NRT) and FTP (Offline – OL). These products reached the demonstrational status after the Operational Readiness Review (ORR-A2, June 2007).

At the ORR-A3 in April 2008, DLR presented two new GOME-2 products – total Bromine Oxide (BrO) and Tropospheric Nitrogen Dioxide (NO_2). These products reached the demonstrational and pre-operational status, respectively. The dissemination of the off-line products via EOWEB© and UMARF was also initiated in April 2008. Finally at the ORR-B in November 2008, total Sulphur Dioxide (SO_2) was presented as a new product together with the validations of more than one year total column products. The validation reports from the University of Thessaloniki and the BIRA institute in Brussels confirmed the high quality reached by the total O_3, total and tropospheric NO_2, and total SO_2 products. Therefore the ORR-B review board recommended that the following products be declared operational:

- total column ozone (Near-Realtime – NTO/O3, Offline – OTO/O3)
- total column NO2 (NTO/NO2, OTO/NO2)
- tropospheric NO2 (NTO/NO2Tropo, OTO/NO2Tropo)
- total column SO2 (OTO/SO2)

The GOME-2 O3M-SAF products provided by DLR are already being used in the GMES atmospheric services ESA-PROMOTE and EU-GEMS as well as other national and international projects. The results were presented in a number of scientific symposia and workshops.

Various examples exist highlighting the usage of the operational GOME-2 total ozone and NO_2 products. Also the latest addition to the GOME-2 portfolio, SO_2, already provides widely accepted results, as e.g. shown in chapters 3-1 and 3-2 of our annual report.

Total Ozone
O3M-SAF total ozone from GOME-2 is being used in a number of projects. Maps with the daily total ozone (level 3), assimilation (level 4), animations, as well as dedicated pages monitoring the ozone hole are available at the World Data Center for Remote Sensing of the Atmosphere (WDC-RSAT). The *World Ozone and Ultraviolet Radiation Data Centre* in Canada (part of WMO-GAW) uses GOME-2 total ozone together with other satellite and ground-based data to produce global maps (see fig. 2-1). In ESA's GMES SE projects PROMOTE and TEMIS service GOME-2 total ozone serves as input for the assimilation maps. GOME-2 total column ozone is currently also monitored in operations at ECMWF, the leader of the EU GMES projects GEMS and MACC. The bottom panel in fig. 2-1 shows the difference between the current ECMWF assimilation analysis and the GOME-2 ozone observations; both data sets already agree very well.

Total ozone (DU) / Ozone total (UD), 2009/01/26
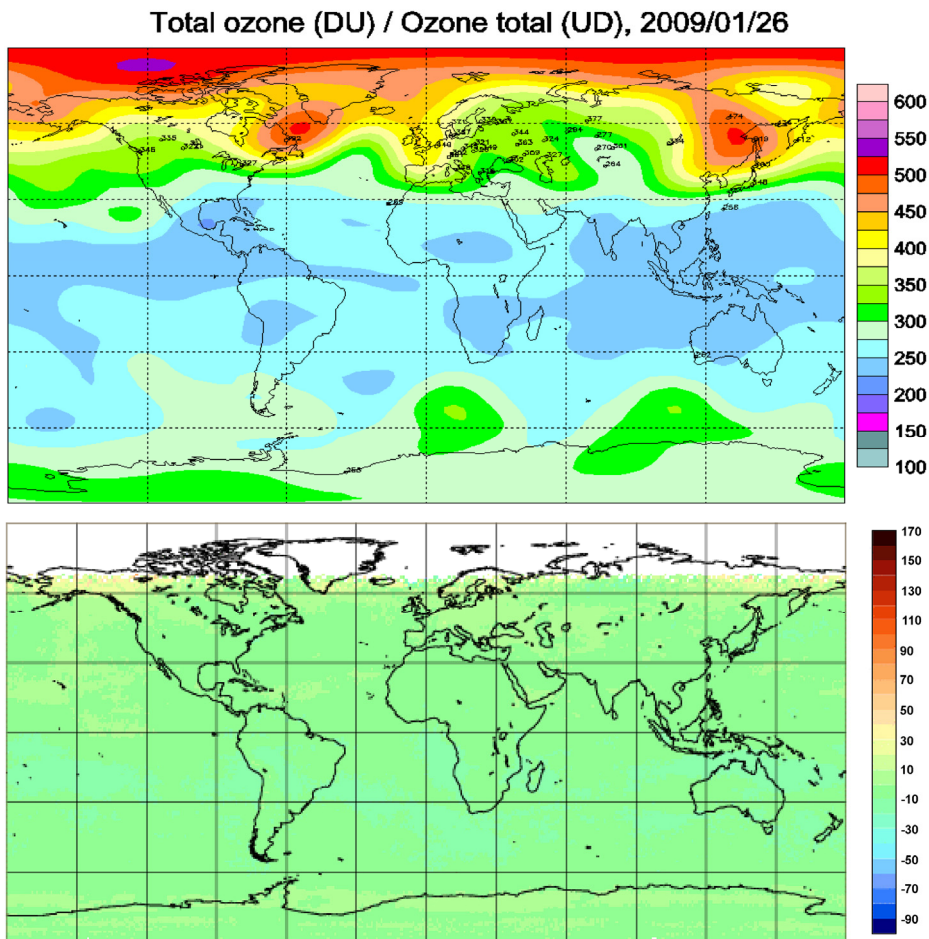
Fig. 2-1: Total ozone map from the *World Ozone and Ultraviolet Radiation Data Centre* in Canada based on satellite, including GOME-2, and ground-based measurements (top panel). The bottom panel illustrates the difference between the ECMWF assimilated total ozone and the GOME-2 observations.

Total Nitrogen Dioxide

Total NO_2 shipping emissions can be measured with GOME (since 1995), SCIAMACHY (since 2002) and GOME-2 (since 2006). Fig. 2-2 displays the shipping tracks in the Bay of Bengal obtained averaging O3M-SAF total NO_2 from GOME-2 measurements in 2008. Based on such NO_2 shipping emissions the sea trade volume can be derived. It shows a constant increase since 1995.
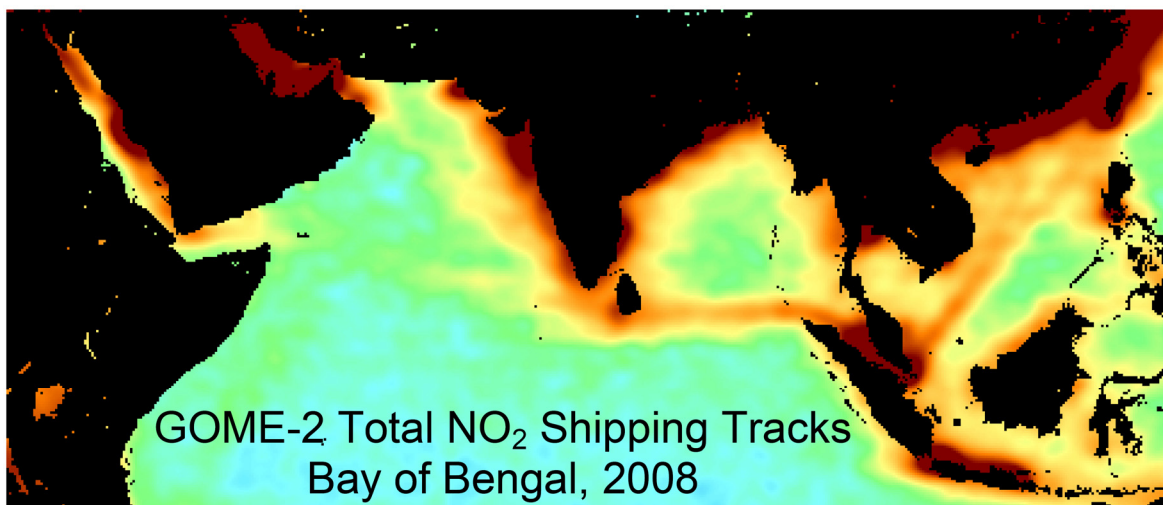
Fig. 2-2: Shipping Tracks observable from GOME-2 NO_2 measurements in 2008.

Tropospheric Nitrogen Dioxide

Contaminations from industrial pollution and vehicles are clearly visible in the generated tropospheric NO₂. Fig. 2-3 illustrates O3M-SAF tropospheric NO₂ from GOME-2 measurements over China in two weeks of 2007 (top panels) and 2008 (bottom panels). The contamination over Beijing, marked by a circle, in the period July/August 2008 clearly appears reduced due the controls applied during the 2008 Olympic Games.
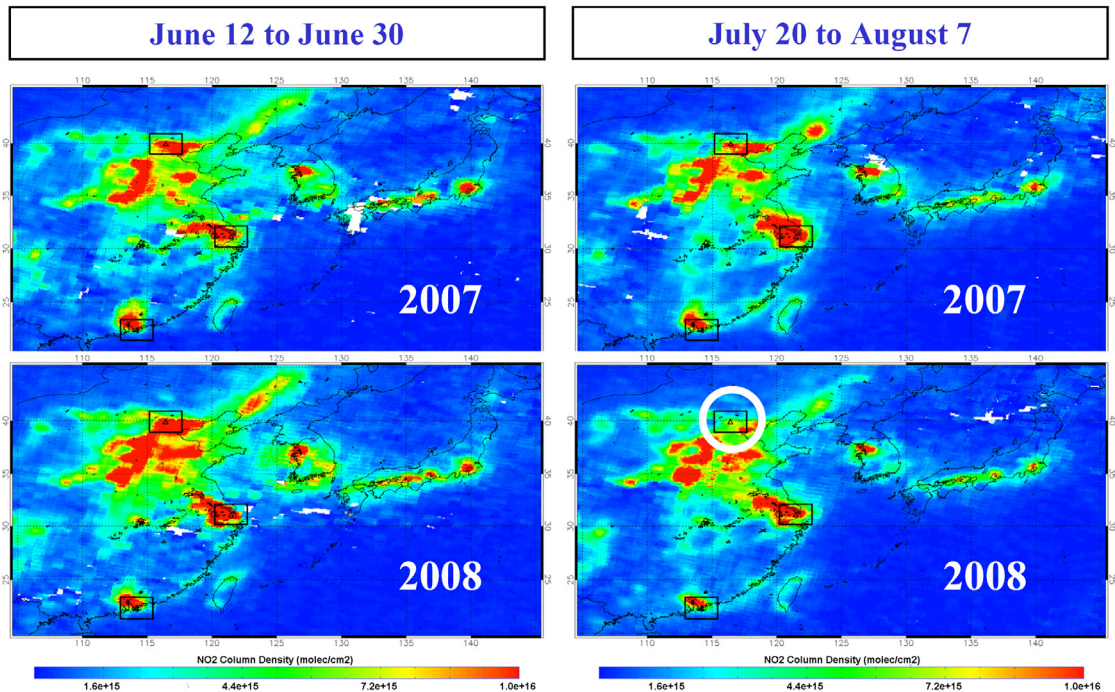
Fig. 2-3: Tropospheric GOME-2 NO₂ measurements in 2007 and 2008 over China. Contamination in Beijing is reduced during the Olympic Games.

Operations Report 2008

GOME-2 total column products were generated and disseminated regularly during the complete year 2008. Fig. 2-4 shows the dissemination statistics for minimum/average/maximum timeliness (top panel) and the corresponding availability for all Product Dissemination Units (PDU), i.e. GOME-2 level 1 products containing 3 minutes of data, received at DLR. As obvious, the level 2 NRT products are usually disseminated to the users already 2:00 hours after sensing. The availability measured as the percentage of PDUs disseminated before 3:00 hours is shown in the bottom panel from fig. 2-4.

The off-line products are delivered typically three days after sensing (see top panel from fig. 2-5). Their quality is controlled by the operators using a dedicated QA tool for GOME-2. Statistics indicate that the vast majority of the OL products were marked as 'good' (bottom panel of fig. 2-5).
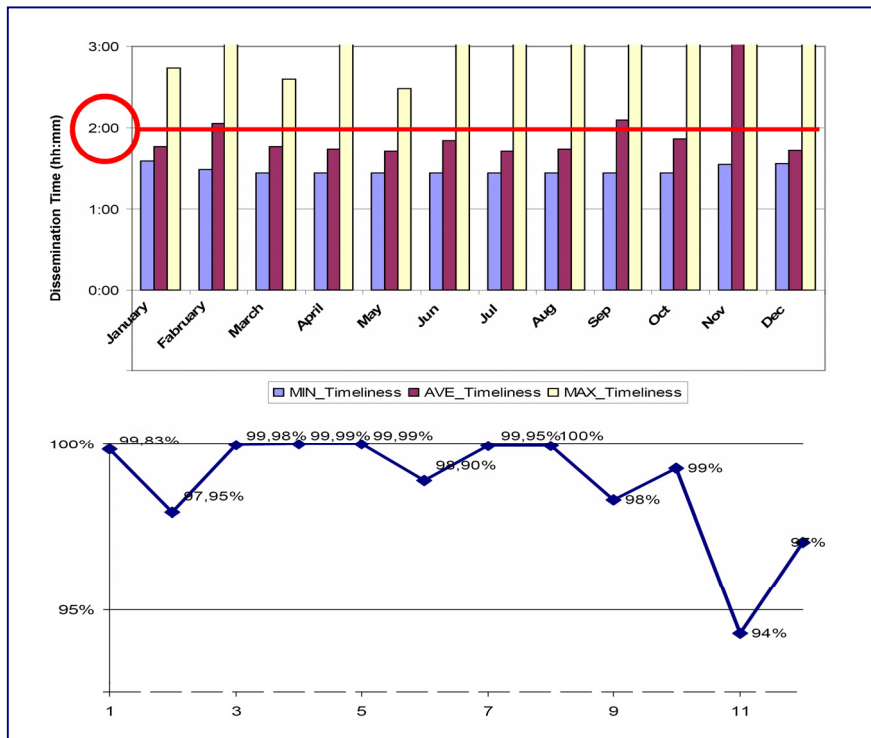
Fig. 2-4: Operations Report for the O3M-SAF NRT products at DLR. The NRT products are disseminated to the users usually in less than 2:00 hours after sensing.
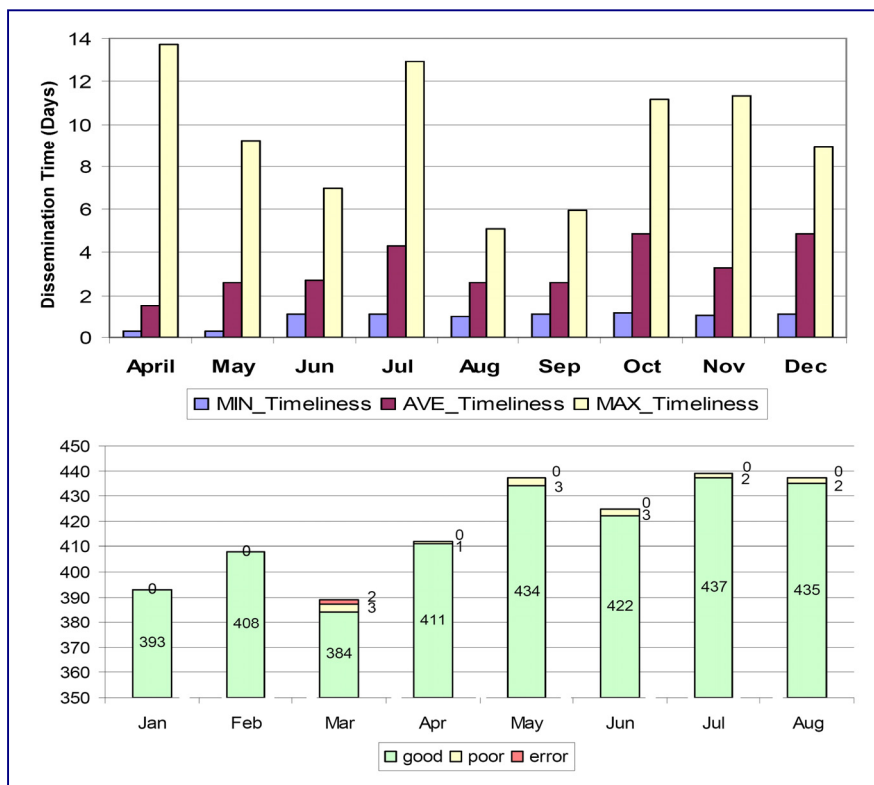
Fig. 2-5: Operations Report for the O3M-SAF OL products at DLR. The off-line products are disseminated to the users after manual quality control and usually in less than four days after sensing.

References

The GOME-2 Algorithm Technical Baseline Document (ATBD), Product User Manual (PUM) and validation reports are available at the GOME-2 page on the WDC-RSAT under http://wdc.dlr.de/sensors/gome2.

3. Current Projects

3.1 Monitoring of Volcanic Sulfur Dioxide Emissions using the GOME-2 Satellite Instrument

M. Rix (TUM), P. Valks, N. Hao, W. Zimmer, S. Emmadi (TUM)

Volcanic eruptions pose a major hazard to those living in the vicinity of volcanoes. Because of rapidly growing populations urban environments more and more approach the sites of active volcanoes. In addition the massive developments in infrastructure and transportation systems make societies more vulnerable. The region closest to an erupting volcano is directly affected by lahars or lava and pyroclastic flows while the fallout of ash plumes not only impacts more remote areas but could also be threatening to aviation. Given the erratic nature of eruptions it is difficult to correctly predict where and when such events occur. This uncertainty leaves no time for preparations and often causes severe disasters. Spaceborne remote sensing of volcanoes supports ground based monitoring systems aiming at minimizing the impact on humans and our environment.

At IMF-AP we focus on the retrieval of trace gases as a reliable indicator for volcanic activity. One of these species is sulfur dioxide (SO_2). Anthropogenicly it is produced in power plants, refineries, metal smelting and the burning of fossil fuels, but its atmospheric background level is usually very low. Volcanic eruptions and their passive degassing are the most important natural sources of sulfur dioxide. During an eruption, SO_2 is the third most abundant gas found in volcanic plumes after H_2O and CO_2. Changes in the degassing SO_2 flux can be a precursor for the onset of volcanic activity. The lifetime of atmospheric SO_2 varies from approximately 1-2 days in the troposphere to several weeks in the stratosphere. In the troposphere it is transformed into sulfuric acid and is responsible for acid rain. If SO_2 is brought into the stratosphere by volcanic eruptions, it can remain there for several weeks and travel over long distances (see e.g. Kasatochi eruption in August 2008). Once transformed to sulfuric aerosols it also causes a cooling in the atmosphere (e.g. Pinatubo eruption, 1991).

In 2008, we concentrated on developing several improvements for the SO_2 retrieval algorithm. In a first step slant column densities (SCD) of SO_2 are determined using the well established *Differential Optical Absorption Spectroscopy (DOAS)* method in the wavelength region between 315-326 nm. In this retrieval wavelength range, there is a strong interference of the SO_2 and ozone absorption signals, especially at high solar zenith angles. Therefore, an interference correction was developed to be applied to the SO_2 slant column values, based on one year of GOME-2 data. In addition a correction that accounts for an equatorial offset is calculated on a daily basis. The corrected slant column densities of SO_2 are converted to geometry-independent vertical column (VC) amounts through division by an appropriate air mass factor (AMF).

For SO_2, the AMF is strongly dependent on the measurement geometry, surface albedo, clouds, aerosols, and most importantly, the shape of the vertical SO_2 profile in the atmosphere. For the AMF calculations, an a priori volcanic SO_2 profile is assumed with a predefined central plume height. As the correct plume height is rarely available at the time of measurement, the SO_2 column is now computed for three different assumed volcanic plume heights (2.5 km, 6 km and 15 km) above ground level. The lowest height represents passive degassing of low volcanoes, the second height effusive volcanic eruptions or passive degassing of high volcanoes and the third height explosive eruptions. To account for the temperature dependence of the SO_2 cross-sections, a correction was calculated that is applied to the slant columns depending on the assumed height of the SO_2 plume. The AMFs are calculated with the radiative transfer model LIDORT.

The SO_2 columns retrieved at IMF-AP are used for several early warning services related to volcanic hazards, such as the *Support to Aviation Control Service (SACS)* which is part of the GMES (Global Monitoring for Environment and Security) Service Element for the Atmosphere (PROMOTE) and the mobile volcano fast response system, *Exupéry*, within the BMBF GEOTECHNOLOGIEN program.

During 2008, several volcanic eruptions have been detected by GOME-2 and analyzed at IMF-AP. A recent event was the Kasatochi eruption in August 2008 in Alaska. It is a good example on how spaceborne measurements can provide valuable information as the region of the Aleutian Island chain has a very high density of volcanoes but lacks regular monitoring. Three major eruptions emitted large amounts of volcanic ash and gas into the atmosphere that rose to a height of at least 10 km, an altitude

where they were a major hazard to air traffic. Due to the low levels of ash concentration using ash absorption features were no efficient means for eruption cloud tracking. However remotely sensed SO_2 densities were much better suited for this purpose. The SO_2 plume of the Kasatochi was first detected during the GOME-2 overpass on August 8th. GOME-2 measured maximum SO_2 column amounts of ~ 150 DU the first day after the eruption. (1 DU corresponds to a total mass of approximately 91.5 tons of SO_2 for a GOME-2 pixel size of 40 km x 80 km.) A first estimate from the GOME-2 data of the total erupted mass of SO_2 during the eruption yields about 1.2×10^6 tons of SO_2. The volcanic cloud was transported across North America intersecting some of the main air traffic routes in that region, as most intercontinental flights from the US to Asia fly over Alaska. One week after the eruption the SO_2 cloud reached Spain on August 14th (fig. 3-1). The SO_2 cloud could be traced for several more weeks as it was distributed all over the northern hemisphere.
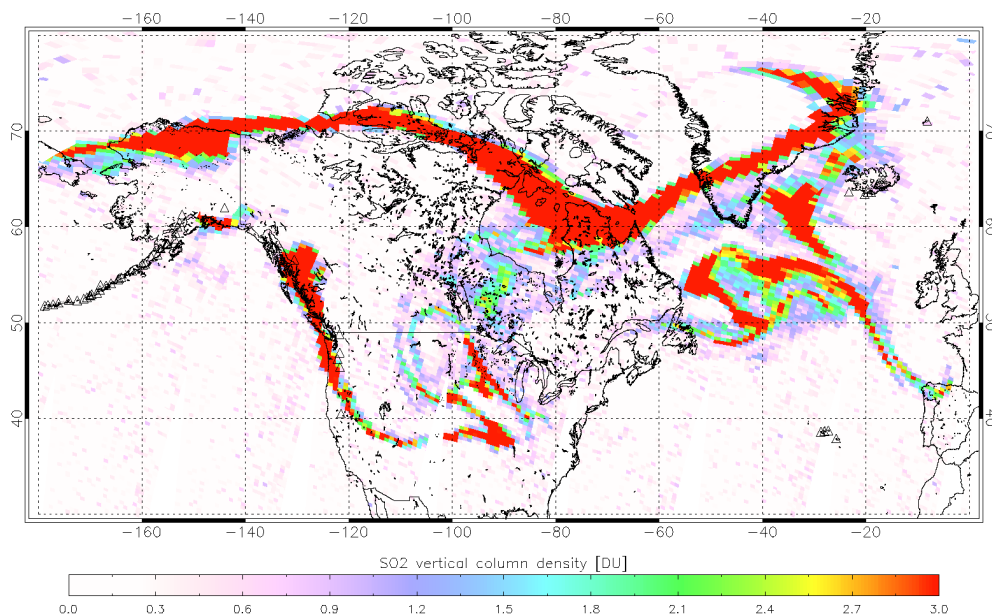
Fig. 3-1: Volcanic SO_2 plume from the Kasatochi eruption (Aleutian Islands) as detected on August 14, 2008 by GOME-2. The SO_2 cloud had been transported over North-America and reached Europe one week after the eruption. Kasatochi volcano erupted on August 7, 2008.
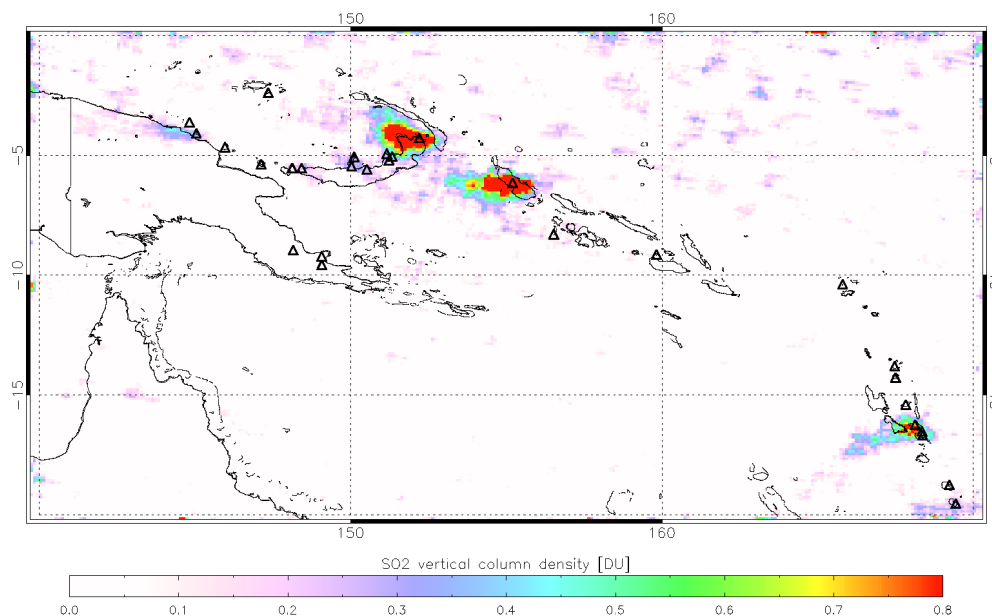
Fig. 3-2: Monthly averaged SO_2 column amounts measured by GOME-2 from passively degassing volcanoes in the volcanic region Papua New Guinea/Vanuatu, March 2008. The degassing volcanoes are from North to South Rabaul, Bagana and Ambrym.

Besides detecting and tracking volcanic eruptions, GOME-2 has also proven its ability to measure non-eruptive degassing of volcanoes. This is of great importance in early warning of volcanic risk. Increasing activity at many volcanoes is indicated by increased gas fluxes at the surface. Rising high-temperature magma releases SO_2 and therefore increased SO_2 degassing can often be a precursor of a magmatic eruption.

An example for the ability of the GOME-2 instrument to monitor the degassing behavior of volcanoes is provided in fig. 3-2. In the monthly averaged SO_2 map of March 2008 for the geographical region of Papua New Guinea/Vanuatu three degassing volcanoes are clearly visible. These are from north to south Rabaul (688 m), Bagana (1750 m) and Ambrym (1334 m).

3.2   GOME-2 Sulphur Dioxide (SO₂) Data Search Engine in WDC-RSAT

K. Reissig (IBR), D. Loyola, P. Valks, T. Erbertseder (DFD-KA)

One of the major trace gases retrieved from GOME-2 data is sulphur dioxide (SO_2). It is not only a tracer for tropospheric pollution but also a suitable means for detecting and monitoring volcanic eruptions (see e.g. chapter 3-1 of this annual report). Quick and user friendly access to GOME-2 SO_2 results is a pre-requisite for establishing a renowned service in this field. Therefore IMF-AP, together with DFD-KA, decided to implement and operate as part of the WDC-RSAT a GOME-2 SO_2 data search engine. It is available via http://wdc.dlr.de/data_products/SERVICES/GOME2NRT/so2.php. This engine provides SO_2 images of the products which have been generated in Near-Realtime as part of our cluster's responsibilities in the Ozone and Atmospheric Chemistry Monitoring SAF (O3M SAF).

Access starts with selecting data based on (see fig. 3-3)

- Pre-defined regions of interest: The user can select the region of interest over a drop-down menu. The zoomed-in selected region is displayed on a map.
- Acquisition start/stop times: The data is available from 2008 onwards.
- SO_2 column density thresholds: A SO_2 limit can be specified such that only datasets exceeding this limit are displayed.
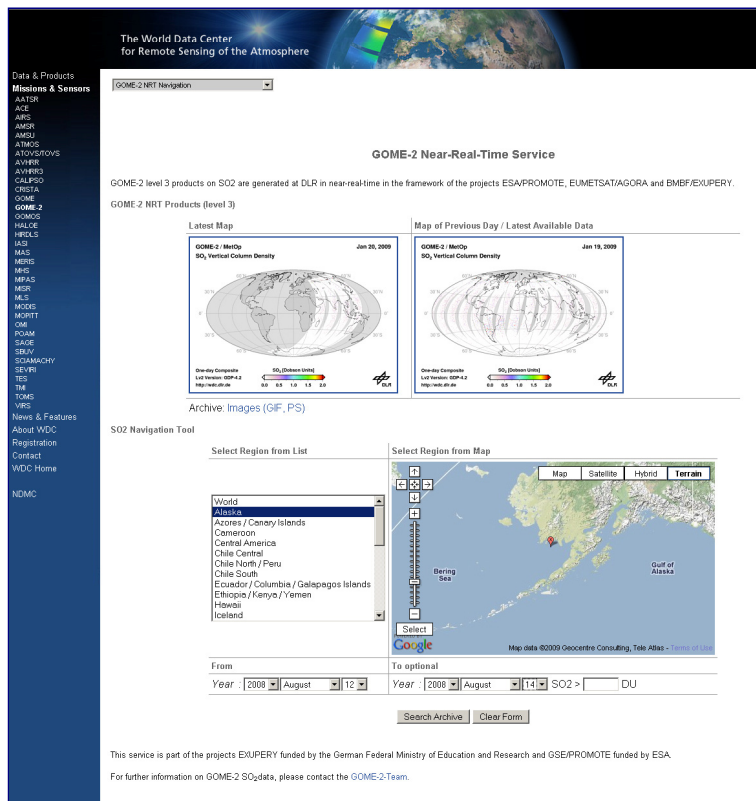
Fig. 3-3: GOME-2 SO₂ data search engine entry page at the WDC-RSAT

By clicking 'Search Archive' button, the query program is invoked to extract from the archive those datasets matching the selected search criteria. After completion, a detailed view is displayed, day-by-day, for each entry on the result page. It includes SO_2 vertical columns together with retrieved cloud related information – cloud fraction, cloud-top height and cloud-top albedo – in the region of interest.
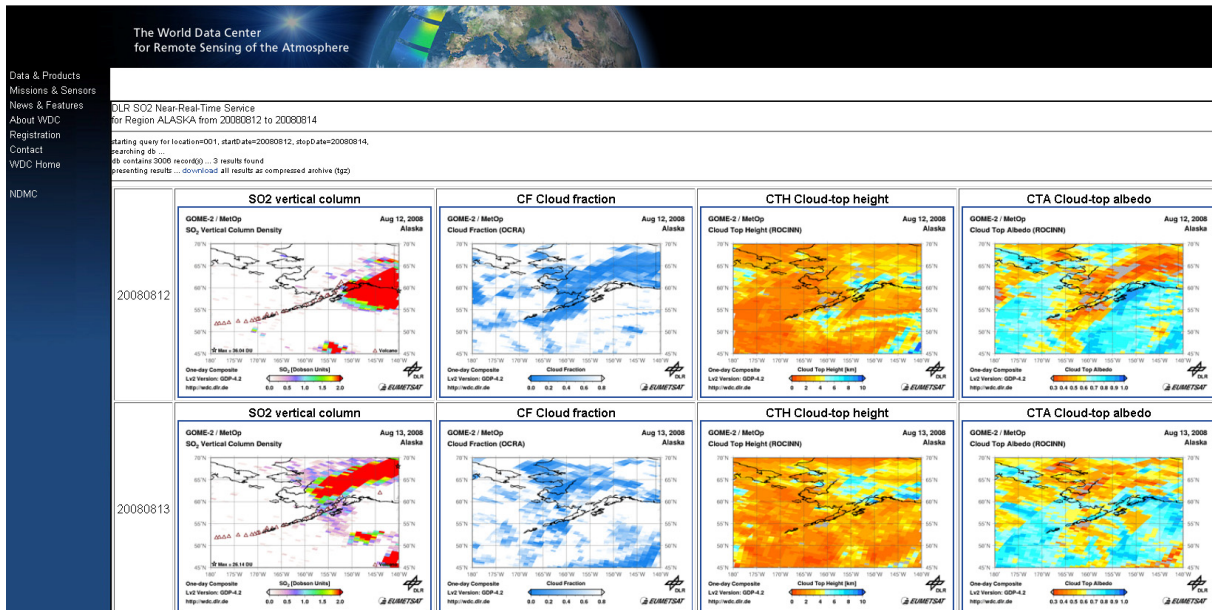
Fig. 3-4: GOME-2 SO_2 data search engine query results page at the WDC-RSAT

Full size images can be displayed in separate windows after clicking on the corresponding thumbnail, (fig. 3-5 left). In these windows, the user can navigate to the next/previous data set on time as well as the next/previous product, i.e. navigate to the cloud parameters corresponding to the selected SO_2.

Original data for the result set as displayed on the main results page can be downloaded in the form of a compressed .tar file by clicking the download link on top of the page.
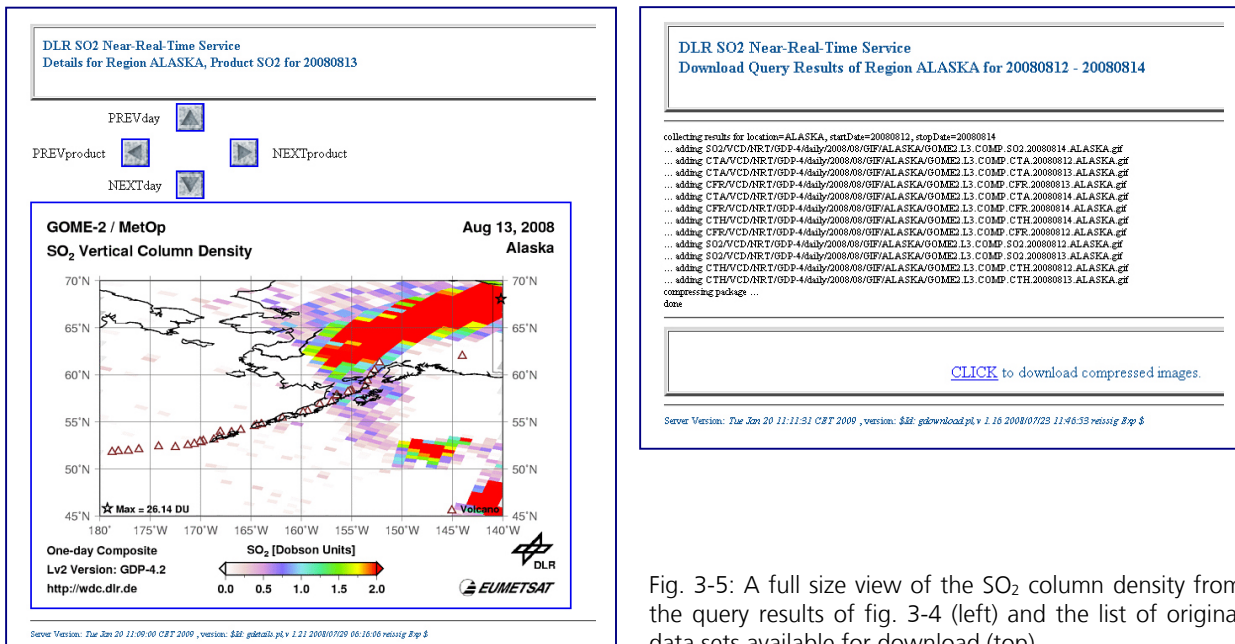
Fig. 3-5: A full size view of the SO_2 column density from the query results of fig. 3-4 (left) and the list of original data sets available for download (top).

The GOME-2 SO_2 data search engine is operational since mid 2008. Its software is successfully tested under the Firefox browser (version 1.5 and higher) on Windows XP and Unix operating systems. The search engine has been designed as a general tool applicable in principle to all GOME-2 products available in WDC-RSAT. On the short term we plan to deploy a version of it for also accessing the GOME-2 tropospheric NO_2 products.

3.3 Long-term Analysis of GOME In-flight Calibration Parameters and Instrument Degradation

M. Coldewey-Egbers, S. Slijkhuis, B. Aberle, D. Loyola

Since 1995 the GOME, the *Global Ozone Monitoring Experiment* measures solar and backscattered spectra in the ultraviolet and visible wavelength range. The GOME Data Processor (GDP) at DLR is the ground segment for the GOME instrument *(Loyola 1997)*, incorporating among other things a Level 0-1 processing chain, and the complete GOME data archive. During the Level 0-1 processing, GOME data is converted into calibrated radiances by applying calibration algorithms and calibration parameters. Many calibration parameters are established on a regular basis from in-flight observations of the spectral calibration lamp, of the internal LEDs (Light Emitting Diodes), of the Sun, and from Dark measurements.

After almost 12 years of successful operation and data processing, it is now of great interest to analyse the in-flight calibration results and parameters, to obtain a first long-term monitoring of their behaviour. The calibration parameters which are calculated during the Level 0-to-1 processing are a good means to monitor the stability of the instrument and its measurements. Stable long-term satellite data are needed as the requirements for more accurate satellite information products are steadily increasing, e.g. global climate monitoring requires temperature changes of a few 0.1°C, or ozone trends with a precision of 1% per decade.

At the end of 2006, an update of the GDP Level 0-1 processor has been developed, in order to reprocess the entire GOME data set and to provide an homogeneous data record. Results from the initial phase of this study were incorporated in the development, leading to improved dark signal correction, and a significantly improved wavelength stability over the entire time period, especially in channels 3 and 4.

The following parameters were monitored:

Solar throughput and PMD polarisation correction factors ('Q-factors'): By means of the daily solar irradiance measurements, the degradation of the GOME sensor was monitored. In channels 1 and 2 the intensity decreased by 70-90% and 35-65%, respectively. The degradation in channels 3 and 4 is lower, and became significant in 2001. The main part of the degradation has been explained in terms of deposits on the scan mirror.

The signals of the three PMDs show qualitatively a similar degradation as the corresponding channel wavelengths. A quantative analysis of the 'Q-factors' yields a slightly differential degradation between PMD and corresponding channel signals.
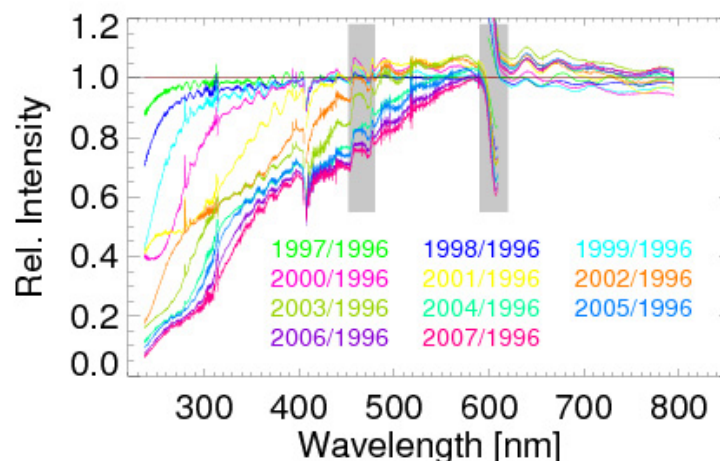
Fig. 3-6: Ratios of the sun mean reference spectra of GOME from 9th January 1997 to 2007 to the corresponding reference spectrum from 1996.

Spectral calibration: The stability of the spectral calibration was inferred by monitoring both, the difference between the exact and GDP-calculated wavelength of the emission lines, and the variability of all calculated GOME wavelengths for a fixed pre-disperser temperature. The latter is very stable and

lies between 0.0015 and 0.004 nm over the whole spectral range, except for the beginning of channel 3 due to a lack of suitable emission lines. The former stability was significantly improved in the new GDP after some instable lines were dismissed for processing (see fig. 3-7).

Analyzing the correlation between wavelength and pre-disperser temperature yields a very complex interaction, which depends on the spectral position on the detector.
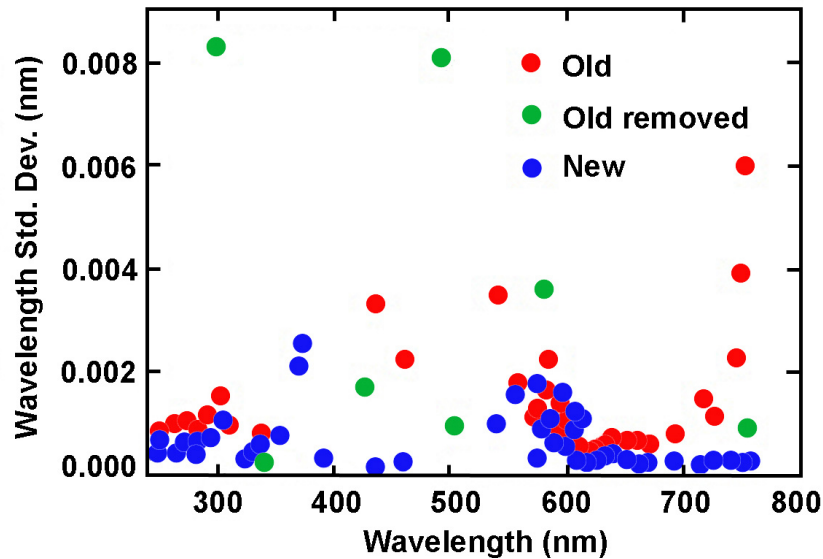
Fig. 3-7: Standard deviation of wavelengths for all calibration orbits between June 1995 and May 2003. Red dots: old wavelength calibration with 67 spectral lines, green dots: spectral lines, which were removed from the calibration analysis, and blue dots: new wavelength calibration.

Dark signal shows a steady increase over the 10 years analysed. This occurs on the detectors as a whole, rather than just in a few bad pixels as might be expected. A linear increase of the dark signal of 3.5-4.5 BU/s in 10 years was found. The PMD zero offsets show a small increase of 0.5-1% up to 2005.

The noise of the detector pixel readouts and the PMD noise level displayed a distinct seasonal cycle until June 2003. We identify this as influence of the SAA region (from which few measurements were available after 2003 when the ERS tape recorder failed).
For this reason, the recently updated version 4.0 of the GDP Level 0-1 processor includes an algorithm to automatically discard anomalous calibration measurements such as the ones over the SAA region – calibration packets are checked for the PMD noise, whether this value is below or above a certain threshold.

The pixel-to-pixel gain, derived from LED measurements, increased in channel 2 by 100%, and in channels 3 and 4 by about 50%.

References

D. Loyola, W. Balzer, B. Aberle, M. Bittner, K. Kretschel, H. Mühle, T. Ruppert, C. Schmid, S. Slijkhuis, R. Spurr, W. Thomas, T. Wieland, and M. Wolfmueller: Ground Segment for ERS-2/GOME Sensor at the German D-PAF, in 3rd ERS Scientific Symposium, Florence, Italy, ESA SP-414 Vol.II, 591, 1997

3.4 SCIAMACHY Quality Working Group, Data Quality Monitoring and Level 0-1 Improvements

G. Lichtenberg, S. Slijkhuis, B. Aberle, D. Scherbakov, M. Gottwald

The SCIAMACHY Quality Working Group (SQWG) was initiated in March 2007 to coordinate, harmonise and streamline the development of SCIAMACHY operational data processing. Members are IUP/IFE, University of Bremen as the prime, DLR-IMF, BIRA and SRON. Additionally it cooperates with KNMI. The SQWG acts as the sole interface to the agencies ESA, DLR, NIVR and BIRA for the evolution of the data processors. The prototype version 5 (which is currently implemented as operational version 7) for Level 0-1b processing and version 4 of the off-line Level 1b-2 processor were first ones delivered in 2008 under the auspices of the SQWG. A major milestone was reached when the agencies reviewed the work of the SQWG in March 2008 and granted the second year of the contract. The further continuation until the end of 2010 is currently under negotiation with the agencies. The processor developments are described in detail in the following.

Apart from the further evolution of the data processing, IMF-AP also gives expert support for the maintenance of the operational processors and the quality of the data products. The tasks include investigation and solution of product or processor anomalies, answers to helpdesk requests and support to ESA for the implementation of the operational processing chain. The first contract for the data quality (called DPQC) had a duration of 3 years and ended in August 2008. A new consortium took over the task of quality control. Within this consortium IMF-AP continues to give expert support for SCIAMACHY'S data processors.

The starting point for our activities in SCIAMACHY data processing is the transfer of the level 0 measurement data to calibrated radiances, i.e. the level 0-1 processing. It includes three facilities:

- **SciCal:** This facility was developed by IMF in order to provide calibration data such as dark correction, sun reference spectra. It extracts all necessary calibration data from Level 0 products and writes them to Auxiliary Data Files (ADF) which are subsequently used to calibrate the spectra.
- **Level 0-1 prototype:** The processor converts spectra from binary units per detector pixel into intensity per wavelength. It is the basis for the implementation of the operational Level 0-1 processor done by industry and under constant development at IMF.
- **SciaL1c:** The SciaL1c tool is a command line tool that allows users to generate calibrated data from Level 1b (called Level 1c data). Each calibration step can be switched according to the users choice. SciaL1c can also list states in the product and export data to an ASCII file.

In the past year IMF delivered new versions of all tools in the Level 0-1 processing chain including full documentation and verification.

Level 0-1Prototype Development
The prototype development continued throughout 2008. The main tasks were the verification of the prototype version 5, that is the basis of the operational IPF version 7, the delivery of the algorithm baseline, the verification of the new features and the preparation of the version 6 for 2009.

Prototype version 5 includes

- matrix stray light correction for channel 2
- correction of wrong scanner encoder values
- inclusion of *Limb_Mesosphere_Thermosphere* states in the Measurement Datasets (MDS).

The matrix correction for spectral stray light for channel 2 was already described in the contribution to last year's annual report in detail. Verification of this feature against a reference algorithm of SRON turned out to be successful.

During the development of the CO in-house retrieval we discovered that on rare occasions the geolocations calculated in the Level 0-1 processing led to abnormally small ground pixels. Several other users reported the same behaviour to the ESA helpdesk. Together with the SOST team the reason was traced to a known internal error of the scanner modules: The scanner mirror moves correctly, but the encoder values used to calculate the line-of-sight of the instrument and location on-ground are not

updated in the downlinked instrument data. This causes almost identical values in the geolocation during one scan and thus leads to apparently very small groundpixels. The error usually occurs at the end of one data package of the telemetry stream. Since the nadir and limb states of SCIAMACHY use fixed scanner profiles which are identical from one scan to the next, a software correction permits correcting erroneous scanner readouts, i.e. deriving correct geolocation values. Fig. 3-8 displays an example for such a case.
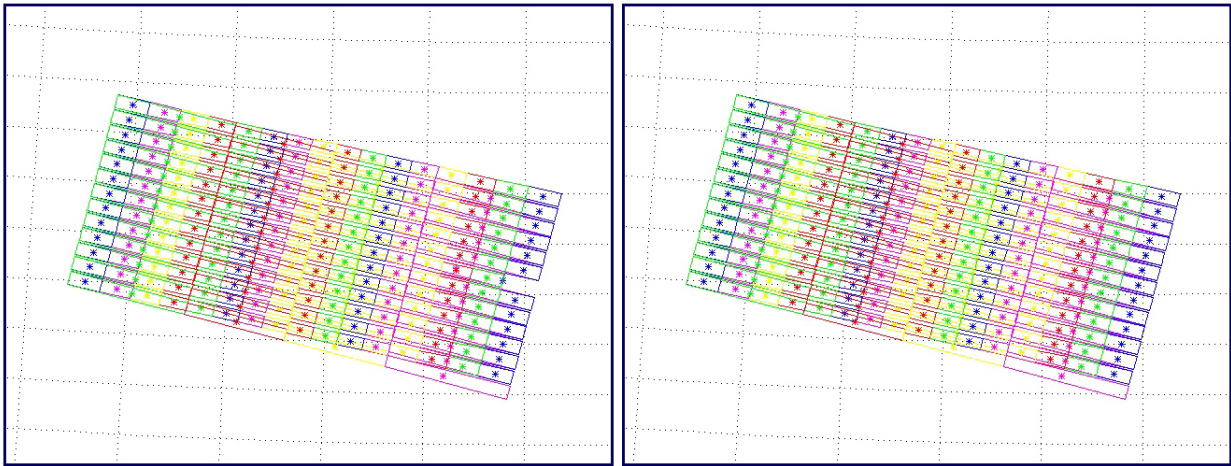

Fig. 3-8: Example for the successful correction of the scanner encoder values. The figure shows the ground pixels of a nadir state. Left: Before correction with the erroneous readout obvious as a gap in the readouts. Right: After correction.

Another change, implemented on a fast track after delivery of the algorithm baseline, resulted from the modification of the final flight configuration when a state which regularly scans the lower thermosphere and mesosphere, the so-called *limb_mesosphere_thermosphere state* (see also section 3.6) was introduced. In the – currently operational – version 6.03 of the processor measurements from data generated by this state are not written to the Level 1b product. They are only available in the Level 0 data. Since such unprocessed data contain no information about the geolocation of the measurement it was decided to add a patch to the already delivered processor that writes the measurement data to the Level 1b product during Level 0-1 processing.

SciCal

The optimisation of the *Dead & Bad Pixel Mask (DBPM)* calculation was finished and implemented in SciCal version 2, which will become operational in 2009. An extended validation of the DBPM occurred by comparing the operational DBPM results with masks from a SRON calculation in the retrieval windows of CO_2, CH_4 and CO. The calculation speed of the mask was improved by a factor of 2. Additionally some updates of the build configuration were implemented making the compilation on 64 bit systems possible. However, work on the DBPM is not finished. Plans for the coming year include a pixel based DBPM and further optimisation of the mask using results of sensitivity studies done for Level 2 retrievals in the short wave infrared (SWIR) channels.

Scial1c

The new SciaL1c user tool was released to the public in October 2008. Compared to the previously released version the following changes were implemented:

- m-factor application
- revision of data set selection ('option –ds')
- improved error logging for easier maintenance.

In addition to the software changes, also the quality control was updated: The SciaL1c tool was developed as a replacement of the Java tool from the ESA maintained *EnviView* package with the intention to speed up the development of the tool and allow easier harmonisation with the Level 0-2 processing chain. Therefore the original test approach for the factory acceptance relied for a large part on the comparison of the output of the Java tool and the new tool. In the meantime the SciaL1c tool evolved and contains now several features which have not been available so far. As a consequence, the test approach, procedure and requirements had to be updated. The proposal for the new testing was

accepted by ESA and incorporated in the new test system, which was successfully used for the factory acceptance test of the new version of SciaL1c.

Early 2009 a Windows version of the SciaL1c, developed by IMF under an ESA contract, will be released. Furthermore the development of a platform independent graphical user interface is under discussion.

3.5   SCIAMACHY Level 1b-2 Processing

G. Lichtenberg, A. Doicu, S. Gimeno-García (TUM), S. Hrechanyy, K. Kretschel, M. Meringer, F. Schreier

In 2008 the verification of the version 4 of the off-line processor was completed and the processor was delivered to ESA. In addition the implementation of the next version 5 of the processor has started. It is planned to finish the implementation and verification in February 2009.

Level 1b-2 OL Processor Version 4 Verification Results
New features of the version 4 processor include

- switchable calibration options for nadir trace gas retrievals
- application of m-factors to correct instrument degradation
- new Aerosol retrieval algorithm
- new nadir product BrO slant column densities
- new nadir product SO2 slant column densities
- optimisation of limb retrieval settings.

All changes were successfully verified in collaboration with the SCIAMACHY Quality Working Group using about 150 orbits of Level 1b data which were processed by DLR with the Level 0-1 prototype. Figures 3-9 to 3-11 show examples for the new SO_2 slant column retrieval and the limb retrieval. Further details can be found in the verification report of the SQWG.
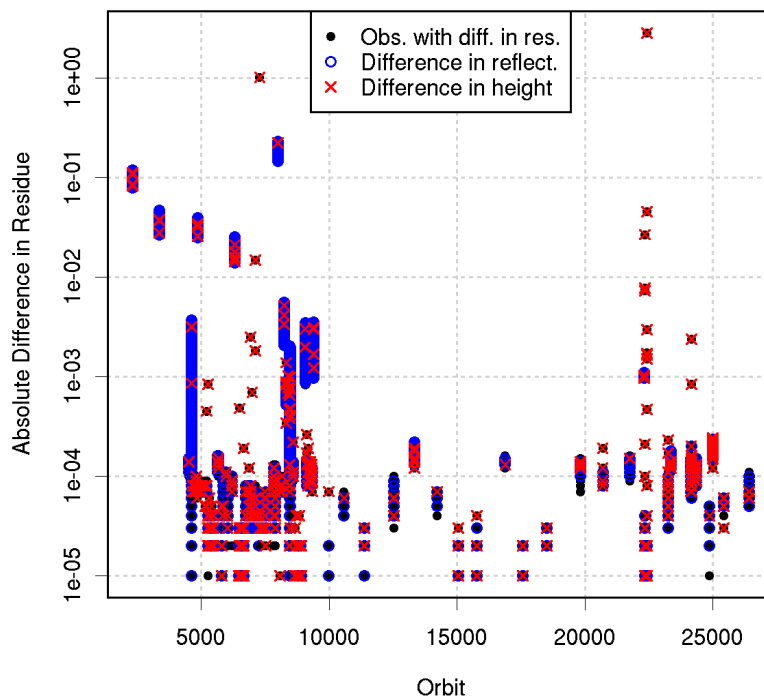
Fig. 3-9: Verification of the absorbing aerosol retrieval. Shown is the absolute difference between the reference algorithm by KNMI/SRON and the operational retrieval. Of the 696512 data records, 99.1% had differences < 0.1. All differences can be explained by the usage of a different topographic database and the operational interpolation of the sun reference spectra and the Earthshine spectra to the same wavelength grid not done in the reference algorithm.

DLR SO₂ Slant Column 20060811
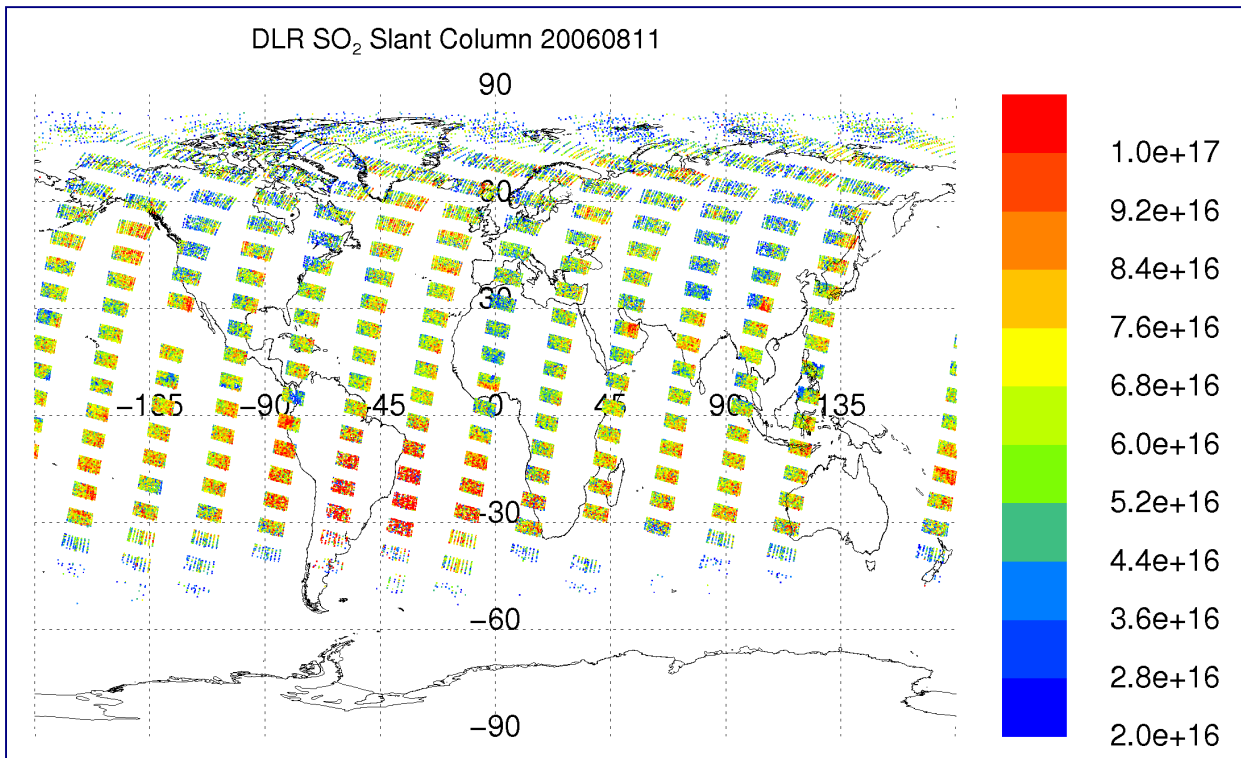
Fig. 3-10: Global map of SO₂ slant columns for November 8, 2006.
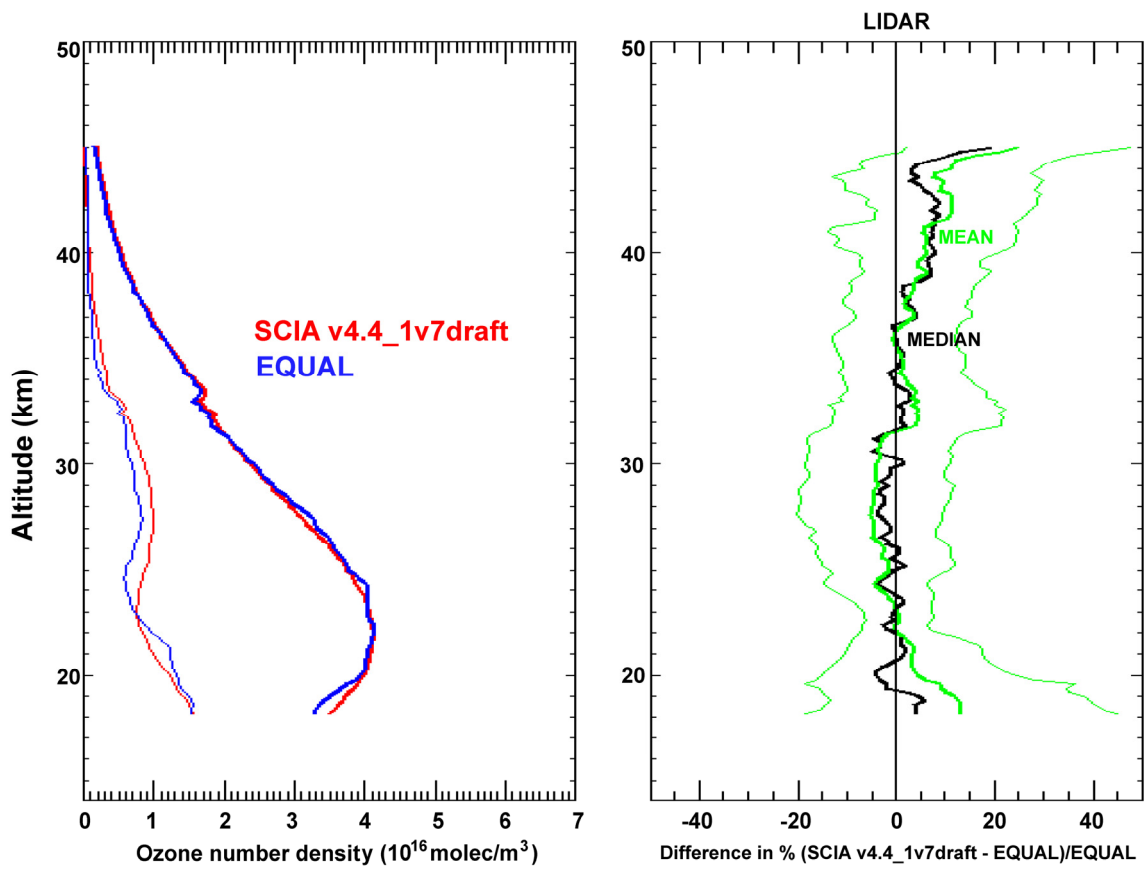
Fig. 3-11: Validation of limb ozone profiles from the EQUAL project. Shown is the mean profile of 14 SCIAMACHY orbits above 18 km and co-located LIDAR measurements (left) and the deviation between the SCIAMACHY processed data and the LIDAR data (right, plot by A. v. Gijsel, RIVM).

The implementation of the next version of the off-line processor, i.e. version 5, is almost finished. The major changes compared to the previous version comprise the introduction of

- two types of total column densities for SO_2 (volcanic and anthropogenic)
- BrO total columns and BrO limb profiles
- H_2O total column density
- OClO slant columns
- CO total 'dry' columns from the SWIR range
- limb cloud flagging.

The introduction of total columns for SO_2 and BrO is the logical continuation of the implementation of the slant column densities in the previous version of the processor. The scientific algorithms forming the basis of the operational implementation were developed by IUP/IFE, University of Bremen (SO_2) and BIRA (BrO). The H_2O retrieval is based on AMC-DOAS developed by IUP Bremen *(Noël et al. 2005)*. Total columns are directly retrieved without an intermediate slant column step. OClO total column retrieval was originally foreseen for implementation in 2009. However the off-line processor delivered promising results in initial tests (see figure 3-12). Since OClO is an important indicator for chlorine activation, it was decided to fast track the implementation. It is based on a scientific algorithm provided by IUP/IFE, University of Bremen *(A. Richter, 2006)*.
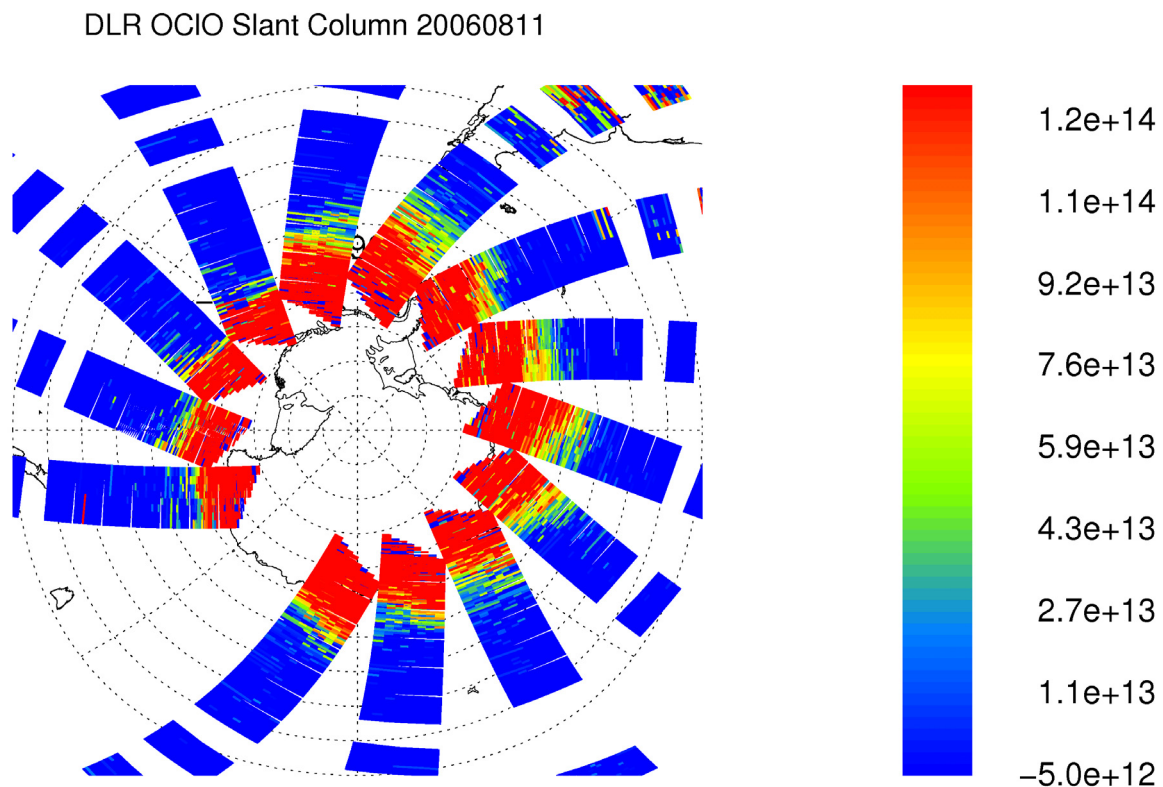
Fig. 3-12: First results for the operational OClO retrieval over the South Pole on August 11th, 2006.

The CO retrieval was an in-house development by IMF-AP (see chapter 3-9). The limb processor by IMF-AP (see annual report 2007) was extended by adding the retrieval of BrO profiles. A first comparison with balloon data and BrO retrievals from other institutes is shown in fig. 3-13.
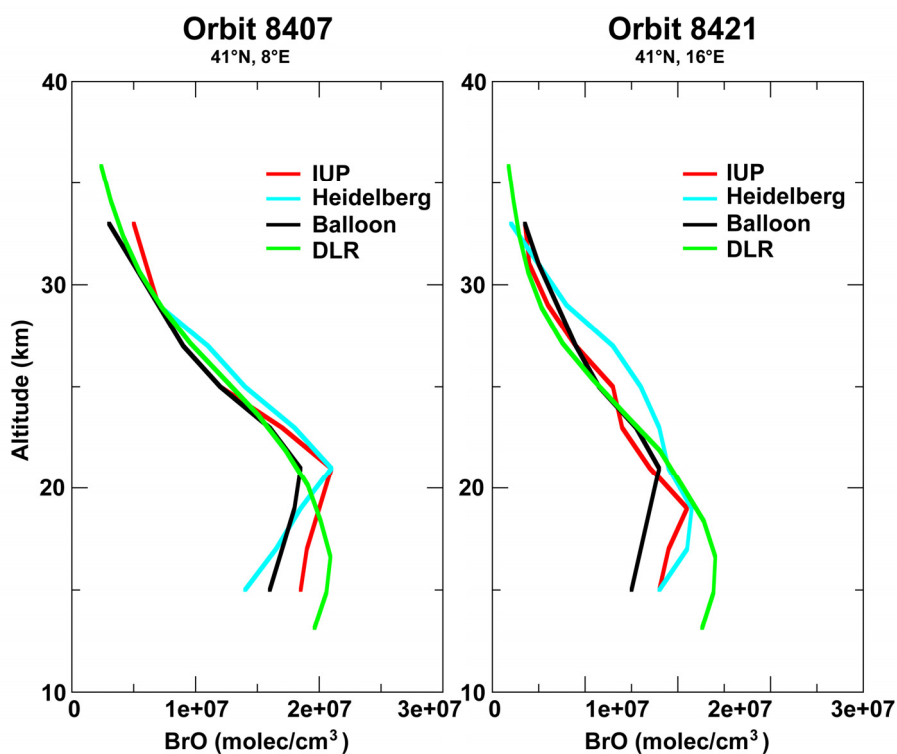
Fig. 3-13: Comparison of different retrievals using SCIAMACHY data and airborne DOAS (black). The retrievals are from DLR (green), IUP/IFE (red; see e.g. *Rozanov et al., 2005*) and the University of Heidelberg (cyan; *Kühl et al., 2008*).

References

Kühl, S., J. Pukite, T. Deutschmann, U. Platt, T. Wagner: SCIAMACHY limb measurements of NO_2, BrO and OClO. Retrieval of vertical profiles: Algorithm, first results, sensitivity and comparison studies, Adv. Sp. Res., 42, 1747-1764, 2008

Noël, S., M. Buchwitz, H. Bovensmann, J.P. Burrows: SCIAMACHY Water Vapour Retrieval Using AMC-DOAS, Proceedings of ENVISAT/ERS Symposium, ESA Special Publication 572, 2005

Richter, A.: Algorithm Description SCIAMACHY OClO slant columns, Technical Note, 2006, available at http://www.doas-bremen.de/manuals/ad_iup_bremen_oclo_nadir.pdf

Rozanov, A., H. Bovensmann, A. Bracher, S. Hrechanyy, V. Rozanov, M. Sinnhuber, F. Stroh, J.P. Burrows: NO_2 and BrO vertical profile retrieval from SCIAMACHY limb measurements: Sensitivity studies, Adv. Sp, Res., 36, 846-854, 2005

SQWG: SCIAMACHY Level1b-2 data processing: Verification Report OL V 4.0, Technical Note, ENV-VPR-QWG-SCIA-0095, issue 1, 2008

3.6   SCIAMACHY Operations Support

M. Gottwald, E. Krieg (TwIG), K. Reissig (IBR), J. How (TwIG)

Assuming that ENVISAT will successfully operate until 2013, the past year marked 'halftime' for the in-orbit activities of the SCIAMACHY Operations Support Team (SOST), formed by personnel from IMF-AP and IUP-IFE/University of Bremen. We continued to closely collaborate with representatives from the Quality Working Group (SQWG) and ESA (flight operations at ESOC, post launch support at ESTEC and payload data segment at ESRIN).

The routine work – mission planning, weekly monitoring – of SOST did not attract too much public attention which implicitly means that instrument operations were running rather smoothly. This is obvious in the annual statistics indicating that the overall instrument availability remained to be high (fig. 3-14). From a total of 5240 orbits only 84 could not be used since SCIAMACHY had been transferred to a mode lower than MEASUREMENT TIMELINE. Thus measurements were executed in slightly more than 98% of all possible orbits. Within each orbit more than 90% of the orbital period were covered with states (scientific or calibration & monitoring). Fig. 3-14 shows that most of the unavailabilities were caused by planned out-of-plane orbit control manoeuvres (OCM) while anomalies are limited to short sporadic periods. The instrument related anomalies can be attributed to Single Event Upsets (SEU), i.e. high energy particles impinging onto instrument electronic components. On platform level an anomaly of the High Speed Multiplexer controlling the on-board data traffic of all ENVISAT instruments required a brief MEASUREMENT IDLE phase for SCIAMACHY.
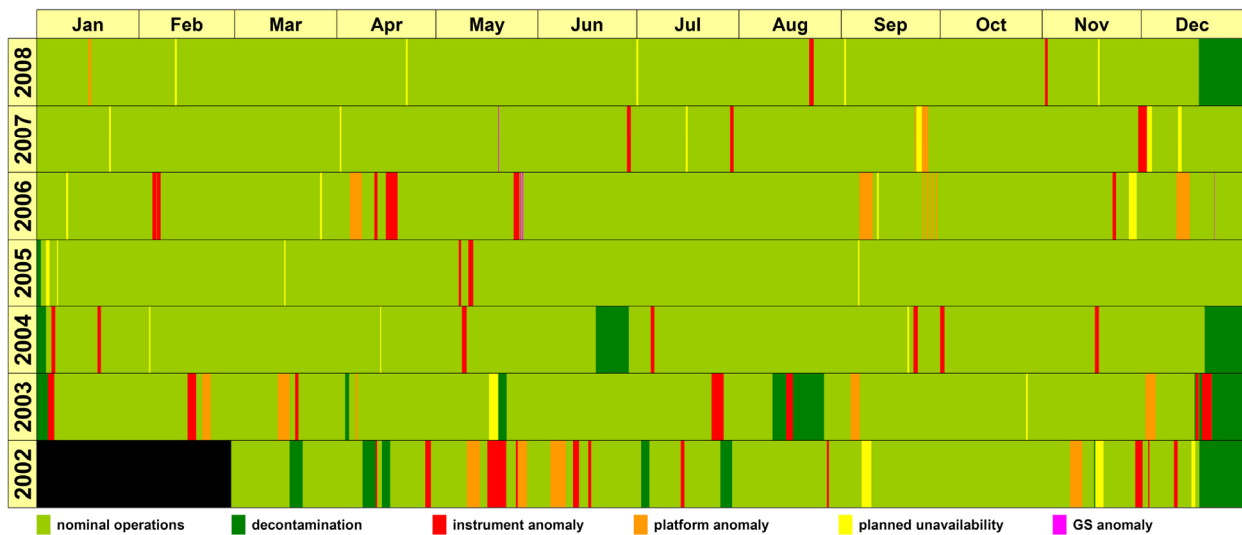
Fig. 3-14: Instrument availability since launch

Even on a monthly basis the availability did not drop below 95% (fig. 3-15). For the majority of months all measurements planned were successfully executed.
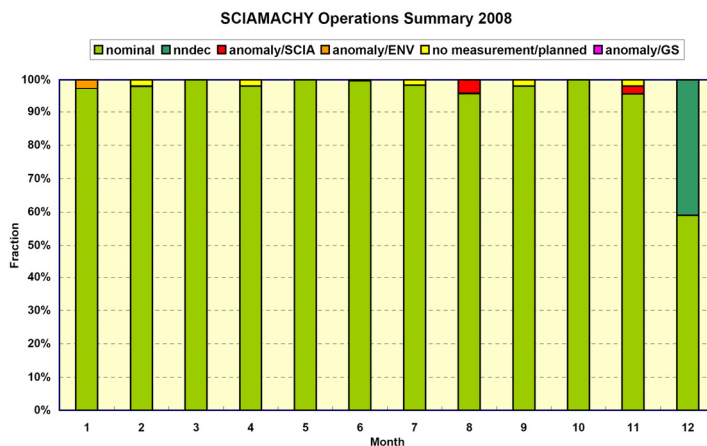
Abb. 3-15: Availability in 2008 on a monthly basis

21

Besides of the routine operation tasks the analysis, preparation and implementation of *Operation Change Requests (OCR)*, transferring SCIAMACHY's routine final flight status into a temporary non-nominal configuration, required significant efforts. From 2003-2008 a total of 39 OCRs have been issued with only one being withdrawn. Thus instrument operations changed every 2-3 months. In 2008 8 OCRs were tackled. They addressed issues such as

- straylight
- phytoplankton
- improved coverage in validation campaigns
- limb_only orbits
- limb_mesosphere_thermosphere.

The OCR requesting regular measurements in the mesosphere and lower thermosphere could only be achieved by modifying the final flight configuration permanently. A dedicated limb_mesosphere_thermosphere state was implemented, together with a full new timeline set, including 4 timelines executing this state in about 30 orbits per month. These orbits have to be scheduled in two blocks of 15 orbits each whereby one block should be synchronized with MIPAS operating in *Upper Atmosphere* mode.

Thermal Operations

The degradation of the thermal systems (TC and ATC) made it necessary to occasionally adjust thermal parameters. For the TC system this occurred in January and April and was more or less a standard procedure. Since June 2002 a total of 21 TC adjustments have been executed. For the ATC the story is different because for more than 6 years the ATC parameters (3 setpoints and 3 gain factors) remained stable. However the degrading average ATC nadir heater power began to closely approach its lower limit around the time of the seasonal minimum around November/December. For 2008 it could be expected that a stable OBM temperature could no longer be maintained for all orbital phases. Therefore for the first time since June 2002 an ATC adjustment was necessary. Details were worked out by SOST based on the existing – mostly pre-launch – information and discussed with Astrium and Dutch Space. The selected approach raised the ATC nadir heater power and lowered the corresponding limb value by the same amount leaving the ATC RAD A heater power unmodified. Thus an almost non-changing OBM temperature could be expected. This option shall permit stable ATC operations for the next few years. The adjustment was successfully executed mid October. Fig. 3-16 illustrates how the ATC temperatures changed during the adjustment.
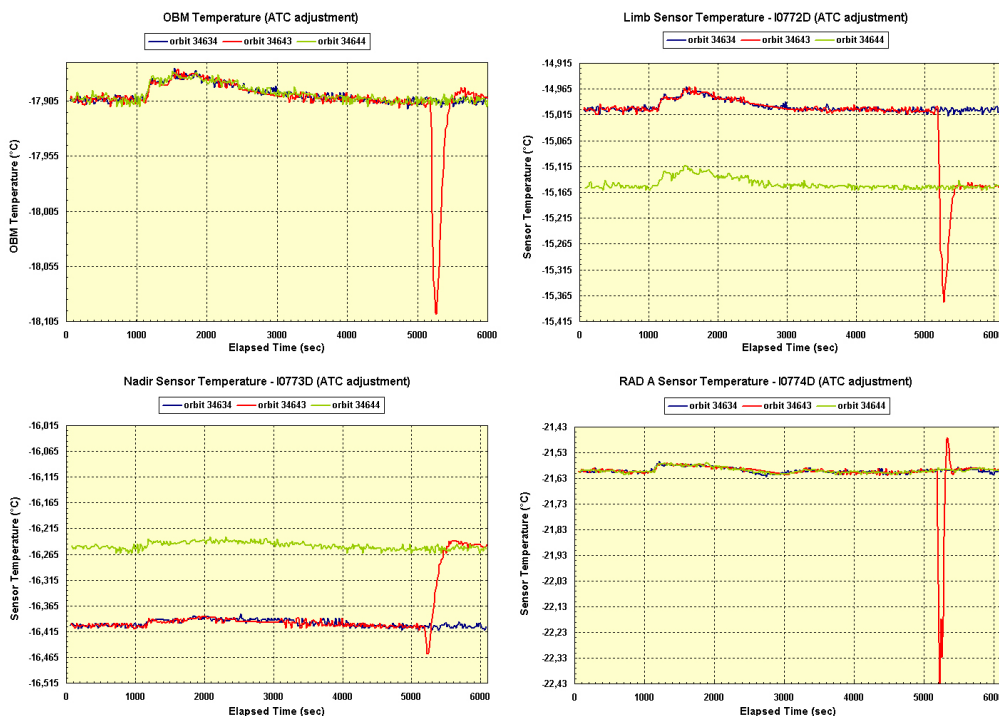
Abb. 3-16: ATC temperature change during the 2008 ATC adjustment in orbit 34643

SCIAMACHY operations information was made publicly available via the SOST webpages (http://atmos.af.op.dlr.de/projects/scops/). Modifications of these pages have been started to account for their growing content, particularly in the light of the mission extension by several more years.

3.7 SCIAMACHY Scanner Monitoring

M. Gottwald, E. Krieg (TwIG)

During the specified mission lifetime both SCIAMACHY scanners, the azimuth scanner (ASM) and the elevation scanner (ESM), were considered uncritical in terms of degradation. Therefore they were not treated as Life Limited Items (LLI) and no regular monitoring was required. The situation changed when the first mission extension began in March 2007. For the second extension until the end of 2013 this activity is required even stronger.

Scanner monitoring has been implemented by SOST in 2007. Since no dedicated scanner monitoring procedures existed, SOST derived two indirect methods

- Scanner currents during state 65 execution: State 65 is scheduled each orbit. Therefore HK telemetry provides good statistics even though the measurement phase of state 65 only lasts about 45 sec. With a rate of 1/16 Hz about 2-3 telemetry readings are obtained each state execution. Due to the design of state 65 a distinct current pattern – for clockwise, counterclockwise and mean current – is expected. No change of this pattern is considered as an indication that the scanner performance does not degrade. If necessary, the currents can in addition be elaborated from other types of states with distinct scanner movements, e.g. nadir, limb.
- Elevation and azimuth jumps in Sun states: It is known since the Commissioning Phase that during execution of particular Sun states (occultation – states 47 and 49, subsolar – state 53) the ESM and ASM readings display a small jump when scanner control is switched from predicted position to Sun Follower. Recently it was shown (see annual report 2007) that all except one of these jumps can be attributed to an extra-misalignment of SCIAMACHY's LoS. As long as the jump patterns do not change the performance of the complete chain leading to an accurate LoS pointing is interpreted not to change. This chain includes the scanners but also items as e.g. scheduling parameters derived on-ground in SCIACAL, platform stability or Sun Follower performance. Therefore this method is less robust than monitoring scanner currents.

Scanner Currents
Two state 65 related scanner current activities were pursued by SOST. In order to improve the temporal resolution of the HK telemetry, 4 orbits were executed in June with the *Non-Nominal Telemetry* format commanded for state 65 execution. This resulted in ASM/ESM scanner readouts every second. Analysis yielded highly resolved current profiles for both scanners which matched perfectly (fig. 3-17) serving as a reference for future investigations.
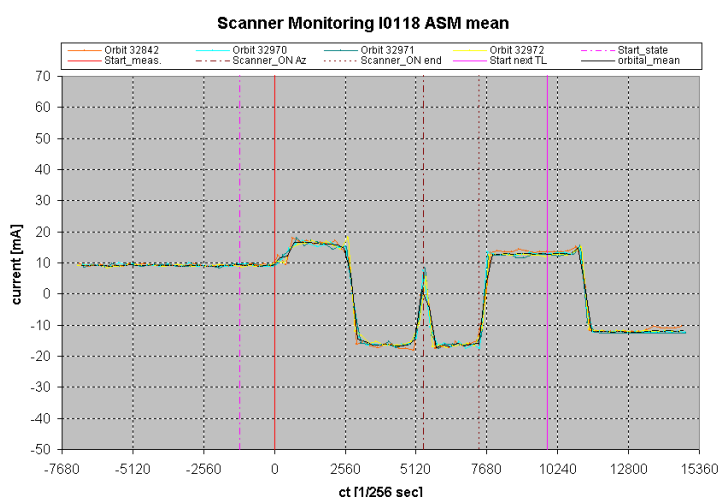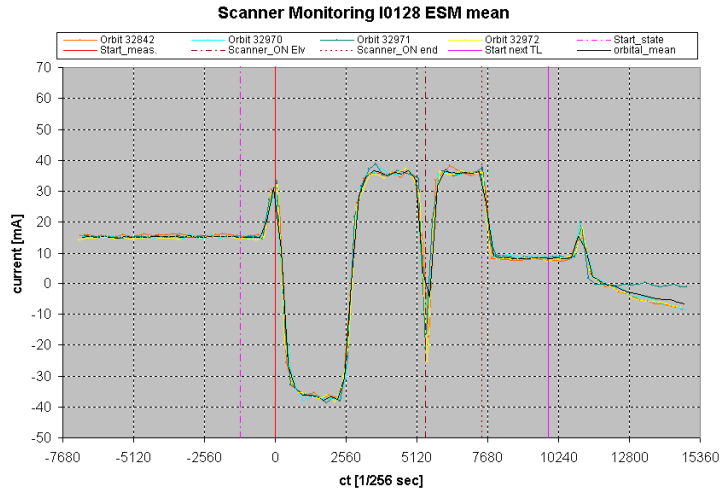
Fig. 3-17: ASM (top, previous page) and ESM (bottom) scanner current profile in 4 orbits with 1 sec time resolution

The individual segments in fig. 3-17 can easily be attributed to the individual state phases (360° clockwise and counterclockwise rotations for scanner maintenance and scanner encoder calibration). Particularly interesting are the plateaus which originate from periods with continuous scanner movements. These plateaus, although embedded in a high scatter, also stick out in the standard *Realtime* HK format (fig. 3-18) when one reading every 16 sec has a large probability to fall into one of such longer lasting plateaus.

For long-term scanner monitoring purposes all current telemetry parameters from 2002 onwards has been analyzed. Fig. 3-18 presents examples for the ASM/ESM mean currents of the state 65. While the ASM shows no peculiarities, the ESM readings begin to increase around the turn of 2007/2008 (orbit 30000) but seem to level off again in the second half of 2008. For comparison a nadir, a limb and a Sun occultation state have been analyzed in the same manner without showing similar ESM behaviour. The case of the state 65 ESM current needs further investigations since the mean current is monitored on-board with a limit set at ± 66.5 mA. Violation of this limit would cause a transfer to a mode lower than MEASUREMENT. Astrium has started a detailed study to understand this behaviour and to propose countermeasures, if considered necessary.
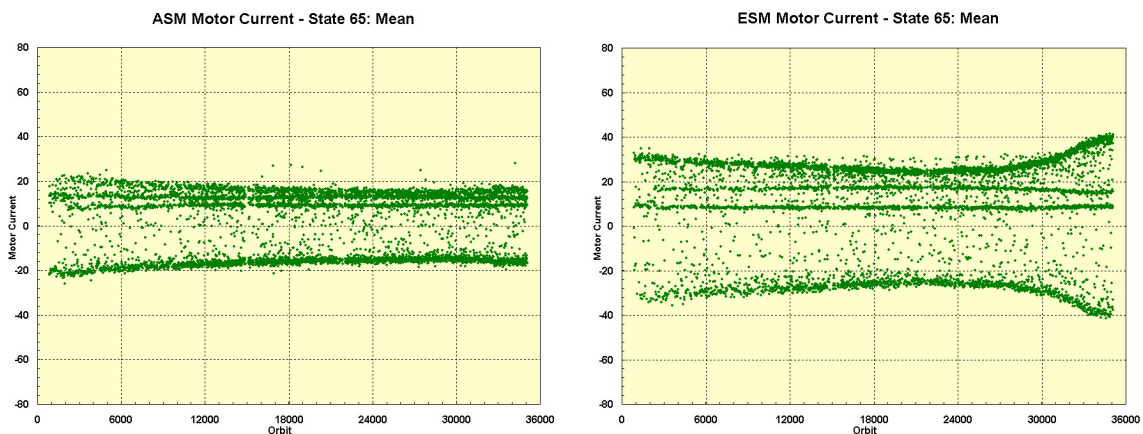
Fig. 3-18: Mean ASM (left) and ESM (right) scanner current from 2002-2008

ASM/ESM Jumps
The jump analysis was continued. In fig. 3-19 only the ESM jump at Sun Follower acquisition during the Sun occultation state displays an increasing scatter. We relate it to a slightly stronger wobble of ESM readouts after acquisition. What causes this behaviour is presently unclear. A direct link to the reported ESM scanner current behaviour (see above) seems unlikely because the scatter increase occurs continuously since the early orbits, contrary what is obvious in fig. 3-18. Although the observed effect is small and does not impact operations and data quality, we continue its full monitoring as a potential analysis useful for preventive measures.

24
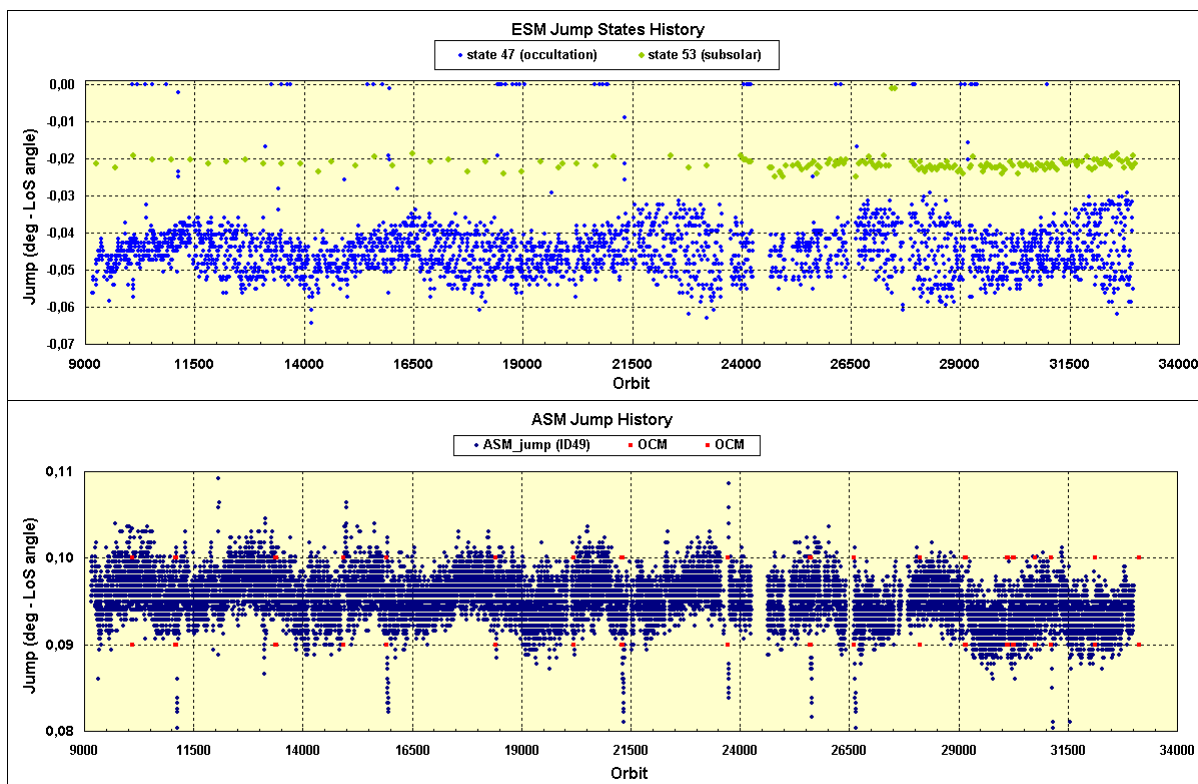
Fig. 3-19: ASM/ESM jumps in solar states from 2002-2008

3.8 SCIAMACHY Consolidated Level 0 Data

M. Gottwald, E. Krieg (TwIG), K. Reissig (IBR), J. How (TwIG)

SOST maintains a master archive of consolidated level 0 (cL0) data in the Data Information Management System (DIMS) environment of the German Remote Sensing Data Center (DFD) at DLR. Details of the master archive generation can be found in the 2007 annual report of IMF-AP. In brief, this archive was established because it

- reflects best the planned measurements (from ANX to ANX) and is therefore considered to be a means for the final verification of operation implementation.
- it defines the basis for reprocessing in the PDS.

Consolidated level 0 data are transferred to DIMS once they passed a sequence of checking routines. These verify the integrity of specific cL0 product properties. Usually two of such processes are running in parallel. In the first most recent cL0 products received from the D-PAC undergo quality checking. This provides for a continuous update of the master archive. Since occasional cL0 data availability interrupts, e.g. late delivery or incomplete consolidation, cause gaps in the cL0 record, a second procedure deals with past orbits where the first process had failed. In a handshaking interface between SOST and ESRIN all orbits for the years 2002 (start of quasi-routine operations on August 2nd) to December 31st, 2007 with missing or incorrect cL0 products were identified and reconsolidated. If necessary, reconsolidation even occurred twice.

By the end of 2008 more than 30000 cL0 products have been successfully quality checked and transferred to DIMS. The statistics for the years 2002-2007 is displayed in fig. 3-20. For this period the statistics of orbits with fully consolidated level 0 products is considered to have reached its final status. For comparison the year 2008 results are only preliminary because they only reflect the status after the

first continuous quality check without any reconsolidation. The detailed cL0 availability on single orbit level is given at the SOST website (http://atmos.caf.dlr.de/projects/scops/).

cL0 Availability
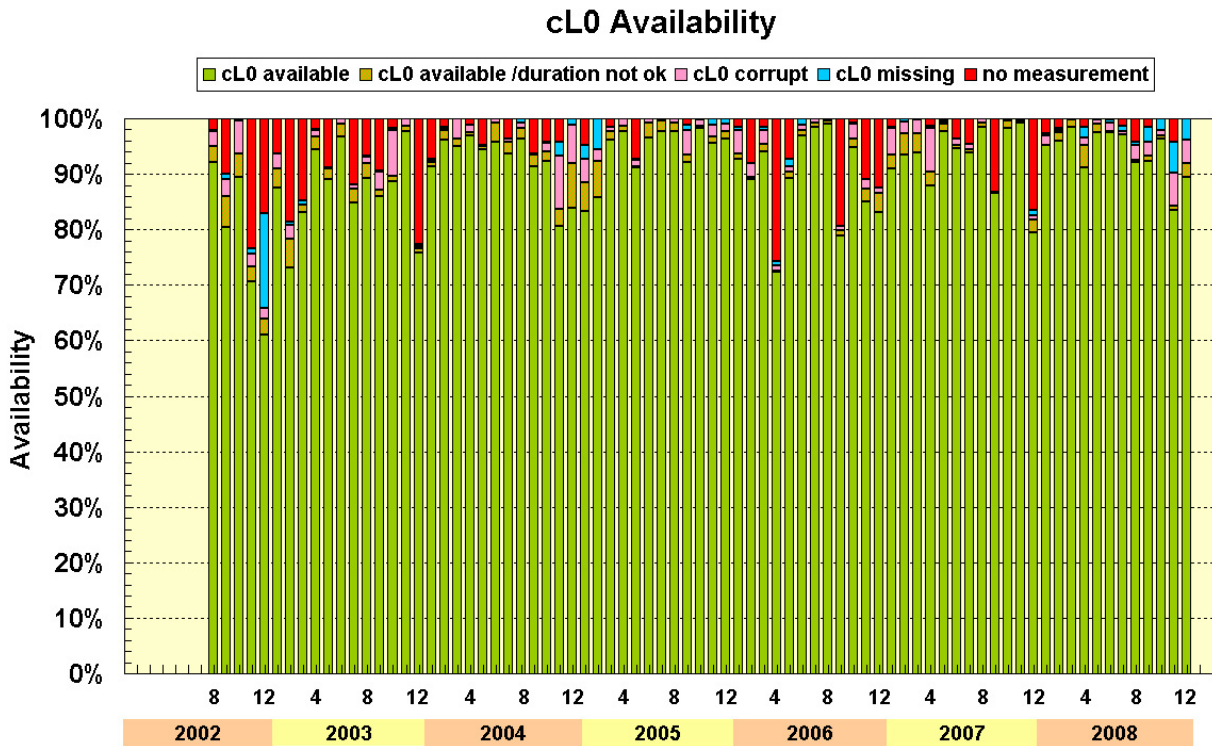
Fig. 3-20: cL0 statistics for the years 2002-2007 (final) and 2008 (preliminary).

Although the figures illustrated in fig. 3-20 already indicate a high value of more than 95% of all orbits in consolidated form our goal is to improve this figure further. Consolidated L0 products with incomplete but otherwise correct content, i.e. not corrupt due to data anomalies like e.g. Reed-Solomon or sync bit errors, can also be analyzed by the operational processors. Therefore our next step is to estimate the percentage of useful data in such orbits and to transfer the accordingly flagged products to DIMS as well. We expect to finally achieve about 97-98% of the planned measurements to be available as cL0 products.

3.9 CO from SCIAMACHY's Short Infrared Wavelength Channels

F. Schreier, S. Gimeno-García (TUM), G. Lichtenberg, S. Slijkhuis, A. Doicu, M. Hess (RASCIN)

Nadir observations in the shortwave infrared (SWIR) channels of SCIAMACHY can be used to derive information on CO, CH_4, N_2O, CO_2 and H_2O. BIRRA (Beer InfraRed Retrieval Algorithm) is a nonlinear least squares fit developed for nadir vertical column density sounding in the near infrared. In the framework of the ongoing code verification, a careful intercomparison of BIRRA with independent retrieval results has been performed.

Theory and Algorithm
The intensity (radiance) I at wavenumber ν received by an instrument is described by the equation of radiative transfer. In case of nadir infrared sounding this can be simplified to

$$F(x) \equiv I(\nu) = r(\nu) I_{sun}(\nu) \exp\left(-\sum \alpha_m \tau_m(\nu)\right) \otimes S(\nu, \gamma) + b(\nu) \tag{1}$$

where τ_m is the optical depth along the entire line-of-sight (Sun-ground-satellite) for the reference atmosphere. $S(\nu, \gamma)$ is the spectral response function, and r and b denote surface reflectivity and baseline correction modelled by low order polynomials in wavenumber. The state vector **x** to be retrieved comprises the scaling factors α_m for the molecular number densities $n_m(z)$, the slit function half width γ, and polynomial coefficients for reflectivity and baseline. The standard approach to estimate the unknown **x** from a measurement vector **y** relies on (nonlinear) least squares

$$min_x |\mathbf{y} - F(\mathbf{x})|^2 \tag{2}$$

where $F(\mathbf{x})$ denotes the forward model (1) describing radiative transfer and instrument. Note that the reflectivity and baseline coefficients enter the forward model linearly and the least squares problem can be reduced to a separable least squares problem. For the solution of the least squares problem, BIRRA uses solvers provided in the *PORT Optimization Library* based on a scaled trust region strategy.

To compensate for variations of the meteorological conditions (e.g. pressure) and for instrumental artefacts (e.g. calibration, slit function, ice layer on detector), the vertical column density of CO is derived as

$$xCO = N_{CO} \times \frac{\alpha_{CO}}{\alpha_{CH4}} \quad where \quad N = \int n(z) dz$$

Furthermore, column densities are averaged in 1° latitude/longitude bins with doubtful values rejected:

- PORT least squares converged with residual norm decreased
- no 'forbidden' x values (e.g. negative column densities)
- scaling factors: $0 \leq \alpha_{CO} \leq 1.2$ and $0.7 \leq \alpha_{CH4} \leq 1.3$ (where α_{CH4} is throughput corrected)
- latitudes in the interval [80S,80N], only overland.

BIRRA Retrievals of Carbon Monoxide Column Densities for 2004
Carbon monoxide (CO) is an important trace gas affecting air quality and climate. It is highly variable in space and time. About half of the CO comes from anthropogenic sources (e.g. fuel combustion), and further significant contributions are due to biomass burning. CO is a target species of several spaceborne instruments, i.e. for AIRS, MOPITT, and TES from NASA's EOS satellite series, and MIPAS and SCIAMACHY on ESA's ENVISAT.

For the retrieval of carbon monoxide vertical column densities with BIRRA, level 1 data of SCIAMACHY channel 8 applying the IUP-Bremen bad/dead pixel mask have been used. Hence a single spectrum comprises 51 data points in the interval 4282.68615 to 4302.13102 cm^{-1}, i.e. 2.3244 µm to 2.3350 µm. Pressure and temperature profiles were taken from the COSPAR International Reference Atmosphere (CIRA) providing data for each month and 34 latitudes. An US standard atmosphere was assumed for the molecular density profiles. Surface reflectivity was modelled with a second order polynomial, baseline was ignored.

The annual average of 2004 CO vertical columns is shown in fig. 3-21. Monthly mean CO columns for February, April, and September 2004 (see fig. 3-22) were compared with results of other SCIAMACHY near infrared retrieval algorithms, e.g. the Weighting Function Modified DOAS (WFM-DOAS, developed by University of Bremen, see *Buchwitz et al. 2007*) and the Iterative Maximum Likelihood Method (IMLM, developed by SRON Netherlands Institute for Space Research, see *Gloudemans et al. 2006*). February is representative for Winter, April for Spring and September for the transition from Summer to Autumn in the Northern hemisphere. Moreover, intercomparisons of the SCIAMACHY carbon monoxide occurred with data *(McMillan et al. 2005)* retrieved from AIRS (Atmospheric Infrared Sensor aboard NASA's AQUA satellite, see *Chahine et al. 2006*).
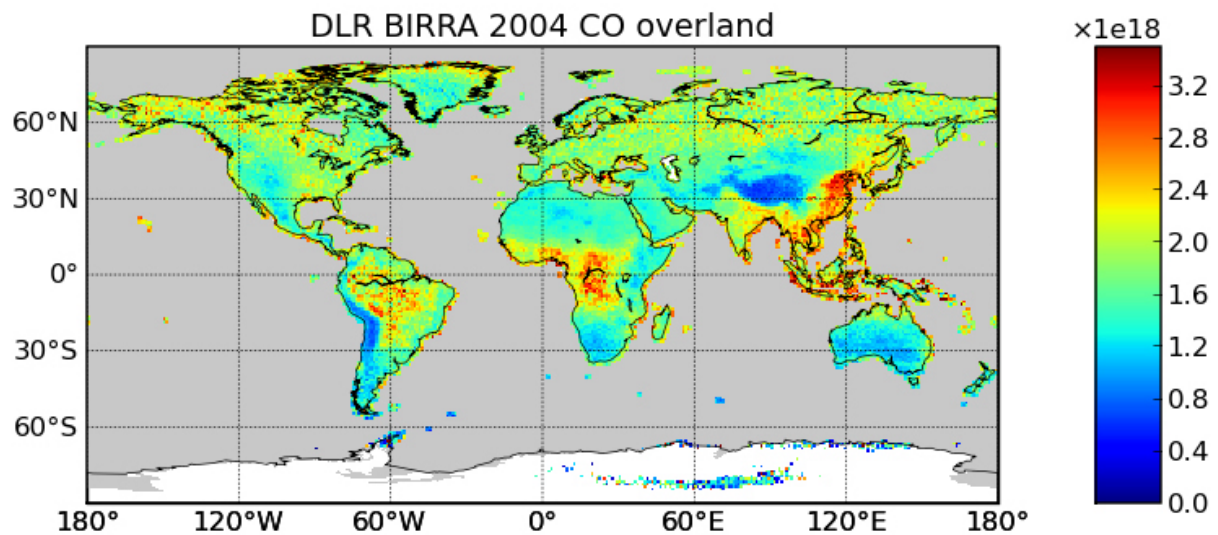
Fig. 3-21: Mean CO column density in 2004 as derived with BIRRA from SCIAMACHY data.
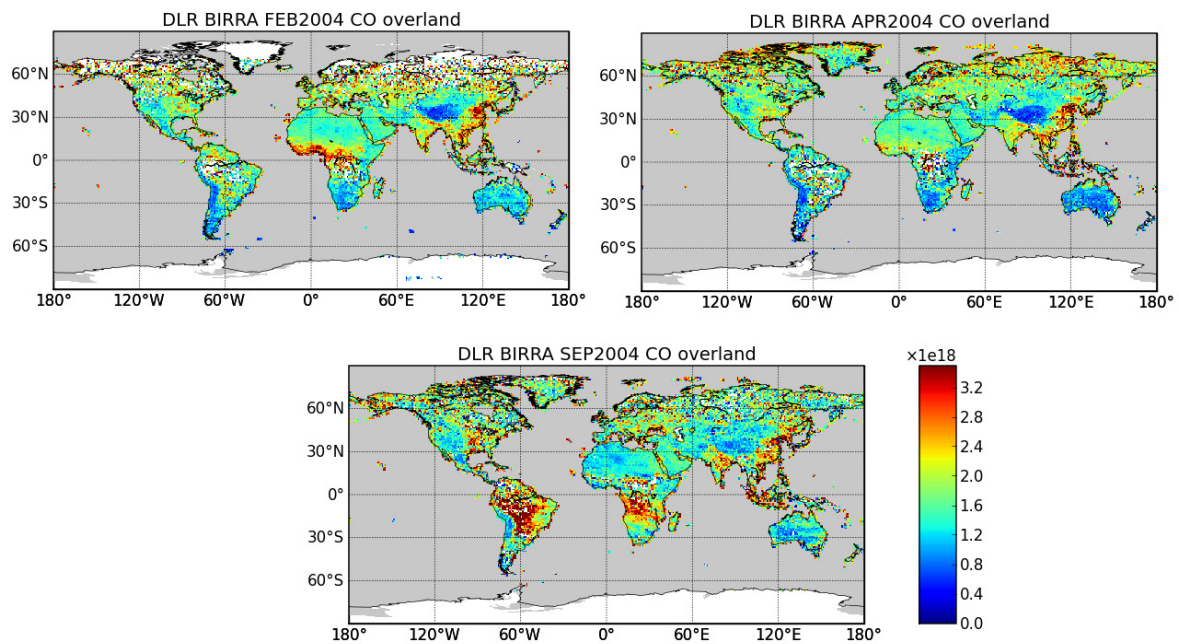
Fig. 3-22: Monthly mean CO column densities from February, April and September 2004 as derived with BIRRA from SCIAMACHY data.

28

Since CO being a very weak absorber in the near infrared, the results are highly sensitive to the bad/dead pixel mask and to the correct filtering of dubious retrieval results. Despite significant conceptual differences of the three SCIAMACHY codes w.r.t. forward modelling and inversion, a good overall agreement has been found.

The BIRRA 'prototype' code was originally developed in FORTRAN77 and has been upgraded to modern Fortran 95/2003 in 2008. Integration of the 'new' code into the operational SCIAMACHY Level 2 processing environment has been started and is expected to become operational in 2009.

Methane CH4 is the second most important greenhouse gas and has strong absorption features in the SWIR channels of SCIAMACHY. Preliminary retrievals with BIRRA using channel 8 have been performed recently. A more thorough investigation of CH4 retrieval, the extension of CO retrieval beyond 2004, and a better modelling of aerosol and clouds will be major tasks for the following year.

References

Buchwitz, M., I. Khlystova, H. Bovensmann, and J. P. Burrows: Three years of global carbon monoxide from SCIAMACHY: comparison with MOPITT and first results related to the detection of enhanced CO over cities, Atm. Chem. Phys. 7, 2399-2411, 2007

Gloudemans, A., H. Schrijver, O. Hasekamp, and I. Aben: Error analysis for CO and CH4 total column retrievals from SCIAMACHY 2.3 µm spectra, Atm. Chem. Phys. 8, 3999-4017, 2008

Chahine, M.T. et al.: AIRS – Improving weather forecasting and providing new data on greenhouse gases, Bull. Am. Met. Soc., 87:911-926, 2006

McMillan, W.W. et al.: Daily global maps of carbon monoxide from NASA's Atmospheric Infrared Sounder, Geophys. Res. Letters, 32:L11801, doi: 10.1029/2004GL021821, 2005

3.10 Processor Development for ADM-Aeolus

D. Huber (DoRIT), T. Trautmann

As the fourth of the ESA Earth Explorer missions the ADM-Aeolus mission is planned for launch in 2011. Being a scientific mission its goal is to demonstrate that the space-borne Doppler wind lidar (DWL) technique can be exploited to determine atmospheric wind velocity profiles. The *World Meteorological Organization* identified the need for accurate and vertical high-resolution wind observations as a key ingredient for the global observation of the Earth's atmosphere. ADM-Aeolus' baseline mission objectives comprise provision of averaged wind profiles over ocean and land in a total of 24 configurable vertical layers having currently the resolution of 250 m, 500 m, 1000 m and 2000 m in the altitude regions 0 to 2 km, 2 to 16 km and 16 to 26 km, respectively.

The currently defined ADM-Aeolus product levels are listed in table 3-1.

Product level	Description	Typical product size (MB per orbit)	Remarks
Level 1B	HLOS winds, only engineering-corrected	21-70	NRT product; spectrometer data processed to HLOS wind profiles without taking scene classification and p,T dependent Rayleigh-Brillouin scattering into account.
Level 2A	Layer optical properties for aerosol and cloud	7-10	ADM-Aeolus signals to provide information on aerosol and cloud layers Offline product for the optical properties of aerosol and cloud layers: altitude, geometric depth, optical depth, backscatter-to-extinction ratio and the scattering ratio (see *Flamant et al. 2008*).
Level 2B	Meteorologically representative HLOS winds	13–18	HLOS wind profiles based on algorithms using (i) scene-classification procedure and (ii) explicit correction for Rayleigh-Brillouin scattering effects by making use of p,T estimates from short-range forecast NWP models. Subset of Level 2C products. Available shortly after near-real-time for operational products generated at ECMWF.
Level 2C	Wind vectors determined from ADM- Aeolus	19–24	Adds ECMWF analysed winds (2 horizontal components) at the ADM-Aeolus locations, and supplementary product confidence data derived via assimilation of Level 2B data at ECMWF. Superset of Level 2B products.

Table 3-1: Product definition for the ADM-Aeolus mission, see *Tan et al. (2008)*

The processing of Level 1B to Level 2A products involves the following main steps:

- The Level 1B data represent the altitude range bin (layer) accumulated backscattered lidar signals on the spatial measurement scale.
- A feature finder algorithm is exploited to determine from these lidar signals if the particular layer under consideration contains aerosol particles or clouds. In addition, by comparison with pre-defined filling cases (aerosol/cloud fills the layer partly or completely) the Level 2A processing algorithm will select a particular filling case which matches the observations best.
- Based on climatological information of *backscatter-to-extinction* ratios for typical aerosol and cloud layers, a processing algorithm involving the optical properties of any of the ADM-Aeolus Mie layers (from approximately 16 km altitude down to the surface) will provide as output the following quantities:
    - altitude and geometrical thickness of the layer
    - mean layer extinction coefficient for particles
    - backscatter-to-extinction ratio for particles
    - scattering ratio defined as the total backscatter coefficient (sum of particles and molecules) divided by the molecular backscatter coefficient.

Current Work in the Context of the ESA project
Within DLR the Institute of Atmospheric Physics (DLR-PA) leads the DLR internal ADM-Aeolus project. In this project IMF-AP's tasks involve the development of a DLR-owned Level 1B processor prototype. DLR's contributions will support ESA with respect to the optimisation and validation of the ALADIN instrument as well as the implementation of the operational processor for the ADM-Aeolus ground segment developed and implemented by industry.

For the Cal/Val phase of the ADM-Aeolus mission the goal of the DLR internal project is to develop a prototype processor for the determination of level 1B products (first wind profiles). Contrary to the operational ESA Level 1B processor, the DLR processor will use the latest state-of-the-art algorithms. Following this approach we are in the position to investigate – independent from the operational processing line – possible improvements and enhancements for the standard Level 1B wind profiles. In addition, the enhancement of the Level 2A aerosol and cloud products requires knowledge of the single-scattering properties of aerosol particles and clouds, since the back-scattering and extinction coefficients of the particulate material play a key role in the interpretation of the lidar signals.

Current Work in the Context of the ESA project
The ADM-Aeolus consortium consisting of the partners CNRS/GAME, DLR, IPSL, KNMI, DoRIT and IB Reissig performs the following tasks on pre-launch sensitivity analyses and code validation work related to the Aeolus Level 1B and Level 2A operational processors:

- release of updated Level 1B and 2A prototype codes
- components in support of the processing of ALADIN calibration modes
- release of the operational Level 1B and 2A processors and related documentation
- investigation of the operations concept on the Level 1B baseline algorithms and products as well as Level 2A products and calibration issues.

Closer to launch of the ADM-Aeolus mission (currently planned for begin of 2011) tasks such as specific in-orbit validation, calibration and maintenance tasks as specified in the Aeolus Commissioning and Cal/Val Plan (ESA, 2007) will be covered, too.

References

Flamant, *P., J. Cuesta, M.-L. Denneulin, A. Dabas, and D. Huber*: ADM-Aeolus retrieval algorithms for aerosol and cloud products, Tellus A, 60, 273-288, 2008

Tan, D., E. Andersson, J. de Kloe, A. Stoffelen, G.J. Marseille, P. Poli, M. Denneulin, A. Dabas, D. Huber, O. Reitebuch, P. Flamant, O. le Rille , and H. Nett: The ADM-Aeolus wind retrieval algorithms, Tellus A, 60, 191-205, 2008

ESA, 2007: ADM-Aeolus Commissioning and CalVal Plan (Ref. AE-PL-ESA-SY-002, September, 28, 2007), see: http://eopi.esa.int/esa/esa?cmd=aodetail&aoname=AeolusCalVal

3.11 New Inversion Methods for the GODFIT Package – a Contribution to GDP5

S. Otto, A. Doicu, D. Loyola

The general minimisation problem within the scope of the retrieval of trace gases can be formulated as a least squares problem. In the framework of the so-called Tikhonov regularisation one has to minimise the function

$$F(\mathbf{x}) \;=\; \left\| \mathbf{F}(\mathbf{x}) - \mathbf{y} \right\|^2 + \alpha \left\| L \cdot (\mathbf{x} - \mathbf{x}_0) \right\|^2$$

where $\mathbf{F}$ represents the forward radiative transfer model, $\mathbf{y}$ the measurement vector of the satellite instrument, L the regularisation matrix, α the regularisation parameter and $\mathbf{x}_0$ is the a priori (state) vector, i.e. the initial guess for the solution vector $\mathbf{x}$ of the entire problem. While the regularisation matrix represents a certain set of side conditions constraining the solution vector, the regularisation parameter is a measure for the strength of this constraint and determines how much the minimisation problem is affected by this term.

The minimisation problem can be solved numerically by performing an iteration which has to satisfy the relation

$$F(\mathbf{x}_{k+1}) \;<\; F(\mathbf{x}_k)$$

where the solution of the $(k+1)^{th}$ iteration $\mathbf{x}_{k+1}$ is calculated from the former solution $\mathbf{x}_k$. Convergence is obtained if a further relation

$$\left| F(\mathbf{x}_{k+1}) - F(\mathbf{x}_k) \right| \;<\; \epsilon$$

is fulfilled with a certain convergence parameter ϵ. Note that during each iteration the forward radiative transfer model has to be called which leads to a certain computational effort depending on the applied model and considered atmospheric constituents (such as auxiliary absorbing gases, scattering aerosols and clouds).

Various inversion methods arise from the treatment of the minimisation function: 1) It can be developed by a second order Taylor series to apply finally methods of the PORT library (Gauss-Newton and quasi-Newton approach), or 2) the forward map $\mathbf{F}$ is linearized to obtained a problem that can be solved by standard methods of singular value decomposition (SVD), and finally 3) the Levenberg-Marquardt approach (LVMR). For our applications we applied all three types to establish the following inversion methods:

1) PORT optimisation tool without regularisation
2) PORT with constant regularisation parameter
3) Gauss-Newton method using SVD and constant regularisation parameter
4) Gauss-Newton method using SVD and variable regularisation parameter
5) LVMR method with constant regularisation parameter
6) LVMR method with variable regularisation parameter.

Depending on the particular minimisation problem a certain method can be chosen adapted to the given situation (*Doicu et al., 2002; 2004*).

The GODFIT package is a comprehensive tool for trace gas retrievals and is developed by our colleagues at BIRA and RTS (*Lerot et al., 2009*) in the framework of the ESA GDP5 project. We apply this package to calculate ozone columns based on GOME/ERS-2 data. GODFIT provides an own inversion routine based on an optimal estimation technique. In the following we refer to this method with the notation ‚BIRA'. From our tools we choose method 3 and use the notation 'GCR'.

Fig. 3-23 shows results of the ozone column retrieval applying BIRA and GCR compared to current operational GDP4 data for a GOME/ERS-2 orbit in December 1999. Both methods processed the same number of pixels in the orbit and led to similar column values as provided by GDP4. The difference between BIRA and GCR is relatively small. However, GCR required about half of the number of

iterations for a ground pixel while it provides qualitatively the same results. This could be an important improvement to save computing time during reprocessing of the complete GOME data set to be performed within the scope of GDP5. A more detailed analysis of the end-to-end performance of the different inversion techniques is in preparation and will be finished by early 2009.
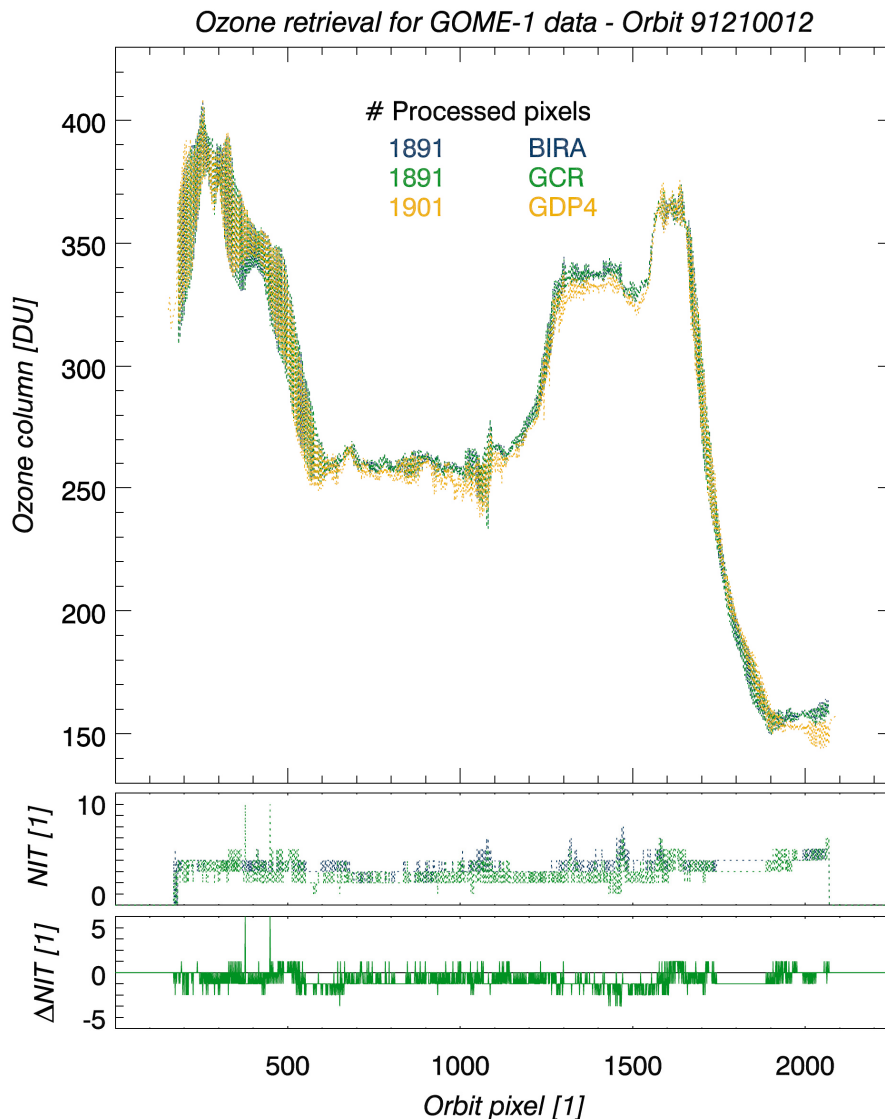
Fig. 3-23: Ozone retrieval based on GOME/ERS-2 data for an orbit on December 10, 1999 applying GODFIT and the inversion methods from BIRA as well as our tool GCR. Retrieved ozone columns in DU as a function of the ground pixel number are given in the top panel. The yellow curve represents the data as provided in the product based on GDP4. The number of iterations for a single pixel required by BIRA and GCR is displayed in the centre panel while the bottom panel illustrates the difference between GCR and BIRA in the number of iterations for a single pixel.

References

Doicu, A., F. Schreier, and M. Hess: Iteratively regularized Gauss-Newton method for atmospheric remote sensing, Comp. Phys. Comm., 148, 214-226, 2002

Doicu, A., F. Schreier, and M. Hess: Iterative regularization methods for atmospheric remote sensing, J. Quant. Spectrosc. Rad. Transf., 83, 47-61, 2004

Lerot, C., M. van Roozendael, J.-C. Lambert, J. Granville, J. van Gent, D. Loyola, and R. Spurr: The GODFIT algorithm: a direct fitting approach to improve the accuracy of total ozone measurements from GOME , Int. J. Rem. Sens., submitted, 2009

3.12 The Discrete Ordinates Matrix Exponential Method for a Pseudo-spherical Atmosphere

A. Doicu, T. Trautmann

The purpose of this work is to present a stable discrete-ordinate algorithm for vertically inhomogeneous layered media using the matrix-exponential solution. Conceptually, the algorithm is similar to a finite-element algorithm and involves the following steps:

- discretization of the atmosphere into a number of distinct but vertically uniform layers,
- derivation of the so-called layer equation using the matrix-exponential solution,
- assemblage of the layer equation into the system matrix of the entire atmosphere,
- solution of the assembled system of equations.

In a further application we extended the matrix-exponential formalism for the scalar radiative transfer to the radiative transfer equation for the full Stokes vector. This leads to a compact and versatile formulation of the vector radiative transfer. Essentially, the linear system of differential equations is treated as a boundary-value problem, and the discretized radiative transfer problem is formulated in terms of the level values of the Stokes vector. In general, the extension of the matrix-exponential formalism to the vector case requires

- an azimuthal expansion of the phase matrix,
- an efficient solution of the matrix eigenproblem, and
- an appropriate treatment of complex eigenvalues.

Method in Brief

We start with the Fourier expansion of the diffuse radiance I_m in a pseudo-spherical atmosphere

$$I(r,\Omega) = I(r,\mu,\varphi) = \sum_{m=0}^{2M-1} I_m(r,\mu)\cos m\varphi$$

Introducing quadrature nodes and weights $\pm\mu_k, w_k, k=1,...,M$ in discrete-ordinate space, the radiative transfer equation for I_m can be formulated as

$$\mu_k^{\pm}\frac{\mathrm{d}I_m}{\mathrm{d}r}(r,\mu_k^{\pm}) = -\sigma_{ext}(r)I_m(r,\mu_k^{\pm}) + \delta_{m0}\sigma_{abs}(r)B(r)$$

$$+(2-\delta_{m0})\frac{F_{sun}}{4\pi}\sigma_{scat}(r)p_m(r,\mu_k^{\pm},\mu_{sun})\mathrm{e}^{-\tau_{ext}^{sun}(|\mathbf{r}-\mathbf{r}_{TOA}|)} \qquad (1)$$

$$+\frac{1}{2}\sum_{l=1}^{M} w_l\sigma_{scat}(r)[p_m(r,\mu_k^{\pm},\mu_l^{+})I_m(r,\mu_l^{+}) + p_m(r,\mu_k^{\pm},\mu_l^{-})I_m(r,\mu_l^{-})],$$

where σ_{ext}, σ_{abs}, σ_{scat} are the extinction, absorption and scattering coefficients, B is the Planck function, F_{sun} is the extraterrestrial solar flux, and the p_m are the Legendre expansion coefficients of the scattering phase function P which is expressed in the form

$$P(r,\Omega,\Omega') = \sum_{m=0}^{2M-1}(2-\delta_{m0})p_m(r,\mu,\mu')\cos[m(\varphi-\varphi')].$$

Note that τ_{ext}^{sun} is the optical depth between a generic point $\mathbf{r}$ and the characteristic point $\mathbf{r}_{TOA}$ at the top of the atmosphere. The other variables above have their usual meaning of radiative transfer theory.

In the next step we define radiance vectors for the upwelling ($\mu>0$) and downwelling ($\mu<0$) radiance Fourier modes via

$$\mathbf{i}_m(r) = \begin{bmatrix} \mathbf{i}_m^+(r) \\ \mathbf{i}_m^-(r) \end{bmatrix}, \quad [\mathbf{i}_m^\pm(r)]_k = \mathrm{I}_m(r, \mu_k^\pm), \quad k = 1, \dots, M$$

such that we directly arrive at a first-order linear differential equation:

$$\frac{d\mathbf{i}_m}{dr}(r) = \mathbf{A}_m(r)\mathbf{i}_m(r) + \mathbf{b}_m(r)$$

Note that the matrix $\mathbf{A}_m(r)$ accounts for both the multiple scattering of diffuse radiation for all possible directions $\pm\mu_k, k=1,\dots M$ as well as the extinction term (i.e. the first term on the right-hand side of Eq. (1)).

Next we introduce a discretization of the atmosphere in N levels: $r_1 = r_{TOA} > r_2 > \dots > r_N = r_s$, where r_s denotes the radial coordinate of the model atmosphere's surface.

A main key in the derivation is that for a homogeneous atmospheric layer we deal with a differential equation with constant coefficients, so that an analytical solution can be derived in the form

$$\mathbf{i}_{m,j} = e^{\overline{\mathbf{A}}_{m,j}\varDelta r_j}\mathbf{i}_{m,j+1} + \int_0^{\varDelta r_j} e^{\overline{\mathbf{A}}_{m,j}(\varDelta r_j - \rho)}\mathbf{b}_m(\rho)d\rho,$$

where $\mathbf{i}_{m,j}, \mathbf{i}_{m,j+1}$ are the radiances at the level boundaries r_j, r_{j+1}, and $\overline{\mathbf{A}}_{m,j}$ is the average of $\mathbf{A}_{m,j}(r)$ over the layer j with geometrical thickness $\varDelta r_j = r_j - r_{j+1}$.

For further mathematical details of the formalism to evaluate the matrix-exponential function we refer the reader to *Doicu and Trautmann (2009a, 2009b)*.

Numerical Simulations
The matrix-exponential solution can be computed by using either the matrix eigenvalue method or the first-order Padé approximation. Here we present some numerical results in order to analyze the applicability of the different versions of the matrix-exponential method. Since the solutions computed with the conventional DISORT method *(Stamnes et al., 1988)* and our matrix eigenvalue method agree to six figures of accuracy, only the matrix-exponential results are reported here.

As an atmospheric scenario we consider two absorbing gases in the UV wavelength region: O_3 and NO_2. In addition, the atmosphere contains a background aerosol in the stratosphere according to the usual LOWTRAN/MODTRAN aerosol parameterization. The aerosol scattering properties are described by the Henyey–Greenstein phase function, while the Rayleigh phase function has been used for the air molecules. The atmosphere is discretized with the following grid steps: 1 km between 0 and 25 km, 2.5 km between 25 and 50 km, and 5 km between 50 and 100 km. The thermal source term is neglected, and all calculations have been performed for a unit solar flux and a surface albedo of 0.3. The results shown in fig. 3-24 correspond to a nadir viewing geometry. In fig. 3-24(a) we plot the radiances computed by the matrix eigenvalue method for different values of the solar zenith angle. The relative errors between the first-order Padé approximation and the matrix eigenvalue solutions are shown in fig. 3-24(b). It is seen that the relative error increases with increasing solar zenith angle, but it never exceeds 0.3%. Other simulation cases are presented for scalar radiative transfer in *Doicu and Trautmann (2009a)*, while applications for the Stokes vector case in an atmosphere containing aerosols and/or clouds is treated in *Doicu and Trautmann (2009b)*.
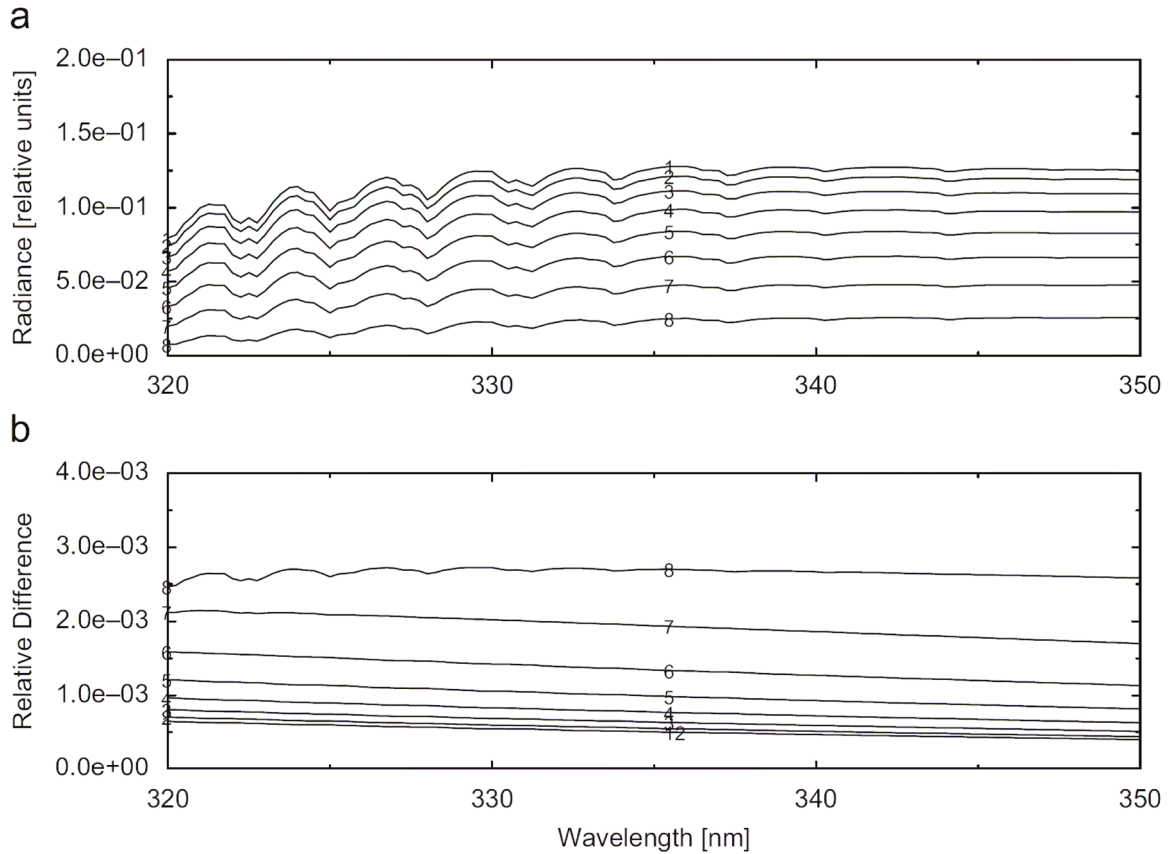
Fig. 3-24: (a) Nadir radiances computed with the matrix eigenvalue method for different values of the solar zenith angle. (b) Relative errors between the first-order Padé approximation and the matrix eigenvalue solutions. The individual curves correspond to solar zenith angles: 1) 10°, 2) 20°, 3) 30°, 4) 40°, 5) 50°, 6) 60°, 7) 70° and 8) 80°.

Conclusions

For the scalar radiative transfer case we conclude that the matrix-exponential formalism retains the main features of the conventional discrete-ordinate method DISORT *(Stamnes et al., 1988)*: it is unconditionally stable for arbitrarily large optical depths. Additionally, the following peculiarities can be put in evidence:

- The matrix-exponential formalism is more compact than the conventional method because the system of equations is formulated directly in terms of the level values of the radiance rather than in terms of the expansion coefficients of the homogeneous solutions.
- For a specific layer, the linear system of differential equation is treated as a boundary-value problem. The matrix-exponential solution incorporates both the homogeneous and the particular solutions, and various polynomial and exponential approximations of the source vector can be considered.
- The matrix-exponential formalism in conjunction with the finite-element technique (derivation and assemblage of layer equations) is a versatile approach. By simply changing the solution method for the matrix-exponential calculation, various representations of the layer equations can be derived. The conventional eigenvalue approach and the finite-difference method can be introduced in a natural way in the framework of the present theory.
- The numerical performance of the matrix-exponential algorithm is approximately a factor of 2–3 faster than the conventional approach.

For vector radiative transfer problems our matrix-exponential formalism possesses the following features:

- By using the matrix-exponential method for a specific layer, the solution of the linear system of differential equations leads to a linear system of equations for the level values of the Stokes vector. This formalism is more compact than the conventional approach, in which the system of equations is formulated in terms of the expansion coefficients of the homogeneous solution.

- The flexibility of the matrix-exponential formalism resides in the concept of the layer equation. Various solution methods for matrix-exponential calculation lead to different representations of the layer equation. In the present analysis we considered only the matrix eigenvalue method and the first-order Padé approximation, but as in the scalar case, higher-order Padé approximations and a general approach, based on the Schur–Parlett method or the scaling and squaring method, can be employed.
- The treatment of the complex eigenvalues of the layer matrix by using fundamental results of the theory of matrix- exponential functions, leads to a natural extension of the formalism for the scalar case to the vector case.

The discussion of the computational examples underlines the efficiency of the proposed method for both an aerosol-loaded atmosphere as well as a cloudy atmosphere. Further applications exploiting the analytical matrix-exponential in the context of coupling forward simulations with inverse problem solvers will be pursued as a next step for the purpose of retrieving atmospheric state vectors.

References

Doicu, A. and T. Trautmann: Discrete-ordinate method with matrix exponential for a pseudo-spherical atmosphere: Scalar case, J. Quant. Spectrosc. Radiat. Transfer, 110, 146–158, 2009a

Doicu, A. and T. Trautmann: Discrete-ordinate method with matrix exponential for a pseudo-spherical atmosphere: Vector case, J. Quant. Spectrosc. Radiat. Transfer, 110, 159–172, 2009b

Stamnes, K., S.C. Tsay, W. Wiscombe, and K. Jayaweera: Numerically stable algorithm for discrete-ordinate-method radiative transfer in multiple scattering and emitting layered media, Appl. Opt., 27, 2502-2509, 1988

3.13 Explicit Expressions for the G-function in Radiative Transfer Theory of Turbid Vegetation Media

S. Otto, T. Trautmann

The approach of a turbid vegetation medium means treating the model leaves to be planar and much smaller than the dimension of a considered region of the vegetation canopy. In addition each point in this region can be represented by a certain number of oriented model leaves. Obviously, this reduces strongly the complexity of the underlying physical process. However it is an often applied simplification in radiative transfer theories with regard to vegetation media. So-called *leaf normal distribution functions* (LNDFs) are defined as a function of space, time and leaf normal direction. The latter is assumed to be confined into the upper hemisphere. A LNDF describes the distribution of the probability of local leaf orientations.

Leaves intercept radiation. As a measure for such extinction processes a mean projection function *G* was introduced in the 1960s (*Nilson, 1971; Ross, 1981*) which depends on the direction of radiation and is the integral of the LNDF, projected onto the radiation direction, over the upper unit sphere. This Ross-Nilson function *G* is the larger, the more the considered radiation direction is confined into the most probable directions of the leaf normals, i.e. the more the radiation direction is perpendicular to the most probable planar leaf elements. Since interactions between radiation and a leaf can be assumed to be the more probable, the more the leaves are oriented perpendicular to the direction of the radiation, *G* is a measure for extinction. Due to these geometrical aspects, *G* is also called 'geometry function' or 'geometry factor', that is shortly, *G-function*. It determines the extinction coefficient and is therefore an integral part of the radiative transfer equation for turbid vegetation media (*Ross, 1981; Marshak and Davis, 2005*). For its analytical solution explicit expressions for the G-functions are required.

To calculate the G-function a LNDF must be pre-defined. However, during the last 40 years since its introduction, *G* could only be calculated analytically and in an explicit form for few simplified cases, e.g. for purely horizontal model leaves. For more realistic LNDFs the G-function was either approximated, associated with a certain inaccuracy for a given LNDF, or is calculated numerically which leads to a certain computational effort.

Beyond the before-mentioned few simplified cases of LNDFs there are more realistic but, nevertheless, standardised LNDFs in literature, for which G was unknown. Firstly, we found the explicit and analytical expressions of *G* for these standard leaf orientation functions and, secondly, we defined a more general trigonometric LNDF for which we also calculated *G*. The free parameters of the latter LNDF can be fitted to measurements, so that realistic vegetation canopies can be characterised for which then the G-function is also given. With regard to the analytical solutions of the radiative transfer equation, thirdly, this opens up the possibility to develop hierarchies, e.g. based on the two- and four-stream approximation, of fast radiative transfer solvers considering realistic leaf architectures. For more details we refer the reader to our original paper (*Otto and Trautmann, 2008*).

References

Marshak, A. and A. Davis: 3D radiative transfer in cloudy atmospheres, Berlin, Heidelberg: Springer, 686 p., 2005

Nilson, T.: A theoretical analysis of the frequency of gaps in plant stands, Agric. Meteor., 8, 25-38, 1971

Otto, S. and T. Trautmann: A note on G-functions within the scope of radiative transfer in turbid vegetation media, J. Quant. Spectrosc. Radiat. Transfer, 109, 2813-2819, 2008

Ross, J.: The radiation regime and architecture of plant stands, The Hague: Dr. W. Junk Publisher, 391 p., 1981

3.14 Confusion about Voigt

Franz Schreier

Due to its importance for molecular infrared spectroscopy, the Voigt profile *(Armstrong, 1967)* is discussed in many textbooks on atmospheric radiation. Describing the combined effect of pressure (collisional) broadening corresponding to a Lorentzian profile $g_L(v)$ with half width $\gamma_L(v)$ and Doppler broadening corresponding to a Gaussian $g_G(v)$ with half width $\gamma_G(v)$, the Voigt profile is defined by the convolution integral, i.e.,

$$g_V(v) = g_L(v) \otimes g_G(v) \qquad (1a)$$

$$K(x,y) = \frac{y}{\pi} \int_{-\infty}^{\infty} \frac{\exp^{-t^2}}{(x-t)^2 + y^2} \, dt \qquad (1b)$$

where $K(x,y)$ is the Voigt function and the dimensionless variables x,y are defined in terms of the distance from the line center position and the Lorentzian and Gaussian half–widths,

$$x = \sqrt{\ln 2} \, \frac{v - v_0}{\gamma_G} \quad y = \sqrt{\ln 2} \, \frac{\gamma_L}{\gamma_G} \qquad (2)$$

Apparently the Voigt profile is a combination of Lorentz and Gauss, and this view is illustrated in numerous textbooks by plots similar to fig. 3-25(a). However, *Huang and Yung (2004)* argue that these figures are often misleading; in particular '….. *the impression that, for Lorentz and Doppler profiles with the same half-widths, the corresponding Voigt profile is steeper than the Lorentz profile and flatter than the Doppler profile in the line core ….. is found to be incorrect …..*'. Furthermore, '….. *the peak of the normalized Voigt profile should be lower than the peak of the normalized Lorentz profile …..*', and '….. $g_V(v)$ *should be larger than* $g_L(v)$ *when* v *is at the line wings …..*'. This behavior is shown in fig. 3-25(b).
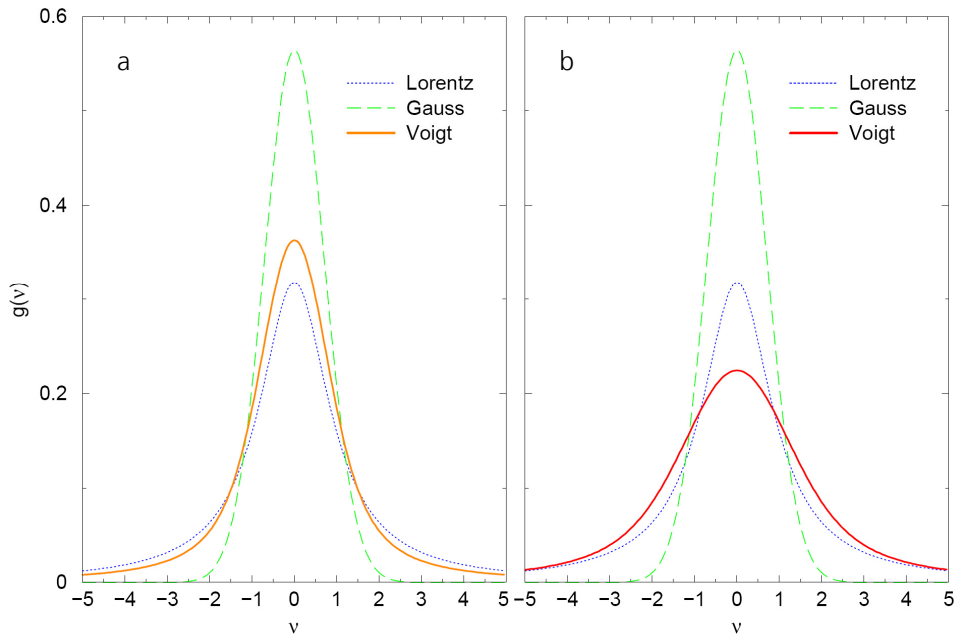
Fig. 3-25: Comparison of Voigt profile with Lorentz and Gauss profiles as shown in some textbooks: a) Thomas and Stamnes (1999), Lopez-Puertas and Taylor (2001), Zdunkowski et al. (2007) / b) Liou (1992)

A closer inspection shows that both figures are somehow 'correct' or – in other words – none of the figures is wrong. The confusion is due to the imprecise usage of the half-width parameters γ and the ambiguous term 'corresponding'.

Eq. 1b clearly shows that the shape of the Voigt function K is essentially determined by the ratio of the widths; however, because of the horizontal and vertical scaling the shape of the Voigt profile g_V is determined by both γ_L and γ_G. As a consequence, the notion of a 'corresponding' Voigt profile is ambiguous even for $y = 1$. Fig. 3-26(b) clearly demonstrates that for a given width ratio y several Voigt profiles exist.

According to the (approximate) formula for the width of the Voigt profile

$$\gamma_V = \frac{1}{2}\left(\gamma_L + \sqrt{\gamma_L^2 + 4\gamma_G^2}\right)$$

the Voigt profile arising from the convolution of a Lorentzian and Gaussian with equal widths is indeed wider, i.e., $\gamma_V > \gamma_L, \gamma_G$. However, the 'corresponding' Voigt profile might just as well be defined by $\gamma_V = 1$ (in fact a figure caption saying '….. *The Lorentz, Doppler, and Voigt profiles with the same half-width …..*' could easily be interpreted as g_L for $\gamma_L = 1$, g_G for $\gamma_G = 1$, and g_V for $\gamma_V = 1$). For $\gamma_L = \gamma_G$ or $y = (\ln 2)^{1/2}$ this corresponds to $\gamma_L = 2/(1+5)^{1/2} = 0.6180$. A comparison of these profiles shown in Fig. 3-26(a) also indicates that – contrary to Huang and Yung's expectations – in the line wings the Voigt profile can be intermediate between those of the Lorentz and Doppler profiles.
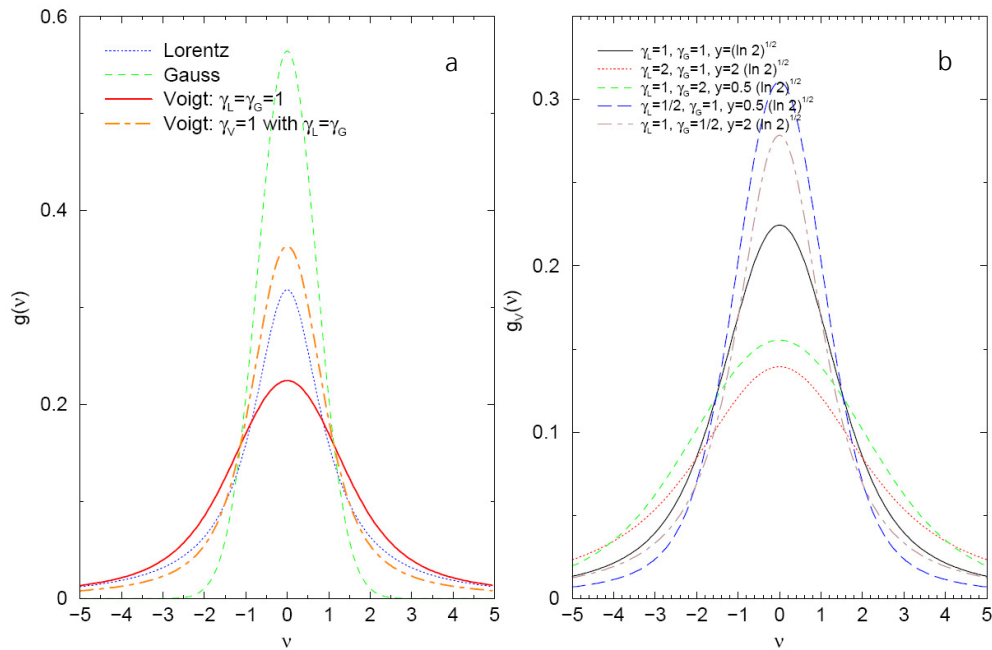
Fig. 3-26: Relation between Voigt profiles and width ratios

References

Armstrong, B.: Spectrum line profiles: The Voigt function, J. Quant. Spectrosc. & Radiat. Transfer, 7, 61-88, doi:10.1016/0022-4073(67)90057-X, 1967

Huang, X. and Y. L. Yung: A common misunderstanding about the Voigt line profile, J. Atmos. Sci., 61 (13), 1630-1632, doi:10.1175/1520-0469(2004)061, 2004

Liou, K.-N.: Radiation and Cloud Processes in the Atmosphere, Oxford University Press, 1992

Lopez-Puertas, M. and F. Taylor: Non–LTE Radiative Transfer in the Atmosphere, World Scientific Publishing, 2001

Salby, M. L.: Fundamentals of Atmospheric Physics, Academic Press, 1996

Thomas, G. and K. Stamnes: Radiative Transfer in the Atmosphere and Ocean, Cambridge University Press, 1999

Zdunkowski, W., T. Trautmann, and A. Bott: Radiation in the Atmosphere – A Course in Theoretical Meteorology, Cambridge University Press, 2007

3.15 Development and Application of Inversion Tools on IASI Spectra

M. Szopa, A. Doicu, F. Schreier

The IASI instrument on Metop-A provides high quality data of the atmosphere's infrared spectrum in the range of 645-2762 cm^{-1} (3.62 μm to 15.5 μm). IMF-AP has started developing tools for analyzing and inverting these spectra in order to extract information about the distribution profiles of temperature and various gases with the option for evaluating further IASI capabilities for such as, e.g. the detection of forest fires.

Level 1 and 2 data of IASI is freely available at EUMETSAT's UMARF database. We have created tools for reading this data – as far as they were not existent beforehand – and compared the spectra as measured by IASI to simulated spectra calculated by the Generic Atmospheric Radiation Line-by-line Infrared Code (GARLIC). As obvious in fig. 3-27, simulation and measurement are in reasonably good agreement. Our intention is to improve this even further by matching GARLIC's input more closely with the conditions as measured by IASI at the given time and location. Besides of demonstrating the usefulness of GARLIC itself these activities are also aiming at laying the ground for GARLIC to become the forward line-by-line model of IMF-APs inversion algorithms.
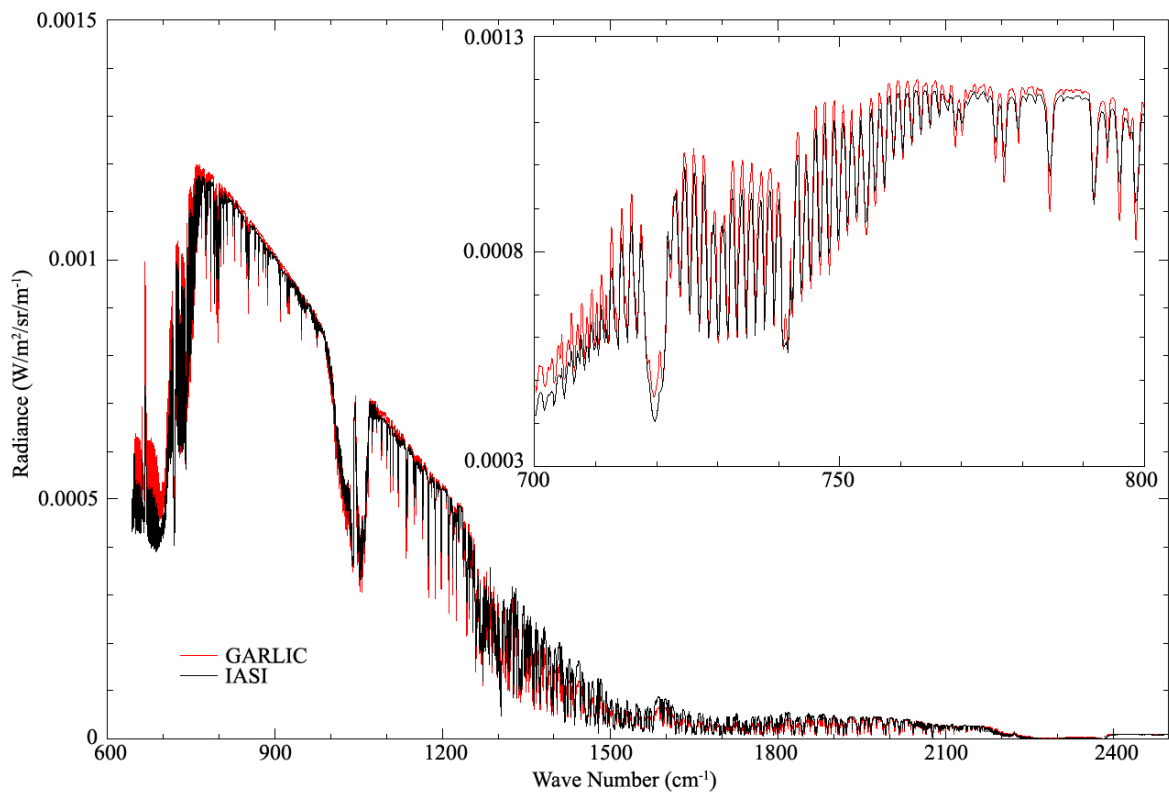
Fig. 3-27: Comparison of an IASI spectrum with the simulation by GARLIC

The next step was the extension of the capabilities of the inversion tool aDvanced Retrieval of the Atmosphere with Constrained and Unconstrained Least-Squares Algorithms (DRACULA) by adding a new method for solving ill-posed differential equations, namely a second level Runge-Kutta method (as presented by *Böckmann et al, 2008*). When linearizing the problem

$$F(x) = y$$

with *F* being a non-linear operator representing the forward model, *y* the vector containing the measurement data and *x* the *n*-dimensional vector containing the actual conditions about the exact solution *x*, one arrives at the differential equation

$$K_k\left(x_{k+1}^{\delta} - x_k^{\delta}\right) = y^{\delta} - F\left(x_k^{\delta}\right)$$

where x_k^{δ} denotes the kth iteration step towards finding the regularization approximation x^{δ} of x, K_k the Jacobian of $F\left(x_k^{\delta}\right)$, and y^{δ} is the 'noisy' measurement. For solving this differential problem, the second level Runge-Kutta family of methods yields the iteration

$$x_{k+1}^{\delta} = x_k^{\delta} + b\widetilde{A}^{-1}\left(\alpha_k I_{2n} + B\right)^{-1}\widetilde{A}s_k$$

with
$b = \left(b_1 I_n, b_2 I_n\right)$, where parameters b defining the method

$I_n = n$-dimensional identity matrix

$s_k = \left(K_k^T\left(y^{\delta} - F\left(x_k^{\delta}\right)\right), K_k^T\left(y^{\delta} - F\left(x_k^{\delta}\right)\right)\right)^T$

and

$\widetilde{A} = \begin{bmatrix} a_{11}I_n & a_{12}I_n \\ a_{21}I_n & a_{22}I_n \end{bmatrix}$, $B = \begin{bmatrix} a_{11}K_k^T K_k & a_{12}K_k^T K_k \\ a_{21}K_k^T K_k & a_{22}K_k^T K_k \end{bmatrix}$, with parameters a defining the method, and α_k being

the inverse step length, depending on the regularization parameter.

We have added this iteration method to DRACULA and started to test it with simulated data, comparing it with the Tikhonov-method with *a priori* regularization parameter. So far, the Runge-Kutta method seems to yield results of similar precision as the Tikhonov-method while being less dependent on variations of the regularization parameter, but further tests are required before final conclusions can be drawn. Once this is achieved, an interface between GARLIC and DRACULA has to be established permitting to apply this new approach on IASI data.

References

Böckmann, C. and P. Pornsawad: Iterative Runge-Kutta-type methods for nonlinear ill-posed problems, Inverse Problems, 24, 025002, 2008

3.16 Textbook on *Electromagnetic Wave Scattering on Non-spherical Particles*

T. Rother

The textbook *Electromagnetic Wave Scattering on Non-spherical Particles: Basic Methodology and Simulations* was finished in 2008 and is accepted for publication in 2009 by *Springer* in the *Optics* series. The readership addressed comprises graduate students as well as researchers working in the field of electromagnetic and light scattering analysis.

If we speak about scattering in this book it is tacitly meant that we consider the interaction of a plane electromagnetic wave with a three-dimensional structure. The latter is characterized by its dielectric property, and the geometry of its boundary surface. A corresponding scattering theory interrelates the asymptotic free states before and after the interaction of the primary incoming plane wave with the scattering structure, whereas the incoming plane wave represents the asymptotic free state before the interaction. If we know the asymptotic free state after the interaction we can derive and define quantities which are appropriate to measure. Moreover, we restrict our considerations to the steady state of scattering. The asymptotic free states correspond in this case to spatial distances large compared to a characteristic distance of the scattering structure, i.e. we look at the free states in the far-field. Due to this understanding of scattering we have to consider processes taking place at different spatial scales. These are the interaction between the incoming plane wave and the scatterer on the local scale of the scatterer, and the behaviour of the electromagnetic fields in the non-local far-field. An exception is only made in chapter 6 when we examine the near-field of a two-dimensional, ideal metallic grating.

Scattering of electromagnetic waves on three-dimensional structures requires the solution of boundary value problems related to the vector-wave equation, in general. Only in specific situations, as it happens for spherical scatterers or if we consider infinitely extended cylinders with noncircular cross-sections normally illuminated by a plane wave, we can benefit from the solution of two independent but scalar boundary value problems related to the scalar Helmholtz equation. The detailed considerations of the boundary value problems related to the scalar Helmholtz equation carried out in this book are therefore attributed primarily to the didactical aspect that most of the derivations become even simpler. The dyadic nature of the relevant Green functions resulting in an increased complexity can be neglected in this case. However there are also essential differences between the scalar and dyadic formulation. One of such differences is the singular behaviour of the free-space Green's function in the source region with corresponding consequences for the general solution methods and their numerical realizations. But, on the other hand, there are other physical disciplines where the scalar boundary value problems considered herein are of direct importance. This applies to acoustic wave scattering and to certain problems in quantum and fluid mechanics, to mention only a few examples. The parameter 'k' occurring in the Helmholtz equation has merely a different physical meaning in these cases.

Fig. 3-28: The 22° halo formed by scattering of light on hexagonal ice crystals

The chapters of this book are organized as listed below:

In the **first chapter** we formulate the boundary value problems of our interest, followed by a very formal discussion of a solution scheme which was already established by Rayleigh.

It is the general intention of all our efforts to approximate the unknown solution of the boundary value problems in terms of an appropriate finite series expansion. The mathematical tools which are required for this purpose are examined in **chapter two**. Here we also define the term 'appropriate' more precisely.

Chapter three represents a first step towards the relevant Green functions. Once we have found the finite series expansion for the sought solution we are able to derive the equivalent approximation of the Green function belonging to the considered boundary value problem. This is accomplished by employing Green's theorem appropriately. However, the most important result of this chapter, from the author's point of view, is the verification of the fact that Waterman's T-matrix is a substantial part of this Green function.

This result is derived again but on a different way in **chapter four**. Starting point is the definition of the so-called 'interaction operator'. This definition can be considered as a special formulation of the Huygens principle for Green functions. Chapter four deals exclusively with the Green functions related to the boundary value problems of our interest, without any recourse to the underlying physical problem. Thus we called the resulting formalism the 'self-consistent Green's function formalism'. With that chapter the author expresses his firm conviction that, from a methodical point of view, the Green functions form a suitable starting point for the treatment of different scattering problems as well as for the development of numerical procedures. The advantage of using Green functions is moreover demonstrated by deriving those important mathematical properties like symmetry and unitarity. These properties will be related later on to the physical experience of reciprocity and energy conservation.

Chapter five illustrates how one can find other known solution methods in the self-consistent Green's function formalism described above. Amongst others we discuss the advantages and disadvantages of a special Finite-Difference technique, the so-called 'Method of Lines'. There exist several misunderstandings concerning the nature of this method as well as its assumed difference compared to the T-matrix methods. These misunderstandings are clarified. In order to reveal the relation of the Green's function formalism to the conventional surface and volume integral equation methods as well as to derive the so-called 'Lippmann-Schwinger equations' we have to perform a slight but important change in the definition of the interaction operators introduced in chapter four.

This change in the definition of the interaction operator is strongly related to the controversial and still ongoing discussion of 'Rayleigh's hypothesis'. The history of Rayleigh's hypothesis is so interesting that we found it appropriate to outline it in a separate chapter - **chapter six**. Although we are also unable to provide a final and satisfactory answer to this problem we believe that the Green functions point of view may add some interesting aspects to it. Additionally, we present a numerical answer to that problem originally considered in Rayleigh's famous paper of 1907.

In **chapter seven** we take a closer look onto the electromagnetic theory as needed to formulate the scattering process and to define suitable quantities in the far-field helping to establish the link to real measurements. Particularly the nature of the far-field and the somehow strange nature of a plane wave are considered in detail here. Therefore this chapter forms the physical basis for the numerical simulations in the next chapter.

With **chapter eight** we condense the theoretical considerations of the former chapters into numerical simulations of selected scattering scenarios which are of importance for recent measurement techniques. Our main focus here is on the difference of the scattering behaviour of non-spherical but rotationally symmetric particles in fixed and random orientation versus spherical particles.

The textbook is finally completed with a commented **reference chapter**.

3.17 Green Function for Multiple Scattering of Scalar Waves on an Ensemble of Non-penetrable Particles

K. Schmidt

In the IMF-AP annual report of 2007 we summarized our theoretical investigations concerning the multiple scattering of waves on ensembles of particles. In the approach presented we extended the self-consistent Green function formalism for acoustic and light scattering on single particles, developed by Rother (2005(a) , 2005(b), 2006, 2007), to N obstacles. We considered the case in which acoustic waves impinge on N sound-soft objects defined by fulfilling the homogeneous Dirichlet condition on their boundary surfaces. It could be shown that the N-particle Green function $G(x,x')$ is given by

$$G(x,x') = G_0(x,x') + \sum_{i=1}^{N} \oint_{\partial \Gamma_i} G_0^>(x,\bar{x}) W_i(\bar{x},x'') G_0(x'',x') dS(\bar{x}) dS(x'')$$

Here, $G_0(x,x')$ and $G_0^>(x,x')$ are the free space Green's function and that one for $|x|>|x'|$. $W_i(\bar{x},x'')$ denotes the interaction operator of the *i*th particle (*i* = 1…..N). Its matrix elements are determined by the following equation system which results from the boundary conditions at all particle surfaces.

$$\ddot{W}_i = \ddot{T}_i^t + \ddot{T}_i^t \cdot \sum_{j=1, j\neq i}^{N} \ddot{S}_1^t (a_i - a_j) \cdot \ddot{W}_j \cdot \ddot{S}_2^* (a_i - a_j)$$

$\ddot{T}_i^t$ designates the transpose of Waterman's T-matrix $\ddot{T}_i$ of the *i*th isolated particle *(Waterman, 1969)*. The T-matrices are computed in advance with respect to arbitrarily chosen local coordinate systems within the particles. The matrices $\ddot{S}_1$ and $\ddot{S}_2$ are transformation matrices of the normalized outgoing and incoming spherical wave functions from one coordinate system into another (see e.g. *Martin, 2006*). Their arguments a_i, a_j are vectors pointing from the origin of a global coordinate system outside the particles at the origins of the local coordinate systems within the *i*th and *j*th particle, respectively. Above equation system takes the correlation between all objects into account, thus revealing the many-particle character of the interaction operators W_i.

Recently we elaborated on important properties such as the unitarity, symmetry, and reciprocity as well as the validity of the optical theorem. Thus matrix elements of a total interaction operator W characterizing the whole ensemble were introduced as follows.

$$[\ddot{W}]_{n'm'} := \sum_{n=0}^{\infty} \sum_{m=0}^{\infty} \sum_{j=1}^{N} [\ddot{S}_2]_{nn'}(-a_j) \cdot [\ddot{W}_j]_{nm} \cdot [\ddot{S}_2]_{m'm}(a_j)$$

Due to this definition, the N-particle Green function $G(x,x')$, expressed in terms of above matrix elements, appears as in the single-particle case *(Rother, 2005(a), 2005(b), 2006, 2007)*. Accordingly, the symmetry

$$[\ddot{S}]_{pq\nu\mu} = (-1)^{q+\mu} \cdot [\ddot{S}]_{\nu,-\mu,p,-q}$$

and unitarity

$$\ddot{S} \cdot \ddot{S}^{t*} = \ddot{E}$$

of the scattering matrix

$$\ddot{S} := \ddot{E} + 2\ddot{W} ,$$

with $\vec{E}$ being the unit matrix, follow simply from the one-particle case. Furthermore, a N-particle scattering amplitude A was introduced which is also a function of all interaction operators W_i, $i = 1…N$. Therefore the ensemble appears as one obstacle for an observer in the far field. Thus the known reciprocity

$$A(\hat{n}_{sca},\hat{n}_{inc}) = A(-\hat{n}_{inc},-\hat{n}_{sca})$$

of the scattering amplitude and the validity of the optical theorem can be assumed for N scatterers, too.

References

Martin, P. A.: Multiple Scattering – Interaction of Time-Harmonic Waves with N Obstacles, Cambridge University Press, Cambridge, 2006

Rother, T.: Self-consistent Green's function formalism for acoustic and light scattering, Part 1: Scalar notation, Opt. Commun., 251, 254-269, 2005(a)

Rother, T.: Self consistent Green's function formalism for acoustic and light scattering, Part 2: Dyadic notation, Opt. Commun., 251, 270-285, 2005(b)

Rother, T.: Self-consistent Green's function formalism for acoustic and light scattering, Part 3: Unitarity and Symmetry, Opt. Commun., 266, 380-389, 2006

Rother, T.: Scalar Green's function for penetrable or dielectric scatterers, Opt. Commun., 274, 15-22, 2007

Waterman, P.C.: New formulation of acoustic scattering, J. Acoust. Soc. Am. 45, 1417-1429, 1969

3.18 Scattering Database for Spheroidal Particles

J. Wauer (Univ. Leipzig)

Scattering of electromagnetic waves on nonspherical dielectric particles receives growing importance in remote sensing of the Earth's atmosphere as well as in technical diagnostics. Examples include e.g. the impact of dust like particles on our climate system and analyzing powder probes. An increasing number of modern measurement techniques requires to take electromagnetic wave scattering on nonspherical particles into account. However this is not a trivial task. Two aspects have to be considered:

- The numerical effort is much higher than that known for spherical particles using classical Mie theory. It strongly depends on the morphology of the particle and can be performed on-line only in very specific situations.
- The convergence procedures of the existing approaches are much more complex as compared to spheres. Obtaining reliable results requires the detailed knowledge of the methodology behind each approach.

While in last year's annual report we described the principles of the scattering database, this year we expand on its main features together with giving information on its user interface. All database calculations have been performed using the program *mieschka* described in detail in *Wauer et al. (2004)*.

Physical Structure
Currently, the database contains scattering quantities for randomly oriented spheroidal scatterers. The database is restricted to a size parameter of $kr_{eff} = 40$ (r_{eff} is the radius of the volume equivalent sphere). For the aspect ratio ($av = a/b$, where a and b are semi axes parallel and perpendicular to the axis of rotation) and the refractive index (Re(n), Im(n)) the following grid was used in the first version of the database:

n	Re(n)	1.33	1.40	1.50	1.60	1.70	1.80	
	Im(n)	0.000	0.001	0.005	0.010	0.030	0.050	0.100
av		0.67	0.77	0.87	1.00	1.15	1.30	1.50

Table 3-2: Original 3D-grid used in the calculations for the optical scattering database

Additionally, the resolution of the data base was improved in the last year. Therefore we added the following refractive indices and aspect ratios to the grid:

| Re(n)	1.31	1.55				
av	0.714	0.82	0.93	1.075	1.22	1.40

Table 3-3: Expansion of the 3D-grid
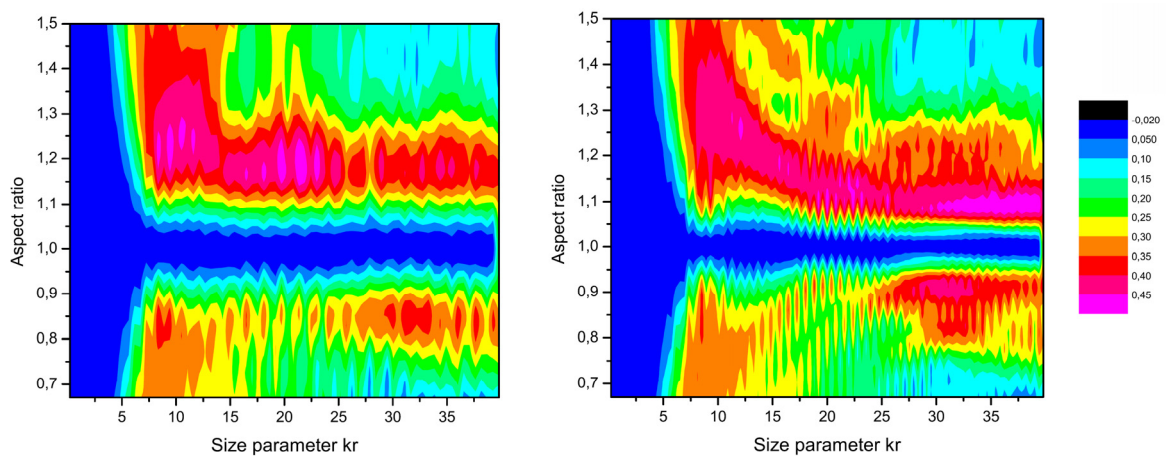
Fig. 3-29: Backscattering depolarization as a function of the size parameter and aspect ratio for a refractive index of n=1.33. In the left panel the aspect ratio was used at the nodes *av* = 0.67, 0.77, 0.87, 1, 1.15, 1.3 and 1.5 and in the right panel additionally the nodes *av* = 0.714, 0.82, 0.93, 1.075, 1.22 and 1.4 have been taken.

Database User Interface and Access

All data sets are arranged with respect to their refractive indices and aspect ratios in a file system. To get easy access to the data, we have developed a user interface providing additional functionalities going beyond the simple readout of data. These are consistency tests of the user requests, interpolation between data and the computation of size averaged scattering quantities. The user interface supports three operation modes:

- **Generation of a single data set:** In this mode the user can search for one specific data set of a randomly oriented spheroidal particle characterized by the radius r_{eff}, the aspect ratio *av*, the real and the imaginary part of the complex refractive index n.
- **Generating a range of data:** Scattering quantities for a certain parameter range are generated. The quantities are stored in respective files as a function of the radius r_{eff}, a function of the radius r_{eff} and the aspect ratio *av*, or as a function of the radius r_{eff} and the real part of the refractive index n. Alternatively r_{eff} can be replaced by the size parameter kr_{eff}.
- **Generating an averaged data set:** In this mode size and aspect ratio averaged scattering quantities are calculated. It includes factorizing the distribution function in a size distribution and an aspect ratio distribution. The following size distribution functions are predefined in the user interface *(Mishchenko et al. 2002)*.
  - modified gamma distribution
  - monomodal log-norm distribution
  - modified power law distribution.

On request, a restricted version (parameter range of the first table) of the database including the documentation are available, free of charge, on a CD-ROM (email to Jochen.Wauer@dlr.de for request).

References

Wauer, J., K. Schmidt, T. Rother, T. Ernst, and M. Hess: Two software tools for plane-wave scattering on nonspherical particles in the German Aerospace Center's virtuallaboratory, Applied Optics, 43, 6371-6379, 2004

Mishchenko, M.I., L.D. Travis, and A.A. Lacis: Scattering, Absorption, and Emission of Light by Small Particles, Cambridge University Press, 2002

3.19   First Results from SAMUM 2

C. Köhler, E. Lindermeir (IMF-EV), T. Trautmann

SAMUM 2 (Saharan Mineral Dust Experiment) is the continuation of the SAMUM project funded by the German Research foundation. Its aim is to characterize the optical and microphysical properties of mineral dust. While SAMUM took place very close to the Sahara, Earth's largest desert, and thus collected valuable information about airborne dust close to its source region, the focus of SAMUM 2 lies on aged mineral dust aerosols. These particles have been transported by atmospheric currents for several days and thus change their physical properties due to hygroscopic growth or mixture with other atmospheric aerosols. Among those other aerosols so-called biomass burning aerosols (or simply smoke) are of special interest. They are emitted in large amounts due to the burning of agricultural waste, a process regularly observed in central Africa during the first months of the year. The smoke particles are about one order of magnitude smaller in diameter than the mineral dust particles and consist mainly of light absorbing carbon. In contrast to these highly absorbing biomass aerosols, the majority of the mineral dust is not absorbing but dominantly scatters incoming radiation. Thus a combination of both aerosol types might display physical properties that differ strongly from the behaviour of its individual components. However it is extremely difficult to predict the physical properties of the mixture for two main reasons: Firstly solving the governing physical equations describing optical processes – the Maxwell equations – is very complex, particularly on the surface of irregularly shaped particles, as observed with aerosols. Secondly, our understanding of the microphysical processes involved in particle growth, particle agglomeration or particle mixing is relatively poor. Considering, for example, a binary mixture of smoke and dust, it is easy to imagine that a layered structure containing pure biomass and pure dust layers differs strongly from a homogeneous mixture of both aerosols, regarding the respective interaction with radiation.

The most suitable way to address the problems encountered in the modelling of aerosol radiative properties are sophisticated field campaigns, which collect as much information as possible about the aerosols and thus help to develop a consistent model of the most dominant physical processes. This was the goal of the SAMUM 2 field experiment, which was conducted during January and February 2008 on the Island of Santiago, Cape Verde (fig. 3-30 and 3-31).

The instrumentation included air-borne and ground based LIDAR to investigate the vertical structure of the aerosol layers, several sophisticated instruments to measure the aerosol mineral composition and size-distributions and spectrometers to gather information about the radiative effect of mixed smoke-dust layers. IMF's participation was a joint approach by combining the expertise in infrared spectroscopy of IMF-EV (Experimental Methods) and our experience in radiative transport theory (see annual report 2007). During the course of the campaign a Fourier Transform Infrared Spectrometer (FTIR) was installed at Praia airport from January 21st to February 6th and measured the downwelling infrared radiation. The information gained during our measurements will help to better characterize the radiative forcing exerted by mineral dust and biomass burning aerosols in the thermal infrared and thus support the development of reliable climate models for the earth. Furthermore our measurements could lead to improved retrieval algorithms for satellite and ground based instrumentation measuring aerosol optical properties.

Fig. 3-30: The SAMUM 2 experimenter group in front of the DLR Falcon research aircraft

Fig. 3-31: The IMF spectrometer setup (left) and the aerosol measurement equipment of the Institute for Tropospheric research and the University of Darmstadt (right) during a visit from a Cape Verdian television team.
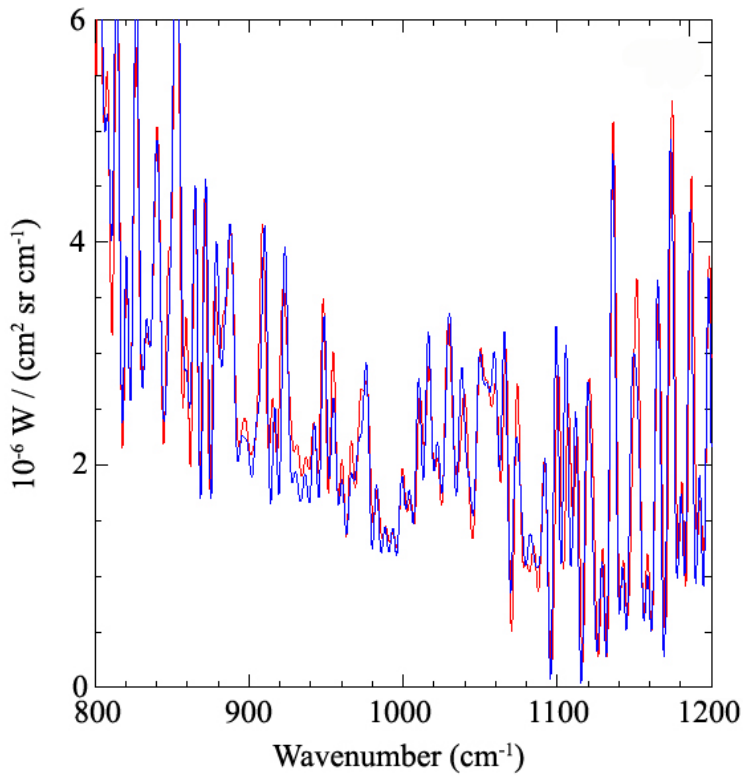
Fig. 3-32: A comparison between a measurement (blue) and a TRAVIS simulation (red) of the downwelling radiance for a clear sky case, i.e. without dust.
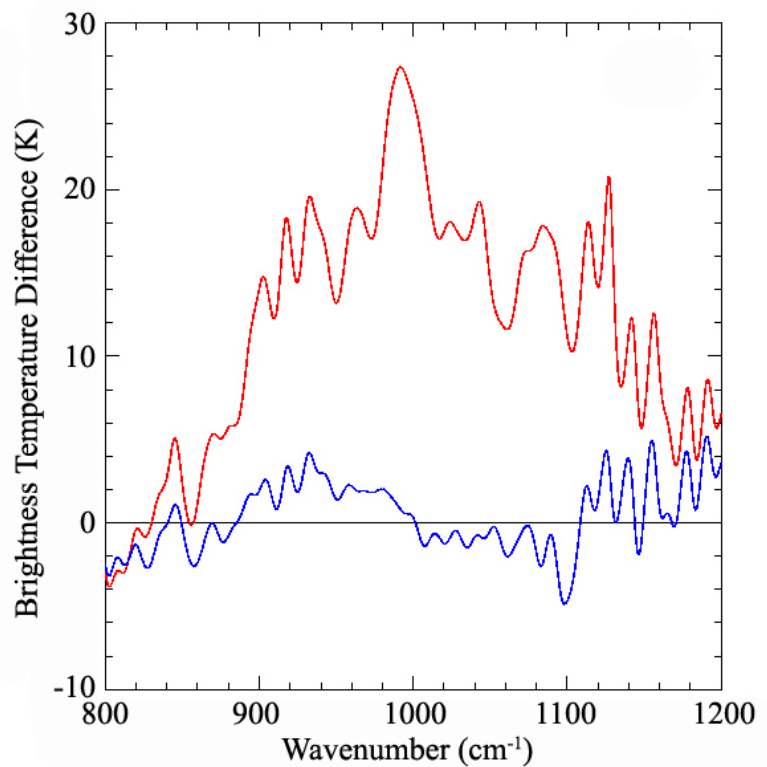
Fig. 3-33: Brightness temperature difference obtained after subtracting the simulated gas emission from the measured spectra for a clear sky case (blue) and for a dust loaded atmosphere (red).

The first quicklooks of all instruments indicate that SAMUM 2 was very successful. No significant instrument failures among the whole consortium occurred and all anticipated meteorological conditions were observed during the measurement period leading to a comprehensive dataset. A first glance at our measurements can be obtained from fig. 3-32, which shows a comparison of a measured spectrum with a radiative transfer simulation for a clear sky day in the infrared atmospheric window region from 8 to 12 microns. The radiative transfer simulation was produced using the TRAVIS code *(Otto et al., 2009)* with a radio sonde profile and GOME-2 ozone column density as input. The agreement between both spectra is the basis for further analyses of measurements of a dust loaded atmosphere because isolation

of the radiative effect of the mineral dust always requires the removal of the numerous gas absorption lines observed in the thermal infrared. The resulting spectra are shown in fig. 3-33. It was obtained by plotting the residual brightness temperature obtained after subtraction of the simulated gas absorption from the measured downwelling radiation for a clear sky case (blue) and a dust case (red). While the blue curve's deviation from zero can be viewed as an error measure, the red curve allows a first impression of the radiative effect of the dust aerosol. It is important to notice, that the effect of the dust clearly exceeds the error estimate.

As described earlier (see annual report 2007) the FTIR we used, a D&P Model 102, is originally not designed for atmospheric measurements and thus calibration was and still remains an important issue, especially at low radiance levels. We cooperate with a group of the UK Metoffice, possessing a wealth of know-how in atmospheric FTIR measurements. They kindly allowed us to conduct measurements with a high precision low temperature black body at the UK Metoffice site in Exeter. These measurements helped us to gain advanced insight into the performance of our FTIR in atmospheric measurements and may lead to even better data evaluation and calibration algorithms. Additionally we performed an inter-instrument comparison of the commercial D&P Model 102 with MIROR (Michelson Interferometer with Rotating Retroreflector), an FTIR developed by IMF-EV. The corresponding data are just under investigation.

The comprehensive datasets successfully collected in 2008, are a sound basis for further scientific research. Next steps include the evaluation of the measured spectra and the incorporation of the data produced by our SAMUM 2 partners into our model simulations. Then the comparison between our aerosol and gas absorption models with accurate measurements, which in turn should yield useful results, are required for further improved, reliable and well characterized models and simulation algorithms.

References

Otto, S., E. Bierwirth, B. Weinzierl, K. Kandler, M. Esselborn, M. Tesche, A. Schladitz, M. Wendisch and T. Trautmann: Solar radiative effects of a Saharan dust plume observed during SAMUM assuming spheroidal model particles, Tellus, 61B, DOI: 10.1111/j.1600-0889.2008.00389.x, 2009

3.20 Radiative Transfer Modelling of a Mineral Dust Plume – Contribution to SAMUM

S. Otto, T. Trautmann

The Saharan Mineral Dust Experiment (SAMUM) was performed in May/June 2006 in order to investigate the microphysics of mineral dust from the Sahara, i.e. to explore the dust close to its source. The project was initiated since mineral dust is one of the most important aerosols of the Earth's atmosphere and because its radiative effects are still in discussion. Our investigations focused on the dust's absorbing and scattering properties with measured microphysical properties of dust particles as starting point (*Sokolik et al., 2001*). The following quantities, being most important for our work, were measured during SAMUM:

- dust size distributions and number concentration profiles
- environmental conditions (temperature, pressure, humidity)
- size-resolved chemical composition
- mean aspect ratios of ellipses which were fitted to the single particle observations using a scanning electron microscope (SEM)
- backscatter coefficient (BSC) and lidar ratio (LR) at 532 nm measured by various lidars
- upwelling and downwelling spectral irradiances at ground and on aircraft as well as spectral surface albedo.

The size distributions demonstrated that the dust contained a dominant fraction of coarse particles: 80 % of the total geometrical cross-section arised from particles larger than about 1 µm in diameter. This particle mode has large effects on the optical properties and radiative transfer (*Otto et al., 2007*).

The size-resolved chemical composition was derived with respect to the five most frequent component classes: silicate, quartz, carbonate, sulphate and iron-rich material. The mean spectral complex refractive indices of these constituents (see e.g. annual report 2007) were used to calculate a mean size-resolved spectral complex refractive index of the entire dust ensemble with the help of the chemical composition data. It turned out that at a wavelength of $\lambda = 550$ nm the real and imaginary part amounted to about 1.51 and 0.0008 for sub-micron (fine-mode) as well as 1.55 and 0.006 for micron (coarse-mode) particles. The lower value of the imaginary part – which is a measure for absorption – for fine-mode particles, which also exhibit smaller geometrical cross-sections, indicates that this type of particles cause less absorption. Thus, the coarse-mode particles dominate the optical properties in the solar spectral range just because of their size and the relatively large imaginary part. This resulted in a single scattering albedo (SSA) and asymmetry parameter (AP) of about 0.8 at 550 nm and indicates that mineral dust of the Sahara is more absorbing and forward scattering than currently assumed (*Dubovik et al., 2002*).
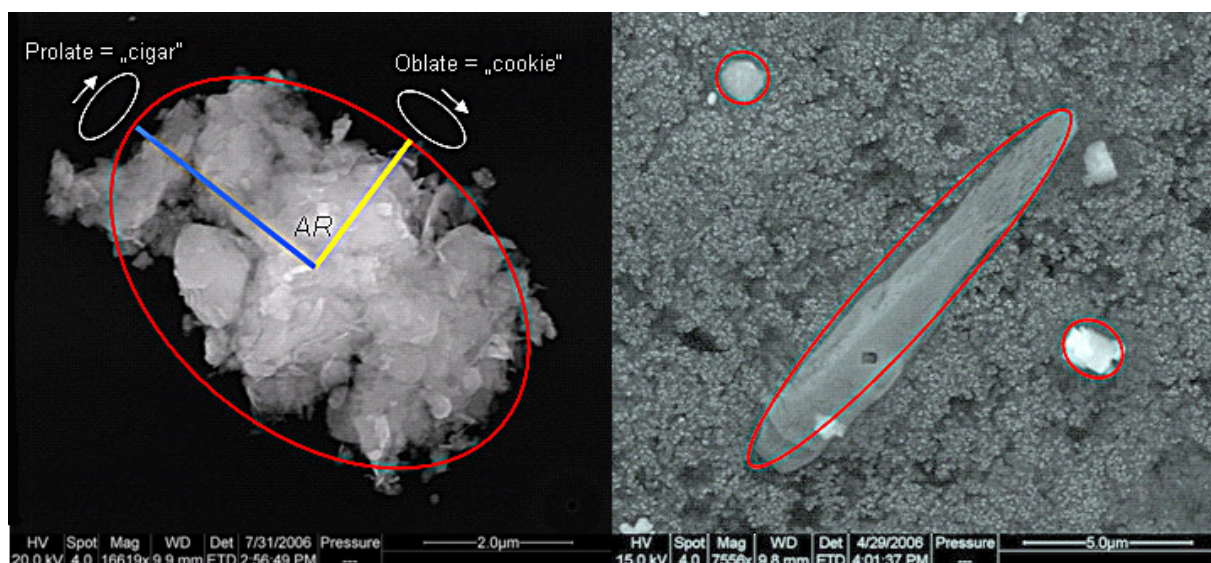
Fig. 3-34: Typical particles found in the Saharan dust plume during SAMUM with the help of a SEM. The particles are rough and non-spherical. The SEM could not distinguish between prolate or oblate particles, only a geometrical cross-section could be observed and used to fit an ellipsis of a certain axis ratio (AR) to each particle. Thus, AR distributions were derived showing maxima at AR=1:1.3 for fine-mode and at AR=1:1.6 for coarse-mode particles.

Observations with the help of the SEM demonstrated that dust particles are typically non-spherical (fig. 3-34). The assumption of an elliptical cross-section for each particle, expressed by the ratio of the half-axes of an adopted ellipse (axis ratio or aspect ratio AR), suited the observations well. Typical aspect ratios of about 1:1.6 were found for coarse particles.

Because of the SEM findings it is questionable whether the consideration of non-spherical particles in calculating dust optical properties and modelling radiative transfer is really needed. In addition it has to be analysed how large the radiative impact due to the particle non-sphericity can be. Thus, we simulated the BSC and LR via Mie theory applying all input data as mentioned before and compared them to the in-situ lidar measurements. It turned out that spheres as model particles could not explain the observations. Obviously the non-sphericity must have certain effects. Therefore we constructed a database of single particle optical properties for oblate and prolate homogeneous spheroids as a function of the volume equivalent size parameter, the real and imaginary part of the complex refractive index as well as of the AR in order to calculate spectral optical properties of dust ensembles which are needed for extensive radiative transfer simulations.

The term 'size' requires special attention if one considers non-spherical model particles. Usually aerosol size distributions are certain functions of the particle size, e.g. in terms of a particular equivalent diameter D_p. Thus, we assumed that each particle with diameter D_p in the given measured size distributions has a spheroidal shape and treated the quantity 'size' in the sense of the following five cases:

- Volume equivalence (VEQV): D_p is the diameter of a sphere having the same volume as the spheroid
- Surface equivalence (SEQV): D_p is the diameter of a sphere having the same surface area as the spheroid
- Volume-to-surface equivalence (VSEQV): D_p is the diameter of a sphere having the same volume-to-surface area ratio as the spheroid
- Longest axis equivalence (LAEQV): $R_p = \frac{1}{2} D_p$ is the length of the longest half-axis of the spheroid
- Shortest axis equivalence (SAEQV): $R_p = \frac{1}{2} D_p$ is the length of the shortest half-axis of the spheroid.

Each case was discussed to account for particle non-sphericity. Note that in order to extract data from the above mentioned database we had to calculate the volume equivalent size parameter in all cases where AR is a free parameter which is then a measure for the non-sphericity. Varying AR one could distinguish between prolate and oblate spheroidal model particles.

We simulated BSC and LR for all the size equivalence cases and found that volume equivalent oblate spheroids with an effective AR of 1:1.6 matched the lidar data of BSC and LR as well as sun photometer measurements of the total optical depth best. Interestingly, this AR was found to be most frequent for coarse particle. Thus, these super-micron particles with their most probable shapes dominate the optical properties of the entire dust ensemble.

Calculating the SSA and the AP from about 0.3 to 2.0 μm wavelength yielded that, in the case of VEQV and an AR of 1:1.6 (oblate shape), the SSA is influenced by up to a magnitude of only 1% by the non-sphericity and the AP is reduced by up to 4% when comparing with spherical particles. Changes in the extinction optical depths were within 3.5%. Obviously, the largest effects occurred with respect to the AP which indicates the enhanced backscattering by the non-spherical particles. Moreover, the value of 0.8 at 550 nm for the SSA via Mie theory as mentioned above is still representative for the observed non-spherical dust plume.

We further performed fine-band radiative transfer simulations and computed irradiances in the spectral range from λ = 0.3-2.0 μm. They agreed to within 5% with measured data. Furthermore, we calculated atmospheric radiative effects (AREs), i.e. spectrally integrated deviations in the net irradiances at the top of the atmosphere (TOA) of a perturbed reference scenario. For the latter case a clear-sky atmosphere with absorbing and Rayleigh scattering air molecules was considered, both over an ocean as well as over a desert surface. The perturbed situation took the measured mineral dust into account. Thus, over desert we had a dust plume from the bottom of the atmosphere up to an altitude of about 4.5 km above ground level and over ocean it corresponded to a lifted layer from about 1.1 to 5.6 km. The ARE

was computed in W m^{-2} for both scenarios as a function of size equivalence as well as AR. It could be taken as a measure for the strength of the cooling (negative values) or warming (positive) of the Earth-atmosphere system (EAS) due to the mineral dust and its non-spherical particles. Fig. 3-35 illustrates how the dust causes a cooling of the EAS over ocean as well as a warming over desert. For an increased degree of non-sphericity, i.e. the smaller the AR lower than 1 (prolate spheroids) or the larger the AR greater than 1 (oblate spheroids), this always results in an enhanced cooling: larger negative values over ocean and smaller positive values over desert. This is due to the forced backscattering by the non-spherical dust particles. Their presence leads to a larger fraction of radiation that is transported back to space. Moreover, the results demonstrate that the size equivalence has a strong impact on the ARE and is very important for accurate radiative transfer modelling.
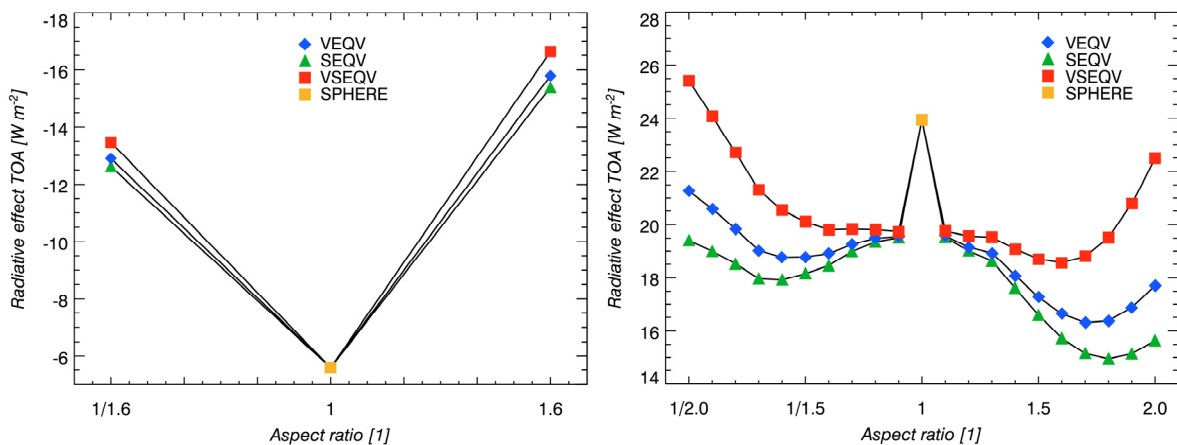

Fig. 3-35: ARE at TOA for the mineral dust over ocean (left panel) and over desert (right) as a function of size equivalence (VEQV, SEQV, VSEQV only) and AR. An AR<1 means prolate spheroids, AR=1 spherical particles and AR>1 oblate spheroids. Over ocean the dust leads to a cooling while it warms the EAS over desert. The non-sphericity always results in an enhanced cooling due to the forced backscattering of the non-spherical dust particles.

Taking the volume equivalent oblate spheroids with an effective AR of 1:1.6 from above (those matching the lidar data best), fig. 3-35 indicates that ARE amounts to about -16 W m^{-2} over ocean and +17 W m^{-2} over desert. For spheres the corresponding values are about -6 W m^{-2} and +24 W m^{-2}. In relative terms this most representative case of non-sphericity during SAMUM leads to a net radiative effect of 167% over ocean and of 29% over desert.

Full details about radiative transfer modelling of a mineral dust Plumes can be found in *Otto et al. (2009)*.

References

Dubovik, O., B.N. Holben, T.F. Eck, A. Smirnov, Y.J. Kaufman, M.D. King, D. Tanre, and I. Slutsker: Variability of absorption and optical properties of key aerosol types observed in worldwide locations, J. Atmos. Sci., 58, 590-608, 2002

Otto, S., M. de Reus, T. Trautmann, A. Thomas, M. Wendisch, and S. Borrmann: Atmospheric radiative effects of an in situ measured Saharan dust plume and the role of large particles, Atmos. Chem. Phys., 7, 4887-4903, 2007

Otto, S., E. Bierwirth, B. Weinzierl, K. Kandler, M. Esselborn, M. Tesche, A. Schladitz, M. Wendisch, and T. Trautmann: Solar radiative effects of a Saharan dust plume observed during SAMUM assuming spheroidal model particles, Tellus, 61B, DOI: 10.1111/j.1600-0889.2008.00389.x, 2009

Sokolik, I.N., D.M. Winker, G. Bergametti, D.A. Gilette, G. Carmichael, Y.J. Kaufman, L. Gomes, L. Schütz, and J.E. Penner: Introduction to special section: Outstanding problems in quantifying the radiative impacts of mineral dust, J. Geophys. Res., 106, No. D16, 18015–18027, 2001

3.21 Radiation, Clouds, and Climate in Planetary Atmospheres

M. Vasquez, F. Schreier, T. Trautmann, M. Gottwald

One of the most exciting challenges in present Space Science / Earth Science is to understand planetary evolution in general and life in particular. The senate of the Helmholtz-Gemeinschaft Deutscher Forschungszentren e.V. (HGF) has addressed this by selecting the theme *Planetary Evolution and Life*, led by the Institute of Planetary Research of DLR at Berlin-Adlershof, as one of its supported research alliances. These alliances are aiming at pursuing innovative approaches in topics of current interest by bringing together experts at Helmholtz centres, universities and non-university facilities. The goal of the alliance *Planetary Evolution and Life* is to study in a multidisciplinary fashion the interaction of the evolution of life and its hosting planet. It comprises the entire planet – dense geosphere (core, mantle, crust), hydrosphere, cryosphere, atmosphere, biosphere and even magnetosphere. Partners of the alliance are

- Helmholtz centres
  - DLR
  - Alfred-Wegener Institute
- Universities
  - Free University of Berlin
  - Technical University of Berlin
  - Humboldt University Berlin
  - Westfälische Wilhelm University Münster
  - University Duisburg/Essen
  - London South Bank University
  - Yale University
- Non-university research institutions
  - Max-Planck Society
  - Observatoire de la Côte d'Azur
  - Austrian Academy of Sciences
- Associated partners
  - Russian Academy of Sciences
  - Pennsylvania State University
  - CNRS Paris
  - CNRS Bordeaux University
  - Technical University of Braunschweig
  - University of Applied Sciences Wildau

A number of parameters determines whether a planet is suitable for the development of life. The type and distance of the central star define pre-conditions for the planet's habitability. In addition, planetary parameters such as mass, composition of the solid body as well as the existence of an atmosphere are factors strongly contributing to habitability. In particular, the atmosphere plays a very important role, since its pressure, temperature and chemical composition set the scene for evolution of life on the planet's surface. In turn, these parameters depend on the incident radiation emitted by the central star and modified by absorption and scattering within the planetary atmosphere. In addition dynamic processes, including e.g. the transport and formation of aerosol particles and clouds at the bottom of the atmosphere as well as escape mechanisms at its top determine how the habitability conditions evolve with time.

IMF-AP contributes to the Helmholtz alliance within topic 1000: *Bio-Atmosphere-Surface Interaction and Life* by providing its know-how in radiative transfer (RT), i.e. the interaction between photons from the central star of a planetary system and the planet's atmosphere. This experience permits to deal with various atmospheric conditions and compositions. The accurate treatment of radiative transfer processes is critical in determining habitability. Furthermore, RT is strongly coupled with chemistry and exchange/transport processes.

In the course of a PhD thesis existing infrared Line-by-Line (LbL) and UV-VIS (multiple scattering) radiative transfer models are extended and optimized. Firstly, the treatment of isotopes needs to be improved. In the next step, scattering shall be implemented in the LbL code allowing realistic infrared RT

modelling in the presence of clouds and aerosols. Such upgrades will enable investigations of radiation balance and radiative heating/cooling rates.

Combining studies of cloud microphysical processes and their effect on RT, atmospheric chemistry and climate with radiative-convective climate models it shall be possible to address cloud related topics like formation, persistence and their effect on climate feedback cycles. Ultimately our codes will contribute to a *modular unified global climate model* tool box.

Conditions for habitability on the surface of terrestrial planets are primarily studied by comparing the evolution of the terrestrial planets with atmospheres in our own solar system: Venus, Earth and Mars (fig. 3-36). Thus it spans a wide range of atmospheric compositions – from the CO_2 loaded extreme greenhouse on Venus via the gentle Earth to the cold Martian environment. Further promising targets in our neighbourhood are the moons of the gas giants Titan (Saturn) and Europa (Jupiter).
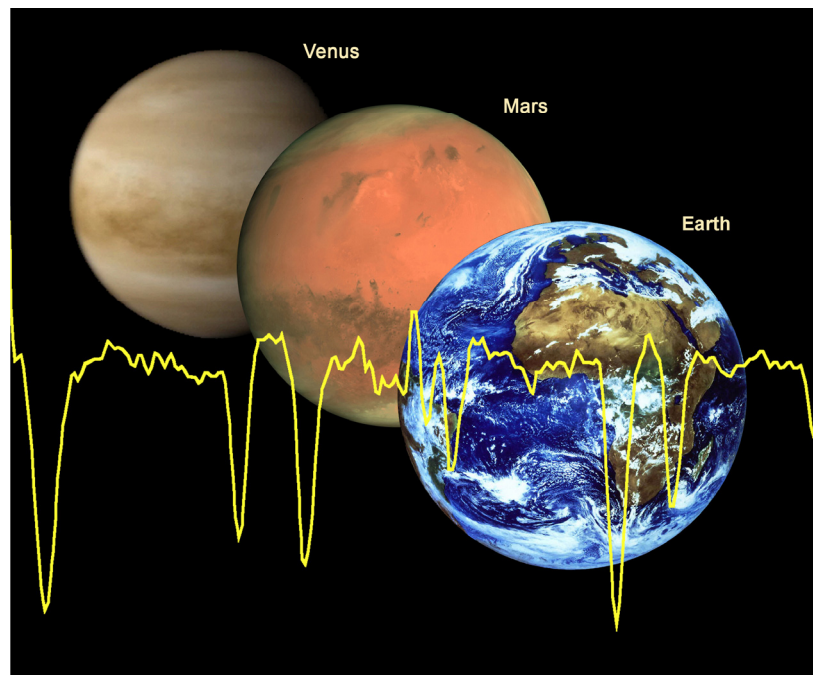
Fig. 3-36: The terrestrial planets in the Solar System with atmospheres. Overlaid is an IR spectrum of Venus at 1.6 μm.

A planet like Earth exhibits its habitability via spectra measured by an external remote observer. So-called biomarkers can be identified in the upwelling radiances. Several interplanetary space missions have measured terrestrial spectra and detected spectral features originating from e.g. oxygen, carbon compounds or water. The modelling of planetary spectra as a function of various input parameters (irradiance, atmospheric composition, surface composition) – one of the major task of our alliance participation – can even be extended to extra-solar planets. Therefore we are capable of determining their spectral 'appearance'. Such studies might be a pre-requisite for finding the *Second Earth*.

3.22 Characterization of Atmospheric Data Quality for an Improved Determination of Earth Gravity Field

E. Fagiolini, G. Schwarz (IMF-PB), T. Trautmann

Highly accurate satellite gravimetry requires a correct modelling of the atmospheric mass including its temporal and spatial variability as well its vertical structure. Basic atmospheric input parameters used during the GRACE data processing are taken from meteorological data sets such as ECMWF or NCEP products. They are spatially resolved and time-tagged maps of surface pressure, temperature profiles and specific humidity. These are state-of-the-art assimilation results combining various measurements and simulations. They include their assumed uncertainties, i.e. their estimated standard deviations, that have physical impact on the gravity field determination.

Alternative calculations of blockmeans, taking into account ECMWF standard deviations, result in clearly visible geoid height differences (fig. 3-37). Previous routine data products did not yet include uncertainties of input data. The simple example presented in fig. 3-37 illustrates the necessity for precise calculation of error propagation.
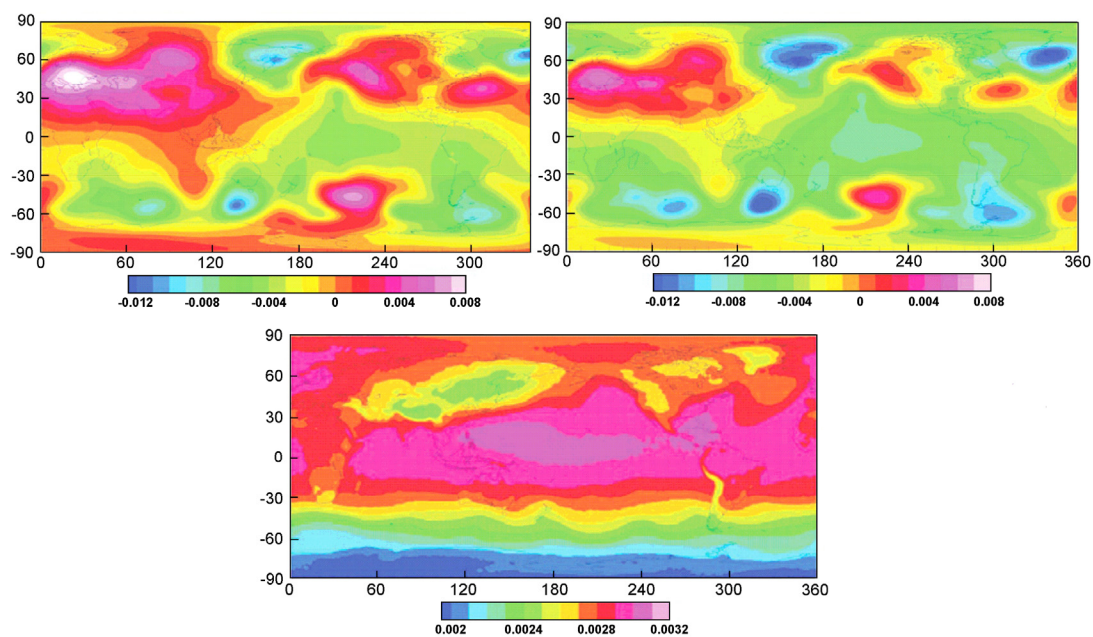
Fig. 3-37: Geoid height variations in m of vertically integrated atmosphere on December 1, 2006, 00:00 UT (top left: arithmetic blockmeans (ABM), top right: weighted blockmeans (WBM), bottom: geoid height differences, courtesy F. Flechtner, GFZ)

In order to understand the propagated gravity field uncertainties and to improve the gravity field determination, we studied and described the atmospheric error bars with respect to their spatial and temporal variations. Further on we performed sensitivity and quality analysis in order to understand the propagated gravity field uncertainties and to improve the gravity field determination. The sensitivity analysis focused both on the identification of the model inputs which contribute most to output variability and on the effects of different predefined input scenarios on the gravity field. Different sensitivity analysis approaches, such as analytical partial derivatives, difference quotient approximation and Monte Carlo simulation, were used and compared.

A numerical sensitivity analysis of atmospheric parameters showed that surface pressure uncertainties are the main reason for geoid errors. Temperature, specific humidity and geopotential heights are less critical. Therefore, we concentrated on surface pressure and its corresponding standard deviation. The surface pressure standard deviations strongly depend on locations and time. Zonal transects show the impacts of continents and oceans. At higher elevations we have lower surface pressure and smaller standard deviations (see fig. 3-38).
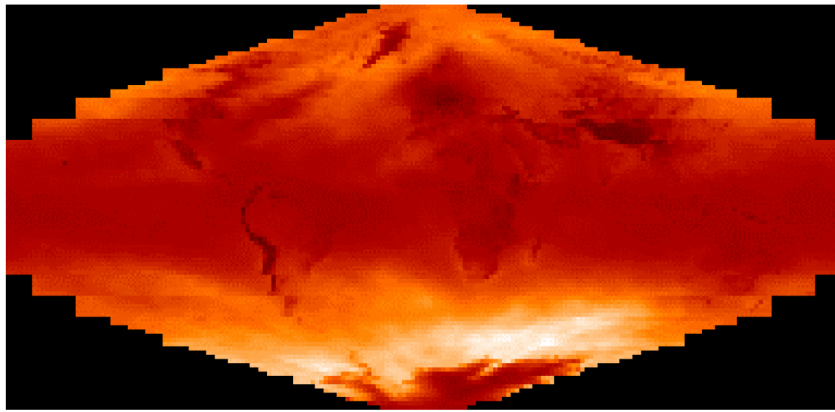
Fig. 3-38: Typical surface pressure standard deviations (min = 40 Pa, max = 90 Pa)

As illustrated below, surface pressure histograms are affected by elevated mountains that result in lower surface pressure values. In contrast, histograms of estimated pressure standard deviations exhibit an opposite asymmetry caused by positive outliers.
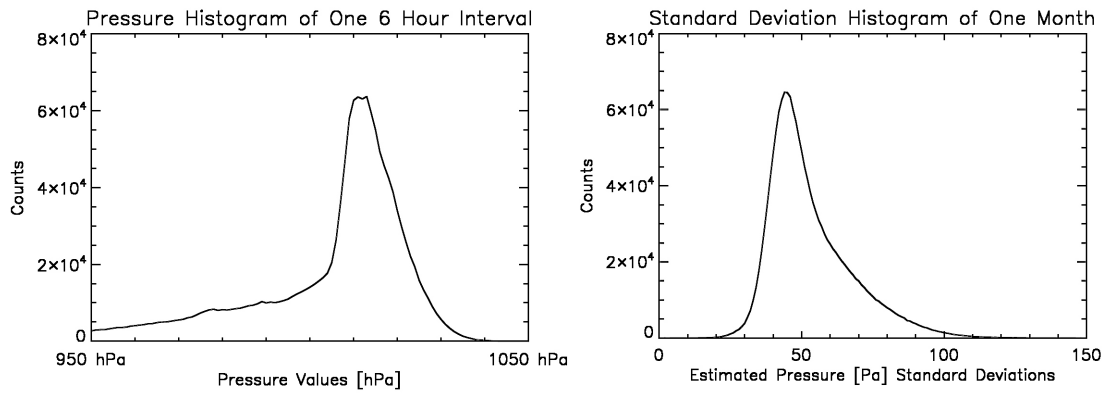
Fig. 3-39: Surface pressure histograms (see text)

Fig. 3-40 demonstrates the diurnal cycle during one month of tropical surface pressure near the equator and the zero meridian. Pronounced minima each 24 hours at 18:00 local time are obvious. At a first glance, this behaviour is invisible in the corresponding standard deviation data. As a consequence, our analysis had to investigate more intricate effects.
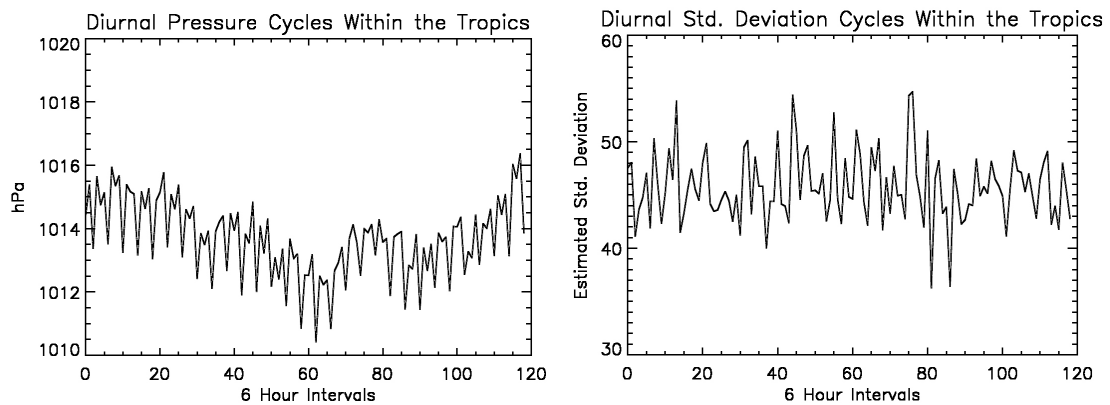
Fig. 3-40: Tropical diurnal pressure cycles (see text)

The validity of ECMWF 6-hour interval standard deviations can be substantially improved by averaging over appropriately selected time periods.

Additionally, the analysis of different surface pressure effects called for a flexible tool to determine their impact. We developed a simulation environment for the analysis and verification of surface pressure effects. The simulator tool consists of a processing part under the control of a Monte Carlo simulator and an analysis/manipulation part permitting the interactive manipulation of surface pressure errors. In particular, it allows the modification of single estimates, bias and random terms, sinusoidal components, geographically confined data as well as time-dependent and multi-scale effects (e.g. trends).
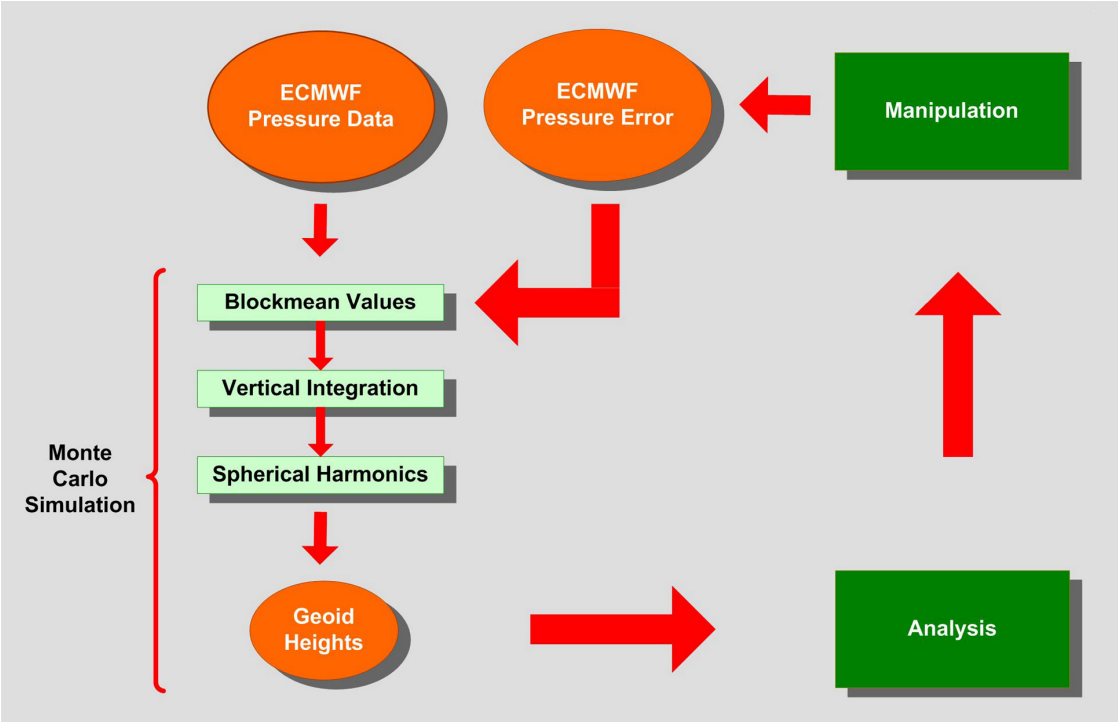
Fig. 3-41: The conceptual layout of the surface pressure simulation environment

3.23 The International Polar Year – IPY

M. Gottwald, D. Floricioiu (IMF-SV)

The polar regions are considered to both play an important role in the Earth system and to response quickly to global change. Therefore observations of the Arctic and Antarctica are of crucial importance for understanding our home planet. Since the advent of modern Earth Sciences there were occasional periods where polar research was coordinated on a global scale via an International Polar Year (IPY). The first IPY occurred in 1881-1884, the last as part of the International Geophysical Year (IGY) in 1957/1958. In March 2007 the current IPY, sponsored by the International Council for Science (ICSU) and the World Meteorological Organization (WMO), started. It will actually span two years and ends in March 2009.

This IPY is the first where the Earth is considered a complex system of interacting spheres (geosphere, hydrosphere, atmosphere, cryosphere, biosphere). Additionally the scientists' capabilities are much improved as compared to the IGY in all areas of ground based, air- and shipborne investigations. Completely absent at the time of the IGY were spaceborne remote sensing methods. In the past five decades since IGY Earth Observation from space has become a new and essential technique to explore the Earth. Particularly studies in the remote polar sites gained significantly with the provided opportunities. Not only did satellite platforms in polar orbits cover the entire region at high latitudes within a few days but also carried instruments where measurements became independent of weather conditions.

WMO has established the Space Task Group (STG) comprising nominated representatives of Space Agencies with WMO providing the secretarial support. STG is tasked with coordinating Earth Observation missions in support of IPY projects. It establishes the dialog between IPY projects and Space Agencies aiming at developing recommendations to Space Agencies on data acquisition plans, processing, archiving, and distribution of satellite data, products and services. All contributions by Space Agencies shall be consistent with each respective Agency's own resources and capabilities – and which in total could satisfy IPY satellite data needs.

Four different goals have been formulated by STG, all being a 'first' in their particular area:

- For the first time, pole to coast multi-frequency InSAR measurements of ice-sheet surface velocity
- For the first time, repeat fine-resolution SAR mapping of the entire Southern Ocean sea-ice cover for sea ice motion
- For the first time, one complete high resolution visible and thermal IR (VIS/IR) snapshot of circumpolar permafrost
- For the first time, pan-Arctic high and moderate resolution Vis/IR snapshots of freshwater (lake and river) freeze-up and break-up.

It is obvious that these goals address high resolution missions in the microwave and optical domain requiring specific planning activities for acquisitions. Low resolution instruments are considered to generate data on a continuous basis and are therefore much less subject to coordination.

DLR is one of the STG members. We contribute TerraSAR-X and SCIAMACHY on ENVISAT to the international fleet of IPY relevant missions. While TerraSAR-X represents a high resolution microwave sensor, SCIAMACHY is a member of the low resolution type. IMF-AP involvement in IPY is twofold, since we provide the STG DLR representative and promote usage of SCIAMACHY data for polar research.

In 2008 the first topic mainly addressed radar issues, i.e. not necessarily the genuine realm of atmospheric processors. However, because significant effort was spent in cooperation with colleagues from IMF-SV and DFD-US to optimize TerraSAR-X acquisitions over the Arctic and Antarctica we think it is worth mentioning it here. A microwave working group, formed by the Canadian Space Agency CSA,

the European Space Agency ESA, the Italian Space Agency ASI, the Japanese agency JAXA and DLR convened twice under the scientific auspices of the GIIPSY project (Global Inter-agency IPY Polar Snapshot Year). The second meeting was held at the DLR premises at Oberpfaffenhofen. It successfully triggered the acquisitions of TerraSAR-X over selected polar sites. In November these campaigns started with observations a tributary ice stream feeding into the Recovery Glacier (81°S, 20°W) in Antarctica. Such measurements are sensitive to fine structures on ice and snow surfaces. They will provide detailed insights into flow dynamics of glaciers and ice streams.

Promotion of SCIAMACHY data for IPY related applications occurred in collaboration with IUP/IFE, University of Bremen. The Earth's atmosphere above the polar caps exhibits several phenomena not observed at low latitude regions. Caused by their remote location, polar regions do not show high concentrations of tropospheric polluting trace gases or particles. However this 'cleanliness' makes them vulnerable to external perturbations. Particularly the stratosphere over Antarctica had created large public interest with the detection of the ozone hole end of the past century illustrating impressively anthropogenic impacts on the Earth system. ENVISAT's high inclination orbit carries SCIAMACHY each day 14 times over the arctic and antarctic region. Due to SCIAMACHY's flexible viewing geometries the polar atmosphere can be sensed through all relevant layers. In the past almost 7 years SCIAMACHY has monitored their status from the bottom (troposphere) up to its top (mesosphere/thermosphere). A wealth of data is available and awaits detailed analyses to retrieve a long record of polar geophysical parameters contributing to the understanding of our changing environment.
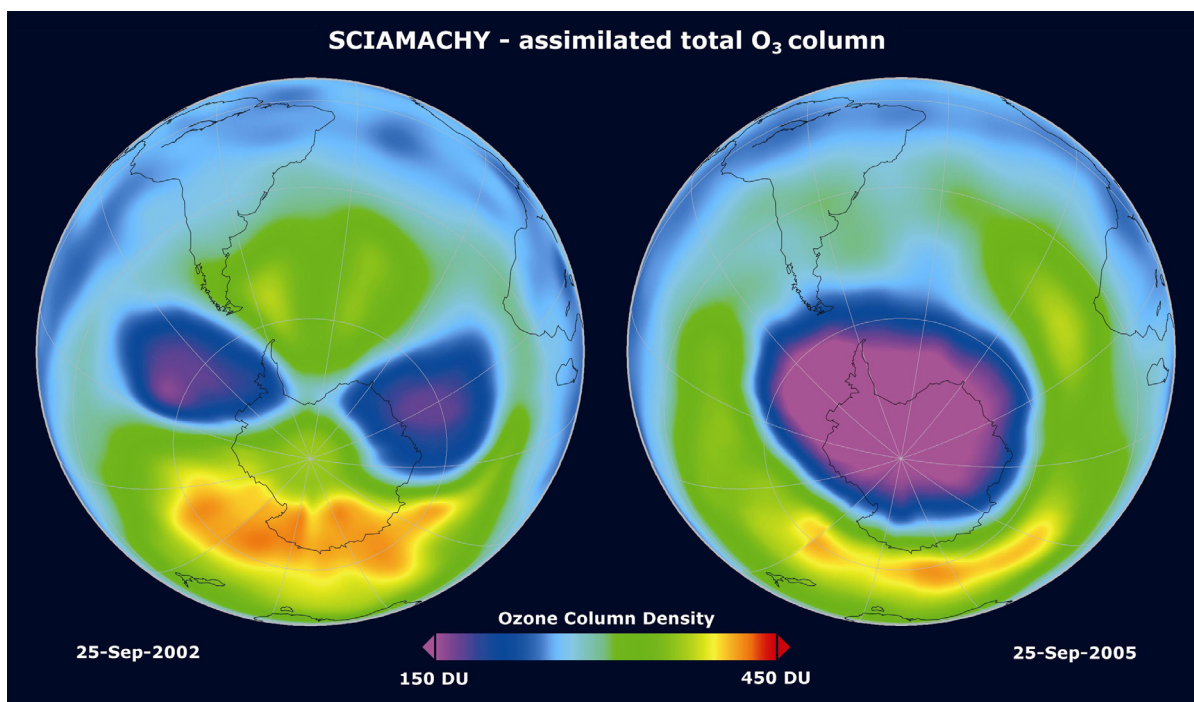

Fig. 3-42: The Antarctic ozone hole in 2002 and 2005 as derived from SCIAMACHY data (image: T. Erbertseder, DFD-KA, from the book *SCIAMACHY – Monitoring the Changing Earth's Atmosphere*)

4. Documentation

4.1 Books and Book Contributions

Badaoui, M., F. Schreier, G. Wagner, M. Birk: Instrumental Line Shape Function for High Resolution Fourier Transform Molecular and Atmospheric Spectroscopy, In: Kaufer, Andreas; Kerber, Florian [Hrsg.]: *The 2007 ESO Instrument Calibration Workshop, ESO Astrophysics Symposia*, Springer-Verlag, 391-396, ISBN 978-3-540-76962-0, 2008

Doicu, A., R. Schuh, T. Wriedt: Scattering by particles on or near a plane surface, In: Kokhanovsky, Alexander A. [Hrsg.]: *Light Scattering Reviews 3, Light Scattering and Reflection*, Springer Praxis Books, Springer Berlin Heidelberg, 109-130, ISBN 978-3-540-48305-2 (Print) 978-3-540-48546-9 (Online), 2008

4.2 Journal Papers

Antón, M., D. Loyola, B. Navascúes, P. Valks: Comparison of GOME total ozone data with ground data from the Spanish Brewer spectroradiometers, *Annales Geophysicae*, 26 (3), European Geosciences Union, 401-412, ISSN 0992-7689, 2008

Bamler, R., M. Eineder, P. Haschberger, T. Trautmann: Erdbeobachtung aus dem Weltraum und aus der Luft, media mind GmbH [Hrsg.]: *Luft- und Raumfahrt in Bayern*, 16-20, 2008

Bamler, R., M. Eineder, P. Haschberger, T. Trautmann: Earth Observation from Space and from the Air, media mind [Hrsg.]: *Luft- und Raumfahrt in Bayern*, 16-20, 2008

Bierwirth, E., M. Wendisch, A. Ehrlich, S. Heese, M. Tesche, D. Althausen, A. Schladitz, D. Müller, S. Otto, T. Trautmann, T. Dinter, W. von Hoyningen-Huene: Spectral surface albedo over Morocco and its impact on the radiative forcing of Saharan dust, *Tellus B - Chemical and Physical Meteorology*, 61B, 2008

Coldewey-Egbers, M., S. Slijkhuis, B. Aberle, D. Loyola: Long-term analysis of GOME in-flight calibration parameters and instrument degradation, *Applied Optics*, 47 (26), 4749-4761, DOI 10.1364/AO.47.004749, 2008

Doicu, A., T. Trautmann: Discrete ordinate method with matrix exponential for a pseudo-spherical atmosphere: Scalar case, *Journal of Quantitative Spectroscopy and Radiative Transfer*, 110 (1-2), 146-158, DOI 10.1016/j.jqsrt.2008.09.014, 2008

Doicu, A., T. Trautmann: Discrete ordinate method with matrix exponential for a pseudo-spherical atmosphere: Vector case, *Journal of Quantitative Spectroscopy and Radiative Transfer*, 110 (1-2), 159-172, DOI: 10.1016/j.jqsrt.2008.09.013, 2008

Gottwald, M.: Die Kartierung des Mondes. Teil 1: Von den Anfängen bis ins 19. Jahrhundert, *Sterne und Weltraum*, 7, 52-62, 2008

Gottwald, M.: Die Kartierung des Mondes. Teil 2: Von den Anfängen der Fotografie bis zum Beginn der Erkundung vor Ort, *Sterne und Weltraum*, 8, 52-61, 2008

Hungershöfer, K., K. Zeromskiene, Y. Iinuma, G. Helas, J. Trentmann, T. Trautmann, R.S. Parmar, A. Wiedensohler, A. Meinrat, O. Schmid: Modelling the optical properties of fresh biomass burning aerosol produced in a smoke chamber: results from the EFEU campaign, *Atmospheric Chemistry and Physics*, 8, 3427-3439, 2008

Jacquinet-Husson, N., N.A. Scott, N. Chedin, A. Crépeau, R. Armante, V. Capelle, J. Orphal, A. Coustenis, C. Boone, N. Poulet-Crovisier, A. Barbe, M. Birk, L.R. Brown, C. Camy-Peyret, C. Claveau, K. Chance, N. Christidis, C. Clerbaux, P.F. Coheur, V. Dana, L. Daumont, M.R. De Backer-Barilly, G. Di Lonardo, J.-M. Flaud, A. Goldman, A. Hamdouni, M. Hess, M.D. Hurley, D. Jacquemart, I. Kleiner, P. Koepke, J.Y. Mandin, S. Massie, S. Mikhailenko, V. Nemtchinov, A. Nikitin, D. Newnham, A. Perrin, V.I. Perevalov, S. Pinock, L. Régalia-Jarlot, C.P. Rinsland, A. Rublev, F. Schreier, L. Schult, K.M. Smith, S.A.

Tashkun, J.L. Teffo, R.A. Toth, V.G.Tyuterev, J. Vander-Auwera, P. Varanasi, G. Wagner: The GEISA spectroscopic database: Current and future archive for Earth and planetary atmosphere studies, *Journal of Quantitative Spectroscopy and Radiative Transfer*, 109 (6), Elsevier, 1043-1059, DOI: 10.1016/j.jqsrt.2007.12.015, 2008

Loyola, D., J. van Geffen, P. Valks, T. Erbertseder, M. Van Roozendael, W. Thomas, W. Zimmer, K. Wißkirchen: Satellite-based detection of volcanic sulphur dioxide from recent eruptions in Central and South America, *Advances in Geosciences*, 14, Copernicus Publications on behalf of the European Geosciences Union, 35-40, 2008

Otto, S., T. Trautmann: A note on G-functions within the scope of radiative transfer in turbid vegetation media, *Journal of Quantitative Spectroscopy and Radiative Transfer*, DOI 10.1016/j.jqsrt.2008.08.003, 2008

Otto, S., E. Bierwirth, B. Weinzierl, K. Kandler, M. Esselborn, M. Tesche, A. Schladitz, M. Wendisch, T. Trautmann: Solar radiative effects of a Saharan dust plume observed during SAMUM assuming spheroidal model particles, *Tellus B - Chemical and Physical Meteorology*, 61B (1), 270-296, DOI: 10.1111/j.1600-0889.2008.00389.x, 2008

Schmidt, T., J. Wickert, S. Heise, F. Flechtner, E. Fagiolini, G. Schwarz, L. Zenner, T. Gruber: Comparison of ECMWF analyses with GPS radio occultations with GRACE, *Annales Geophysicae*, 26 (11), European Geosciences Union, 3225-3234, ISSN 1432-0576, 2008

Schreier, F., D. Kohlert: Optimized implementations of rational approximations – a case study on the Voigt and complex error function, *Computer Physics Communications*, 179 (7), Elsevier, 457-465, DOI: 10.1016/j.cpc.2008.04.012, 2008

Tan, D.G.H., E. Andersson, J. de Kloe, G.-J. Marseille, A. Stoffelen, P. Poli, M.-L. Denneulin, A. Dabas, D. Huber, O. Reitebuch, P. Flamant, O. Le Rille, H. Nett: The ADM-Aeolus wind retrieval algorithms, *Tellus A - Dynamic Meteorology and Oceanography*, 60, 191-205, DOI: 10.1111/j.1600-0870.2007.00285.x, 2008

von Paris, P., H. Rauer, J.L. Grenfell, B. Patzer, P. Hedelt, B. Stracke, T. Trautmann, F. Schreier: Warming the early Earth - CO2 reconsidered, Schulz, R [Hrsg.]: *Planetary and Space Science*, 56 (9), Elsevier, 1244-1259, ISSN 0032-0633, DOI: 10.1016/j.pss.2008.04.008, 2008

Worringen, A., M. Ebert, T. Trautmann, S. Weinbruch, G. Helas: Optical properties of internally mixed ammonium sulfate and soot particles - a study of individual aerosol particles and ambient aerosol populations, *Applied Optics*, 47 (21), S. 3835-3845, DOI: 10.1364/AO.47.003835, 2008

4.3   Conference Proceeding Papers and Presentations

Bovensmann, H., A. Rozanov, C. von Savigny, K.U. Eichmann, K. Bramstedt, L.K. Amekudzi, J.P. Burrows, A. Doicu, G. Lichtenberg, M. Gottwald, J.A.E. van Gijsel, T. Fehr: Monitoring of Stratospheric O3 and NO2 Profiles with SCIAMACHY/ENVISAT, Quadrennial Ozone Symposium, Tromsø, Norway, 2008

Chiou E., R.D. McPeters, P. Veefkind, D. Loyola: Characteristics of zonal variations of total column ozone from OMI(TOMSv8.5), OMI(DOAS), GOME-2, and SCIAMACHY measurements during 2007-2008, AGU, San Francisco, United States, 2008

Doicu, A.: Scattering by systems of particles on or near a plane surface, Mie Theory 1908-2008 – Present developments and interdisciplinary aspects of light scattering, Invited talk, University of Halle-Wittenberg, Halle, 2008

Ehret, G., C. Kiemle, A. Börner, K. Günther, T. Trautmann, H. Schwarzer, J.T. Grundmann, B. Kazeminejad, S. Montenegro, P. Spietz: The mission Charm-SSB, a new perspective for active remote sensing of methane and vegetation height using DLR`s standard satellite bus SSB, 37th COSPAR Scientific Assembly 2008, Montreal, Canada, 2008

Erbertseder T., J. Meyer-Arnek, D. Loyola, F. Baier: First MetOp/GOME-2 chemical analysis of the 2007 Antarctic Ozone Hole, EUMETSAT Meteorological Satellite Conference, Darmstadt, September, 2008

Fagiolini, E., F. Flechtner, T. Gruber, T. Schmidt, G. Schwarz, T. Trautmann, J. Wickert, L. Zenner: Characterization of atmospheric data quality for an improved determination of Earth gravity fileds, EGU General Assembly, Vienna, Austria, 2008

Fagiolini, E., F. Flechtner, T. Gruber, T. Schmidt, G. Schwarz, T. Trautmann, J. Wickert, L. Zenner: Atmospheric Parameters and Geoid Heights: Mathematical Aspects, Geodätische Woche, Bremen, 2008

Floricioiu, D., M. Gottwald, E. Diedrich, A. Roth, M. Eineder: TerraSAR-X Capabilities in Polar Regions, SCAR/IASC IPY Open Science Conference: Polar Research – Arctic and Antarctic Perspectives in the International Polar Year, St. Petersburg, Russia, 2008

Gottwald, M.: Die Entstehung unseres Sonnensystems, public lecture, Munich, June 6, 2008

Gottwald, M., E. Krieg, G. Lichtenberg, C. von Savigny, S. Noel, P. Reichl, A. Richter, H. Bovensmann, C. Robert, M. Weber, J.P. Burrows: Exploring the Polar Atmosphere with SCIAMACHY, Polar Research - Arctic and Antarctic Perspectives in the International Polar Year, St. Petersburg, Russia, 2008

Gottwald, M.: Das Bild der Erde, public lecture, Trebur, September 19, 2008

Gottwald, M.: Das Bild der Erde, public lecture, Munich, November 14, 2008

Gottwald, M., E. Krieg, S. Noel, H. Bovensmann, K. Bramstedt, R. Snel: The SCIAMACHY Extended Mission, 37th COSPAR Scientific Assembly, Montreal, Canada, 2008

Gruber, T., E. Fagiolini, F. Flechtner, T. Schmidt, G. Schwarz, D. Stammer, T. Trautmann, J. Wickert, L. Zenner: Introduction to the IDEAL-GRACE Project and General Status, SPP 1257 Kolloquium, Munich, 2008

Hao, N., P. Valks, D. Loyola, M. Rix, W. Zimmer, D. Balis: One year of total ozone and SO2 measurement from GOME-2, 4th International DOAS workshop, Hefei, China, 2008

Hao, N., P. Valks, M. Rix, D. Loyola, M. Van Roozendael, G. Pinardi, J.-C Lambert, N. Theys, W. Zimmer, S. Emmadi: Operational O3M-SAF trace-gas column products: GOME-2 tropospheric NO2, Ozone, and total SO2, 7th AT-2 workshop, Helsinki, Finland, 2008

Heinen T., B. Buckl, T. Erbertseder, S. Kiemle, D. Loyola: Standardized Data Access Services for GOME-2/MetOp Atmospheric Trace Gas Products, EUMETSAT Meteorological Satellite Conference, Darmstadt, September, 2008

Kniffka, A., T. Trautmann: Combining the independent pixel and point-spread function approaches to simulate the actinic radiation field in moderately inhomogeneous 3D cloudy media, International Radiation Symposium (IRS2008), Foz do Iguaçu, Brazil, 2008

Köhler, C.H., E. Lindermeir, T. Trautmann: Measurement of mixed biomass burning and mineral dust aerosol in the thermal infrared, 3rd International Workshop on Mineral Dust, Leipzig, 2008

Köhler, C.H., E. Lindermeir, T. Trautmann: Measurement of mixed biomass burning and mineral dust aerosol in the thermal infrared, International Radiation Symposium (IRS2008), Foz do Iguaçu, Brazil, 2008

Kujanpää, J., D. Loyola, O. Tuinder, F. Karcher, H. Sørensen, D. Balis, L. Kins, A. Delcloo, C. Clerbaux, J.-C. Lambert: O3M-SAF: Ozone, Trace Gas and UV Products from EPS/Metop, Quadrennial Ozone Symposium, Tromsø, Norway, 2008

Lang R., R. Munro, Y. Livschitz, S. Hassinen, J. Kujanpää, D. Loyola, P. Stammes, O. Tuinder, P. Valks: GOME-2 - Achievements and Future Perspectives, AGU, San Francisco, United States, 2008

Loyola D.: Ozone Time Series from European Satellites and Coupled Climate-Chemistry Models, CEOS Atmospheric Composition Constellation Workshop, New York, United States, 2008

Loyola D., P. Valks, W. Zimmer, S. Kiemle., D. Balis, J.-C. Lambert, M. Van Roozendael, M. Koukouli, van J. Gent, N. Hao, T. Ruppert, K.-H. Seitz: O3M-SAF Pre-operational Products: GOME-2 Total Column Ozone and NO2, EUMETSAT Meteorological Satellite Conference, Darmstadt, 2008

Loyola D., M. Coldewey-Egbers, M. Dameris, H. Garni, D. Balis, M. Koukouli, M. Van Roozendael, C. Lerot, T. Erbertseder, P. Valks, W. Zimmer, J.-C. Lambert, R. Spurr: Trend Analysis of GOME/SCIAMACHY/GOME-2 Total Column Ozone from 1995 to 2008, Quadrennial Ozone Symposium, Tromsø, Norway, 2008

Loyola D., P. Valks, T. Erbertseder, S. Kiemle, D. Balis, W. Zimmer, J. Meyer-Arnek, T. Ruppert, A. Craubner, K.-H. Seitz: Polar ozone monitoring with GOME-2/MetOp, EGU General Assembly, Vienna, Austria, 2008

Munro R., R. Lang, Y. Livschitz, J. Kujanpää, D. Loyola, P. Valks, P. Stammes, O. Tuinder: GOME-2 Mission and Product Validation Status, EUMETSAT Meteorological Satellite Conference, Darmstadt, 2008

Otto, S., T. Trautmann, E. Bierwirth, M. Wendisch, B. Weinzierl, K. Kandler, M. Esselborn, M. Tesche: Solar radiative effects of non-spherical mineral dust particles during SAMUM 2006, 3rd International Workshop on Mineral Dust, Leipzig, 2008

Otto, S., T. Trautmann: Exact G-functions for various leaf normal distribution functions applied to analytical two-stream radiative transport in turbid vegetation media, International Radiation Symposium (IRS2008), Foz do Iguaçu, Brazil, 2008

Pflug, B., B. Aberle, D. Loyola, P. Valks: Near-real-time estimation of spectral surface albedo from GOME-2/Metop measurements, EUMETSAT Meteorological Satellite Conference, Darmstadt, 2008

Rix, M., P. Valks, N. Hao, T. Erbertseder: Monitoring volcanic SO2 emissions using the GOME-2 satellite instrument, EGU General Assembly, Vienna, Austria, 2008

Rix, M., C. Maerker, K. Seidenberger, P. Valks, T. Erbertseder: Monitoring volcanic SO2 plumes using the GOME-2 satellite instrument, Statusseminar: Early Warning Systems in Earth Management, Osnabrück, 2008

Rix, M. P. Valks, N. Hao, T. Erbertseder, J. Van Geffen: Monitoring of volcanic SO2 emissions using the GOME-2 satellite instrument, 2nd workshop on USE of Remote Sensing Techniques (USEReST) for Monitoring Volcanoes and Seismogenic Areas, Naples, Italy, 2008

Schmidt, T., E. Fagiolini, F. Flechtner, S. Heise, J. Wickert: Comparison of ECMWF analyses with GPS radio occultations, EGU General Assembly, Vienna, Austria, 2008

Schmidt, T., E. Fagiolini, G. Schwarz, T. Trautmann, J. Wickert: The Determination of Representative Errors for the Atmospheric Parameters, SPP 1257 Kolloquium, Munich, 2008

Schreier, F., S. Gimeno-Garcia, M. Hess, A. Doicu, G. Lichtenberg: Retrieval of Carbon Monoxide Vertical Column Densities from SCIAMACHY Infrared Nadir Observations, 37th COSPAR Scientific Assembly, Montreal, Canada, 2008

Schreier, F., S. Gimeno-Garcia, A. Doicu, M. Hess, G. Lichtenberg, A. von Bargen: SCIAMACHY Infrared Nadir Retrievals with BIRRA, SADDU (SCIAMACHY Algorithm Development and Data Usage) Workshop, Bremen, 2008

Schreier, F., S. Gimeno-Garcia, M. Hess, A. Doicu, G. Lichtenberg: Retrieval of CO Vertical Columns from SCIAMACHY Infrared Nadir Observations, International Radiation Symposium (IRS2008), Foz do Iguaçu, Brazil, 2008

Schreier, F., A. Doicu, M. Birk, G. Wagner, M. Badaoui, J. Mendrok: Far Infrared Activities at DLR – Remote Sensing Technology Institute, SMILES International Workshop 2008, Kyoto, JAPAN, 2008

Tan, D.G.H., E. Andersson, J. de Kloe, G.-J. Marseille, A. Stoffelen, P. Poli, A. Dabas, D. Huber, O. Reitebuch, P. Flamant, A.-G. Straume, O. Le Rille, H. Nett: ADM-Aeolus Wind Retrieval Algorithms for NWP, 9th International Winds Workshop, Annapolis, MD (USA), 2008

Valks, P., N. Hao, M. Van Roozendael, J.-C. Lambert, G. Pinardi, F. Goutail, E. Kyro, D. Loyola, W. Zimmer, S. Emmadi: Retrieval of total and tropospheric NO2 from GOME-2/MetOp, EGU General Assembly, Vienna, Austria, 2008

Valks, P., S. Emmadi, J.-C. Lambert, D. Loyola, G. Pinardi, M. Van Roozendael, W. Zimmer: Retrieval of tropospheric NO2 and O3 from the GOME-2 instrument on MetOp, Quadrennial Ozone Symposium 2008, Tromsø, Norway, 2008

Valks, P., S. Emmadi, N. Hao, J.-C. Lambert, D. Loyola, G. Pinardi, M. Rix, M. Van Roozendael, N. Theys, W. Zimmer: Upcoming O3M-SAF trace-gas column products: GOME-2 tropospheric NO2, total BrO and SO2, EUMETSAT Meteorological Satellite Conference, Darmstadt, 2008

Venema, V., S. Gimeno-García, C. Simmer: A new algorithm for the downscaling of 3-dimensional cloud fields, EGU General Assembly, Vienna, Austria, 2008

Venema, V., S. Gimeno-García, C. Simmer: A new algorithm for the downscaling of 3-dimensional cloud fields, International Radiation Symposium, Foz do Iguaçu, Brazil, 2008

Wauer, J., K. Schmidt, T. Rother: Scattering data base for nonspherical particles, GAeF Conference on Light Scattering, Karlsruhe, 2008

Wauer, J., T. Rother, K. Schmidt: Scattering data base for nonspherical particles, Mie Theory 1908-2008 – Present developments and interdisciplinary aspects of light scattering, Halle, 2008

Wauer, J., T. Rother: Considerations to Rayleigh's Hypothesis, Mie Theory 1908-2008 – Present developments and interdisciplinary aspects of light scattering, Halle, 2008

Wendisch, M., E. Bierwirth, S. Bauer, S. Otto, T. Trautmann: Major factors influencing local dust radiative forcing, 3rd International Workshop on Mineral Dust, Leipzig, 2008

4.4   Technical Reports

Balis, D., M. Koukouli, D. Loyola, P. Valks, N. Hao: Second Validation report of GOME-2 total ozone products (OTO/O3, NTO/O3) processed with GDP4.2, Iss./Rev. 2, November 2008

Gottwald, M., E. Krieg, J. How, K. Reissig: SCIAMACHY Consolidated Level 0: Statistics for the Year 2008, PO-TN-DLR-SH-0019, Issue 1, Rev. 0, 14 April 2008

Lambert, J.-C., G. Pinardi, N. Hao, and P. Valks: GOME-2 GDP 4.2 total NO2 (NTO/OTO) validation update and tropospheric NO2 validation set-up, TN-IASB-GOME2-O3MSAF-NO2-02_ORR-B_0, Iss./Rev. ORR-B/0, November 2008

Loyola D., W. Zimmer, S. Kiemle, P. Valks, T. Ruppert: Product User Manual for GOME Total Columns of Ozone, Minor Trace Gases, and Cloud Properties, DLR/GOME/PUM/01, Iss./Rev. 2/A, December 2008

Otto, S., T. Trautmann: Fast analytical two-stream radiative transfer methods for horizontally homogeneous vegetation media, In: Raabe, Armin [Hrsg.]: Meteorologische Arbeiten (XIII) und Jahresbericht 2007 des Instituts für Meteorologie der Universität Leipzig, Wissenschaftliche Mitteilungen aus dem Institut für Meteorologie der Universität Leipzig, 16 p., ISBN 978-3-9811114-2-2, 2008

Schreier, F., S. Gimeno-Garcia, G. Lichtenberg: SCIAMACHY Infrared Nadir Level 1-2 Data Processing Algorithm Theoretical Basics and Intercomparison Study, Technical Report, 2008

Valks, P., D. Loyola: Algorithm Theoretical Basis Document for GOME-2 Total Column Products of Ozone, Minor Trace Gases, and Cloud Properties (GDP 4.2 for O3M-SAF OTO and NTO), DLR/GOME-2/ATBD/01, Iss./Rev. 2/A, November 2008

Van Geffen, J., M. Van Roozendael, M. Rix, P. Valks: Initial validation of GOME-2 GDP 4.2 SO2 total columns – ORR B, Iss./Rev. 1/0, November 2008

4.5 Attended Conferences

SMILES International Workshop, Kyoto, Japan, March 17-19, 2008

SPP1257 Mass Transport and Mass Distribution in the Earth System Workshop, Herrsching, March 31 – April 2, 2008

4th International DOAS workshop, Hefei, China, March 31 – April 2, 2008

HGF Alliance Week, Berlin, May 13-16, 2008

EGU General Assembly, Vienna, Austria, April 13-18, 2008

Quadrennial Ozone Symposium, Tromsø, Norway, June 29 – July 5, 2008

GAeF Conference on Light Scattering, Karlsruhe, July 3/4, 2008

SCAR/IASC Open Science Conference: Polar Research – Arctic and Antarctic Perspectives in the International Polar Year, St. Petersburg, Russia, July 8-11, 2008

37th COSPAR Scientific Assembly, Montreal, Canada, July 13-20, 2008

International Radiation Symposium (IRS2008), Foz do Iguaçu, Brazil, August 3-8, 2008

EUMETSAT Meteorological Satellite Conference, Darmstadt, September 8-12, 2008

International Conference on Mie Theory 1908-200: Present developments and interdisciplinary aspects of light scattering, Halle, September 15-17, 2008

3rd International Workshop on Mineral Dust, Leipzig, September 15-17, 2008

EuroPlanet – European Planetary Science Congress, Münster, September 21-26, 2008

Geodätische Woche, Bremen, September 30 – October 2, 2008

SPP1257 Mass Transport and Mass Distribution in the Earth System Kolloquium, Munich, October 6-8, 2008

CEOS Atmospheric Composition Constellation Workshop, New York, United States, October 15-17, 2008

Helmholtz-EOS-Konferenz, Potsdam, October 28/29, 2008

4.6 Diploma and Doctoral Theses

Fagiolini, E.: The impact of atmospheric variability on the determination of the gravity field of the Earth. Dissertation, Faculty of Civil Engineering and Geodesy, Technical University of Munich. (Supervisors: Prof. Dr. Reiner Rummel, Technical University of Munich and Gottfried Schwarz)

Gimeno-García, S.: Simulation of solar radiative transfer and comparison with spectro-radiometric measurements. Dissertation, Faculty of Physics and Earth Science, University of Leipzig. (Supervisor: Prof. Dr. Thomas Trautmann)

Hiebsch, A.: Light scattering on nonspherical particles, especially Chebyshev particles, and their application in remote sensing. Diploma Thesis, Faculty of Physics and Earth Science, University of Leipzig. Submitted in May 2008 (Supervisors: Prof. Dr. Thomas Trautmann and Dr. Tom Rother)

Kniffka, A.: Influence of the inhomogeneity of aerosols, surface albedo and clouds on the actinic radiation field in the atmosphere. Dissertation, Faculty of Physics and Earth Science, University of Leipzig. Submitted in February 2008 (Supervisor: Prof. Dr. Thomas Trautmann)

Köhler, C.H.: Observation and simulation of the longwave radiative effects for Saharan mineral dust plumes. Dissertation, Faculty of Physics, Mathematics and Computer Science, Johannes Gutenberg University of Mainz. (Supervisors: Prof. Dr. Manfred Wendisch, Johannes Gutenberg University of Mainz and Prof. Dr. Thomas Trautmann)

Otto, S.: Optical properties of mineral dust and its climatic impact on radiative transfer in the Earth's atmosphere. Dissertation, Faculty of Physics, Ludwig Maximilian University of Munich. (Supervisors: Prof. Dr. Olaf Krüger, Ludwig Maximilian University of Munich and Prof. Dr. Thomas Trautmann)

Rix, M.: Observation of volcanic SO_2 plumes based on the satellite-borne GOME-2 instrument. Dissertation, Faculty of Civil Engineering and Geodesy, Technical University of Munich. (Supervisors: Prof. Dr. Richard Bamler, Technical University of Munich and Dr. Pieter Valks)

Szopa, M.: Inversion methods for atmospheric nadir infrared sounding. Dissertation, Faculty for Mathematics and Science, University of Potsdam. (Supervisors: Prof. Dr. Christine Böckmann, University of Potsdam and Dr. Adrian Doicu)

Tröller, A.: Rayleigh-Hypothese im Fall der Streuung an 3-dimensionalen Objekten. Diploma Thesis, Faculty of Physics and Earth Science, University of Leipzig. (Supervisors: Prof. Dr. G. Rudolph and Dr. Tom Rother)

Vasquez, M.: Simulation of the radiation field in planetary atmospheres. Dissertation, Centre of Astronomy and Astrophysics, Technical University of Berlin. (Supervisors: Prof. Dr. Heike Rauer, German Aerospace Center, Institute of Planetary Research and Dr. Franz Schreier)

Abbreviations and Acronyms

ABM	Arithmetic Blockmean
ADF	Auxiliary Data File
ADM	Atmospheric Dynamics Mission
AIRS	Atmospheric Infrared Sounder
ALADIN	Atmospheric Laser Doppler Instrument
AMC-DOAS	Air Mass Corrected DOAS
AMF	Air Mass Factor
ANX	Ascending Node Crossing
AP	Atmospheric Processors
AR	Axis Ratio
ARE	Atmospheric Radiative Effect
ASI	Agenzia Spaziale Italiana
ASM	Azimuth Scan Mechanism
ATBD	Algorithm Technical Baseline Document
ATC	Active Thermal Control
BIRA	Belgisch Instituut voor Ruimte-Aëronomie
BIRRA	Better InfraRed Retrieval Algorithm
BMBF	Bundesministerium für Bildung und Forschung
BSC	Backscatter Coefficient
CIRA	COSPAR International Reference Atmosphere
CL0	Consolidated Level 0
CNRS	Centre National de la Recherche Scientifique
COSPAR	Committee on Space Research
CSA	Canadian Space Agency
DBPM	Dead and Bad Pixel Mask
DFD	Deutsches Fernerkundungsdatenzentrum
DIMS	Data & Information Management System
DISORT	Discrete Ordinate Radiative Transfer
DLR	Deutsches Zentrum für Luft- und Raumfahrt
DOAS	Differential Optical Absorption Spectroscopy
D-PAC	German Processing and Archiving Centre
DPQC	Data Processing and Quality Control
DRACULA	aDvanced Retrieval of the Atmosphere with Constrained and Unconstrained Least-Squares Algorithms
DWL	Doppler Wind Lidar
EAS	Earth-Atmosphere System
ECMWF	European Centre for Medium-Range Weather Forecasts
ENVISAT	Environmental Satellite
EOS	Earth Observing System
EOWEB	Earth Observation on the Web
EPS	EUMETSAT Polar System
EQUAL	ENVISAT Quality Assessment with Lidar
ESA	European Space Agency
ESM	Elevation Scan Mechanism
ESRIN	European Space Research Institute
EU	European Union
EUMETSAT	European Organisation for the Exploitation of Meteorological Satellites
EUMETCast	EUMETSAT broadcast system for environmental data
FTIR	Fourier Transform Infrared Spectrometer
GAME	Groupe d'étude de l'Atmosphère Météorologique
GARLIC	Generic Atmospheric Radiation Line-by-Line Infrared Code
GAW	Global Atmosphere Watch
GDP	GOME Data Processor

GEMS	Global and regional Earth-system (Atmosphere) Monitoring using Satellite and in-situ data
GIIPSY	International Polar Snapshot Year
GMES	Global Monitoring for Environment and Security
GODFIT	GOME Direct Fitting
GOME	Global Ozone Monitoring Experiment
GRACE	Gravity Recovery and Climate Experiment
HGF	Helmholtz-Gemeinschaft Deutscher Forschungszentren e.V.
HK	House Keeping
HLOS	Horizontal Line-of-Sight
IASI	Infrared Atmospheric Sounding Interferometer
ICSU	International Council for Science
IMF	Institut für Methodik der Fernerkundung
IMLM	Iterative Maximum Likelihood Method
InSAR	Interferometric SAR
IPSL	Institut Pierre-Simon Laplace
IGY	International Geophysical Year
IPY	International Polar Year
IUP/IFE	Institut für Umweltphysik / Institut für Fernerkundung
IR	Infrared
JAXA	Japan Aerospace Exploration Agency
KNMI	Koninklijk Nederlands Meteorologisch Instituut
LbL	Line-by-Line
LAEQV	Longest Axis Equivalence
LED	Light Emitting Diode
LIDAR	Light Detection and Ranging
LIDORT	Linearized Discrete Ordinate Radiative Transfer
LLI	Life Limited Item
LNDF	Leaf Normal Distribution Function
LoS	Line of Sight
LOWTRAN	Low Resolution Transmission
LVMR	Levenberg-Marquart Approach
MACC	Monitoring Atmospheric Composition and Climate
MDS	Measurement Datasets
MetOp	Meteorological Operational Polar Satellites of EUMETSAT
MIPAS	Michelson Interferometer for Passive Atmospheric Sounding
MIROR	Michelson Interferometer with Rotating Retroreflector
MODTRAN	Moderate Transmittance Code
MOPITT	Measurements of Pollution in the Troposphere
NCEP	National Centers for Environmental Prediction
NIVR	Nederlands Instituut voor Vliegtuigontwikkeling en Ruimtevaart
NRT	Near-Realtime
NTO	Near-Realtime Total Ozone
O3M	Ozone Monitoring
OBM	Optical Bench Module
OCM	Orbit Control Manoeuvre
OCR	Operation Change Request
OL	Offline
OTO	Offline Total Ozone
PDS	Payload Data Segment
PDU	Product Dissemination Unit
PMD	Polarization Measurement Device
PROMOTE	Protocol Monitoring for the GMES Service Element
PUM	Product User Manual
QA	Quality Assurance
RT	Radiative Transfer
SACS	Support to Aviation Control Service

SAEQV	Shortest Axis Equivalence
SAF	Satellite Application Facility
SAMUM	Sahara Mineral Dust Experiment
SAR	Synthetic Aperture Radar
SCIAMACHY	Scanning Imaging Absorption Spectrometer for Atmospheric Chartography
SCD	Slant Column Density
SEM	Scanning Electron Microscope
SEQV	Surface Equivalence
SEU	Single Event Upset
SOST	SCIAMACHY Operations Support Team
SQWG	SCIAMACHY Quality Working Group
SRON	Netherlands Institute for Space Research
STG	Space Task Group
SVD	Single Value Decomposition
SWIR	Short Wave Infrared
TC	Thermal Control
TEMIS	Tropospheric Emission Monitoring Internet Service
TES	Thermal Emission Spectrometer
TN	Technical Note
TOA	Top of Atmosphere
UMARF	Unified Meteorological Archive and Retrieval Facility
UV	Ultraviolet
VEQV	Volume Equivalence
VIS	Visual
VSEQV	Volume-to-Surface Axis Equivalence
WBM	Weighted Blockmean
WFM-DOAS	Weighting Function Modified DOAS
WDC-RSAT	World Data Center for Remote Sensing of the Atmosphere
WMO	World Meteorological Organization

DLR at a Glance

DLR is Germany's national research center for aeronautics and space. Its extensive research and development work is integrated into national and international cooperative ventures. As Germany's space agency, DLR has been given responsibility for the forward planning and the implementation of the German space program by the German federal government as well as for the international representation of German interests. Furthermore, Germany's largest project-management agency is also part of DLR.

Approximately 5,100 people are employed in DLR's 27 institutes and facilities at eight locations in Germany: Köln-Porz (headquarters), Berlin-Adlershof, Bonn-Oberkassel, Braunschweig, Göttingen, Lampoldshausen, Oberpfaffenhofen, and Stuttgart. DLR also operates offices in Brussels, Paris, and Washington, D.C.

Remote Sensing Technology Institute
Institut für Methodik der Fernerkundung

DLR's Remote Sensing Technology Institute (IMF) is located in Oberpfaffenhofen, Berlin-Adlershof, and Neustrelitz.

IMF carries out research and development for retrieving geo-information from remote sensing data. It conducts basic research on physical principles of remote sensing and develops algorithms, techniques, and operational processing systems for synthetic aperture radar, optical remote sensing, and spectrometric sounding of the atmosphere. The processing systems are in operational use for national, European, and international Earth observation missions.

For preparation and in support of spaceborne missions IMF operates a suite of multi- and hyperspectral optical airborne sensors. The institute contributes its expertise to novel sensor and mission concepts.

The German Remote Sensing Data Center (DFD) and IMF form DLR's Applied Remote Sensing Cluster (C-AF).

**Deutsches Zentrum
für Luft- und Raumfahrt** e.V.
in der Helmholtz-Gemeinschaft